UNIVERSITÀ
DEGLI STUDI
FIRENZE

Scuola di
Scienze Matematiche
Fisiche e Naturali

Corso di Laurea Magistrale in
Scienze Fisiche e Astrofisiche

Instability of persistent currents in fermionic superfluid rings

Instabilità di correnti persistenti in anelli fermionici superfluidi

Relatrice
Giulia Del Pace

Correlatore
Leonardo Fallani

Candidato
Nicola Grani

Anno Accademico 2020/2021

Contents

Introduction

The study of fermionic many-body systems is crucial in the understanding of many phenomena, as fermions are the fundamental component of matter. The behaviour of electrons in solid state system or nucleons in atomic nuclei are some examples. However, as the number of particle in the system increases, an exact mathematical description is too complicated. Also numerical simulations become not trivial. In order to understand the behaviour of these systems, Feynman proposed the use of controllable quantum systems as quantum simulators [1]. The high degree of control and manipulation obtained in the last decades on atomic samples makes ultracold quantum gases an ideal candidate for this realization. In particular strongly interacting gases of ultracold fermionic atoms are perfect platforms for the study the many-body phenomena like superfluidity. Moreover, interactions in this systems can be tuned by using Feshbach resonances allwing to explore the BEC-BCS crossover. In this way, it is possible to explore different regimes of superfluidity. Superfluids are described by an order parameter, $\psi(\mathbf{r},t) = |\psi(\mathbf{r},t)|e^{i\phi(\mathbf{r},t)}$, consisting in a macroscopic wave function of the system [2]. In particular $|\psi(\mathbf{r},t)|^2$ is associated with the density of superfluid fraction, while the phase $\phi(\mathbf{r},t)$ is directly connected to its velocity: $\mathbf{v}(\mathbf{r},t) = \frac{\hbar}{m}\nabla\phi(\mathbf{r},t)$. Superfluids are characterized by no dissipative flow up to a critical velocity v_c [3]. In the case of charged particles, this corresponds to the critical current in superconductivity in solid state physics. [4]. Superfluidity can also be observed in normal mesoscopic systems [5, 6]. The realization of these currents leads to application, like the SQUIDs which is able to measure magnetic field with a high degree of precision [7]. The existence of persistent currents is the hallmark of the superfluid state. For superconducting rings pierced by a magnetic field, persistent currents arise as the new ground state of the system and both the Aharonov-Bohm effect [8], and a quantization of the magnetic flux occur [9].

The high degree of control and manipulation available on ultracold quantum gases, allows for the realization of superfluid system with arbitrary geometry. In particular, it is possible to excite persistent currents in also a ring-shaped superfluid. In neutral atomic superfluids systems in a ring, the continuity of the order parameter around the loop makes possible only quantized circulation states. The stability and decay of supercurrents have been studied in superfluid Helium and in superfluid bosonic rings [11, 12]. Only, recently, persistent currents have been observedalso in atomic superfluids [48]. However the decay mechanism is not fully understood yet.

In our system, we create homogeneous fermionic superfluid in tunable rings, that allow to study superfluid system with periodically boundary conditions. We control the phase of the system exciting persistent currents via a phase imprinting method in all the BEC-BCS crossover. We detect the state of the system by interferometric measurements. In the contest of this thesis, I study the instabilities of persistent current in a ring superfluid in the presence of an obstacle, whose size is of the order of the correlation length. In particular, we are able to choose the number, the dimension and the intensity of the obstacles with a high degree of freedom, engineering defect in a controlled way in the system, in opposition to solid state systems, in which the presence of impurity is not controllable. Decay of persistent currents has been observed above a critical circulation. We observe the current to decay through emission of quantized vortices. Furthermore, we exploit the possibility of tuning the potential shape to study an even more exotic configuration, as the one of two counter propagating

persistent currents in superfluids obtained by tailoring two rings separated by a barrier on the atomic sample. Under some condition, a vortex crystal ring at the interference between the two superfluids arises from the merging of the two superfluids. This configuration evolves by a dynamical instability related to the Kelvin-Helmholtz instability in classical fluids.
My work thesis is organized as following:

- In Chapter 1, I present some theoretical background of strongly correleted fermi superfluids underling the study I performed during my thesis, with particular attention of the effects of interactions. I will show how it is possible to manipulate interactions in atomic gases via Feshbach resonances by changing the magnetic field and how this gives the possibility to explore the BEC-BCS crossover. Next, the main features of superfluidity are described. Then, I will show how the Landau criterion predicts that superfluidity can occurs only below a critical velocity and I will show how the macroscopic wave function description of the system gives rise to quantized vortices and to the quantization of persistent current in a ring-shaped superfluid. Finally I will present the basis of a dynamical instability that occurs in classical fluid: the Kelvin-Helmholtz instability.

- In Chapter 2, I provide a description of the experimental method used in our system to realize persistent current in a ring-shaped superfluid. In particular, in the first part I describe the techniques used to reach a condensed Fermi gas. Subsequently I describe the high resolution system used both for imaging the sample and for the creation of arbitrary optical potential with a Digital Micromirror Device, that allows for the creation of ring-shaped superfluid samples. Next I present the phase imprinting methods implemented for excite persistent currents states in the sample and the interferometer method used in order to detect the state of the system. I then present some analysis on the additional effects from the phase imprinting technique as the creation of quantized vortices. Finally, I will show the effects of the geometry of the system on the persistent currents in the sample.

- In Chapter 3, I present the results about the instability of persistent currents in a ring against the presence of an obstacle. In the first part I concentrate on the stability of persistent currents against the presence an obstacle acts on the sample. In the BEC and BCS regimes, a decay is observed only for high velocity states of the system, above a critical velocity. Moreover, differences between the regimes are highlighted. The UFG gas demonstrate to be the most stable one. Moreover, the decay observed in the BCS regime respect to the UFG one, can underline the presence of dissipative effects linked to the fermionic nature of the system, like pair breaking mechanism. Then, I give an explanation of the microscopic mechanism underling the dissipative process in term of quantized vortices nucleation.

- In Chapter 4, I present the realization of the double ring geometry, characterizing the potential used for this purpose. Next, I describe the techniques for the excitation of counter propagating persistent currents in this system. This will be useful in the understanding of the merging of two counter-flowing condensed system. Due to the phase coherence of the system, the merging can creates soliton structures or a regular array of quantized vortices that are unstable in time. Finally I will present some preliminary results of the an analogous of the Kelvin-Helmholtz instability.

Chapter 1

Basics on fermionic systems

In this chapter I present the theoretical frame necessary for understanding the experimental work showed in the next chapters. In the first section I resume the main properties of a non-interacting Fermi gas. In the second section I present the physics of interacting fermionic system, starting from the scattering theory and showing how is possible to manipulate interactions between atoms using Feshbach resonances, that allow us to realize the BEC-BCS Crossover. In the last section I present the theoretical description of the Kelvin-Helmholtz instability as it occurs in classical fluids.

1.1 The non-interacting Fermi gas

Particle with half integer spin are known as fermions. The request of the antisymmetrazation on the wave function for this particle prevents the occupation of the same quantum state by more than one particle. This is the Pauli exclusion principle.

For a fermionic system, in the Gran Canonical ensemble the average occupation number $\langle n_i \rangle$ of a single state i[1] with energy E_i is:

$$\langle n_i \rangle = \frac{1}{e^{\frac{E_i - \mu}{k_B T}} + 1}, \tag{1.1}$$

where μ is the chemical potential, k_B the Boltzamnn constant and T the temperature. At $T = 0K$ this distribution shows the typical step-like behaviour . In this case $\langle n_i \rangle = 1$ for each state with energy below the chemical potential and zero otherwise. The chemical potential at $T = 0$ defines the Fermi Energy $E_F = \mu(T = 0K)$. Distribution 1.1 can take a maximum value of $\langle n_i \rangle = 1$. This is consistent with the Pauli Exclusion principle, for which two fermions cannot occupy the same state.

1.1.1 Atomic Fermi Gases in harmonic traps

The effects of Fermionic nature of particles become important when to the average distance between particle $a \simeq 1/\sqrt[3]{n}$, where n is the density of the sample, is comparable to the typical spread of a wavefunctions describing single particles. For a temperature T this is given by the De Broglie wavelength

$$\lambda = \frac{h}{\sqrt{2\pi m k_B T}}, \tag{1.2}$$

[1]the states considered and their corresponding energy E_i are respectively eigenstates and eigenvalues of the one-particle Hamiltonian

where h and k_B are the Planck and the Boltzmann constants. As temperature is lowered, this quantity increase. In experiments on ultracold quantum gases low temperatures are achieved and therefore the effects of the quantum statistics of the atoms will be important.

In experiments, ultracold atoms are usually confined in a region of space using detuned lasers. These are used to create a trapping confinement, that is approximately described by an harmonic potential $V(x) = \frac{1}{2m}\omega^2 x^2$. w is the trap frequency and m the atomic mass. Using a semiclassical approach is possible to obtain the density distribution of a Fermi gas. From Eq. 1.1 we can write the expected occupation number of a cell of volume h^3 in the phase-space around the point $(\mathbf{r}, \mathbf{p})$ of position $\mathbf{r}$ and momentum $\mathbf{p}$ (Thomas-Fermi approximation) [13]:

$$f(\mathbf{r}, \mathbf{p}) = \frac{1}{e^{\frac{\frac{\mathbf{p}^2}{2m} + V(\mathbf{r}) - \mu}{k_B T}} + 1}. \tag{1.3}$$

Therefore, the density distribution is given by:

$$n(\mathbf{r}) = \int \frac{d^3\mathbf{p}}{(2\pi h)^3} f(\mathbf{r}, \mathbf{p}) \rightarrow_{T \to 0} \frac{1}{6\pi^2} \left(\frac{2m}{\hbar^2}\right)^{\frac{3}{2}} (\mu - V(\mathbf{r}))^{\frac{3}{2}}, \tag{1.4}$$

where we have considered the limit of zero temperature.

For harmonic traps, $V(\mathbf{r}) = \frac{1}{2m}\omega_x^2 x^2 + \frac{1}{2m}\omega_y^2 y^2 + \frac{1}{2m}\omega_z^2 z^2$. In this case, by integrating over the real space of Eq. 1.4 is possible to obtain the Fermi Energy

$$E_F = \hbar(\omega_x \omega_y \omega_z)^{\frac{1}{3}} (6N)^{\frac{1}{3}}, \tag{1.5}$$

where N is the atom number for each spin state, and the Thomas-Fermi radius in each direction is defined as:

$$R_{TF_{x,y,z}} = \sqrt{\frac{2E_F}{m\omega_{x,y,z}^2}}. \tag{1.6}$$

This quantity represent the typical dimension of the atomic sample.

Eq. 1.5 describes the Fermi energy of the system. However it is possible to define a local Fermi Energy $\epsilon(\mathbf{r}) = E_F - V(\mathbf{r}) = \frac{\hbar}{2m}(6\pi^2 n^{\frac{1}{3}}(\mathbf{r}))$, that reduces to E_F at $\mathbf{r} = 0$, where the harmonic potential vanishes. Moreover, combination of Eq. 1.5 and Eq. 1.6 shows that the dimension of the sample depend on the atom numbers $R_{TF} \sim \sqrt[6]{N}$. This is an effect of the Pauli principle, that makes atoms occupy all the states up to the Fermi Energy and therefore make the sample increase his dimensions for incraesing N.

1.2 Interactions in atomic Fermi Gas

Interactions play a fundamental role in the emergence of superfluidity. In the non interacting case the ground state of the system is the Fermi Sea, in which atoms occupy all the state with energy below E_F; in this case no superfluidity appears. In attractive fermionic system the formation of cooper pairs allows the creation of a superfluid. On the other hand, pairs of fermionic particles can bound together to form a molecula, in this case the pairs are bosons and the system can form a Bose Einstein condensate (BEC). In ^{6}Li the intensity and the sign of the interaction can be controlled by tuning an external magnetic field via a Feshbach resonance, allowing thus to study strongly interacting system. However is important to notice that collisions between indistinguishable fermions are suppressed by the request of antisymmetrization of the wave function: collisions are allowed only in mixture of two different species of fermions.

In the study of Feshbach resonances in bosonic systems, strongly interacting regimes was always observed through strong losses in the atoms number [14]. The cause of this behaviour is the increase of the losses in the sample due to the 3-body collision. In Fermionic gases with two difference species, three-body interactions are suppressed by the Pauli principle, allowing to study strongly interacting condensate.

1.2.1 Scattering theory

At the low temperatures achieved in experiments on ultracold quantum gases, the equilibrium state of the system is a crystal. The gas condition is only a metastable state and during collisions atoms can recombine and create a solid. The dominant channel for this process is the three-body recombination, that can be suppressed by lowering the density of the system. In this case interactions are dominated by two-body collisions so that, although in a metastable configuration, the gas will reach kinetic equilibrium long before a solid is created. Therefore experiment on ultracold quantum gas usually satisfy the diluteness condition $n|a_s|^3 \ll 1$, where a_s is a parameter I will define in this section representing the intensity of the interactions.

In the center-of-mass frame, it is possible to reduce the two-body collision to a one-particle problem. The corresponding Schrodinger equation is: [15]

$$-\frac{\hbar^2}{m}\nabla^2\psi(r) + V(r)\psi(r) = E\psi(r), \tag{1.7}$$

where $M = m/2$ is the reduced mass and $V(r)$ is the interaction potential. In the case of vanishing interactions, the solutions of Eq. 1.7 are plane waves $\sim e^{ikr}$ with $k = \sqrt{\frac{Em}{\hbar^2}}$. The presence of an interaction potential with finite range and no bound states modifies the solution. Far away from the scattering potential the wave function $\psi(r)$ can be expressed by the sum of the incident plane wave and a scattered wave consisting in the atom exiting the collision that is described by a spherical wave:

$$\psi(r) \sim e^{i\mathbf{kr}} + f(\mathbf{k}', \mathbf{k})\frac{e^{ikr}}{r}. \tag{1.8}$$

Here $f(\mathbf{k}', \mathbf{k})$ indicate the scattering amplitude. We will consider only the case of elastic collision, for which the incident and the outgoing wave numbers, respectively $\mathbf{k}$ and $\mathbf{k}'$ have the same modulus $|\mathbf{k}| = |\mathbf{k}'| = k$

Starting from this wave function, it is possible to write the differential cross-section in term of the scattering amplitude by the relation:

$$\frac{d\sigma}{d\Omega} = |f(\mathbf{k}, \mathbf{k}')|^2. \tag{1.9}$$

In the case of low energy scattering it is convenient to write the wave function in spherical armonic: the expression in Eq.1.8 gets [16]:

$$\psi(\mathbf{r}) = \frac{1}{2ikr}\sum_{l=0}^{+\infty}\sum_{m=-l}^{+l}\frac{U_{l,m}(r)}{r}Y_{l,m}(\theta, \phi). \tag{1.10}$$

The scattering potential between two ^{6}Li atoms is mostly given by the Van der Walls interaction, scaling like $\sim \frac{C_6}{r^6}$, at long distances, while atoms feel a strong repulsion when the distance between them becomes very short. The interactions between the low magnetic moments arising from the spin in negligible. Therefore collisions are described by an isotropic potential. In this case only the terms with $m = 0$ in the sum of Eq. 1.10 will be different form 0 and is possible to write Eq. 1.8 as:

$$\psi(\mathbf{r}) \sim \frac{1}{2ikr}\sum_{l=0}^{\infty}(2l+1)P_l(\cos(\theta))[(-1)^{l+1}e^{-ikr} + e^{2i\delta_l(k)}e^{ikr}]. \tag{1.11}$$

It's important to notice that a similar expression can be written for plane wave $e^{i\mathbf{kr}}$ that we have in the vanish potential case. This expression differs from the Eq. 1.11 only for the absence of the factors $e^{2i\delta_l(k)}$. Therefore the scattering phenomena is completely described by the phase shifts $\delta(l)$. The total scattering section can be written as:

$$\sigma(k) = \sum_{l=0}^{\infty} \frac{4\pi}{k^2}(2l+1)\sin^2(\delta_l(k)). \tag{1.12}$$

The way we deal with the interaction problem is very useful for the low energy scattering. A physical way to see this is the following: starting from the Schrodinger Equation 1.7 and using the wave function as is written in 1.10 neglecting the $m \neq 0$ terms, we can arrive to the expression:

$$\left(-\frac{\hbar^2}{m}\partial_r^2 + \hbar^2\frac{l(l+1)}{mr^2} + V(r). - E\right)\frac{U_{l,0}(\mathbf{r})}{r} = 0 \tag{1.13}$$

Solving this equation is possible to obtain $U_{l,0}(\mathbf{r})$ and therefore the phase factors from their asimptotyc limit. We can see this expression like a Schodinger equation with a effective potential $V_{eff} = \hbar^2\frac{l(l+1)}{mr^2} + V(r)$, that depend on l. For $l \neq 0$, V_{eff} is characterized by a centrifugal barrier. This term repress the $l \neq 0$ scattering in the low energy case.
Is possible to show that in the case of Van der Walls interaction the scaling law for low k of the phase shifts is given by:

$$\delta_l(k) \sim k^{2l+1} \tag{1.14}$$

The low temperatures reached by ultracold experiment allow to take into account the low momenta limit $k \sim 0$. In this case the *s-wave scattering* (corresponding to the $l = 0$ case) becomes predominant respect to all the other partial waves. In this limit, it is possible to define the *scattering length*

$$a_s = -\lim_{k\to 0}\frac{\tan(\delta_s)}{k}. \tag{1.15}$$

This factor completely describe the interactions. The sign identify the type of interaction (a_s is positive in the repulsive case, negative for the attractive one), while the modulus indicates the strength of the interactions. Finally, the total cross section can be express in term of a_s, in the low k case we can write:

$$\sigma = \frac{4\pi}{k^2}\sin^2(a_s^2k^2) \tag{1.16}$$

In the case of indistinguishable fermions the Eq. 1.8 must be correct for the antisymmetrization requirement. Following the same calculation, it is possible to obtain an equation similar to Eq. 1.12, in which only the term with odd l survives. As a result, the s-wave scattering is repress. On the other hand,as just seen, a low temperature $l \neq 0$ scattering are negligible due to the presence of the centrifugal term in Eq. 1.13. The result is that in ultracold fermionic gases indistinguishable particles do not interact between each other. Collisions in ultracold fermionic systems are allowed in mixture of different atomic species or between two difference magnetic states of the same specie. It is important to notice that in case of indistinguishable bosons we need to keep only the even terms in Eq. 1.12. In this case atoms can collide even at low temperature.

1.2.2 Feshbach resonances

The scattering length defined in Eq. 1.15 depends on the shape and on the depth of the interaction potential. Let's Imagine to increase the depth of the potential. For the low energy scattering, a_s

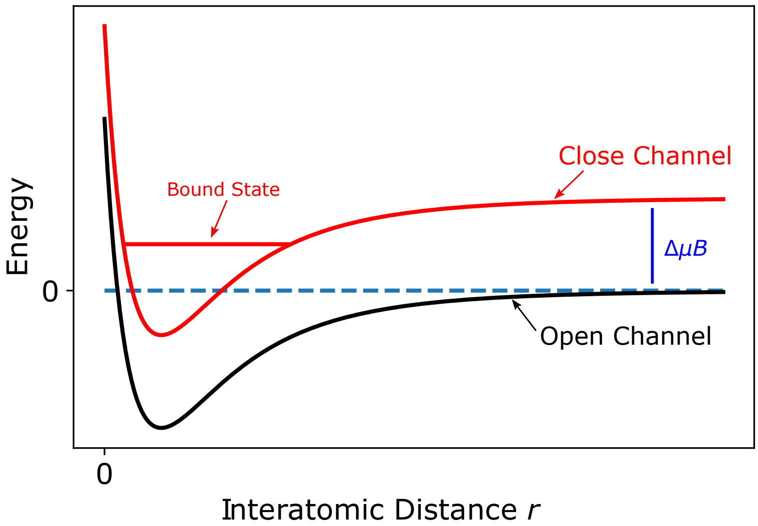

Figure 1.1: Underling mechanism of a Feshbach Resonance. Cause that Hamiltonian present non diagonal terms in the total magnetic moment, atoms colliding in a magnetic configuration, called open channel, are coupled to a different state (the close channel). Due to the different magnetic moment of the two state is possible to tune the relative energy using a magnetic field B. When a bound state of the close channel equal the energy of the free particle in the open channel the scattering length diverges, even if the coupling is weak.

diverges when a new bound state enters in the potential, namely when the interacting potential has a bound state with energy near 0 [17]. Before the formation of this bound state, a_s is negative, while become positive when the new bound state is created. This feature play a crucial role in the manipulation of atom interactions, in the Feshbach resonances and in the realization of the BEC-BCS crossover.

In the previous section we analyzed the scattering problem by a general point of view. In the case of atom-atom interaction, the scattering potential depends on the internal states of the atoms. If the magnetic configuration of the colliding atoms is well defined, what we have see in the previous section fully describe the interactions. However, in the alkali atoms the Hamiltonian presents non diagonal term in the total magnetic moment. This provides a coupling between two-particle state with different magnetic configurations. In relation to Fig 1.1, let's consider two atoms colliding in a magnetic configuration, that is called *open channel*, with an interaction potential represented by the black curve. If this state is coupled with an other one with a different magnetic configuration that support the presence of a bound state, a powerful physics arises. Due to the different magnetic moment $\Delta\mu$ in the two configurations, it is possible to tune the relative energy using a magnetic field B as show in Fig. 1.1. When a bound state for the closed channel reach the energy of the free particle in the open channel, the scattering length diverges, even if the coupling is weak. This is the mechanism underling the *Feshbach resonances*. Around a Feshbach resonance, the relation between a_s and B is given by [17]:

$$a_s = a_{bg}\left(1 - \frac{\Delta}{B - B_0}\right), \tag{1.17}$$

where B_0 is the centre of the resonance, namely the magnetic field at which the scattering length diverges, Δ represents the width of the resonance and a_{bg} is the background scattering length, namely

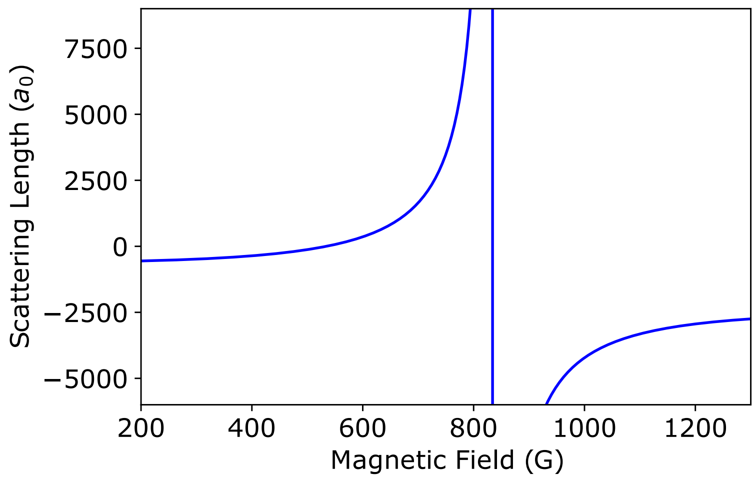

Figure 1.2: Scattering length between the two lower hyperfine states $|F, m_f\rangle = \left|\frac{1}{2}, -\frac{1}{2}\right\rangle$ and $|F, m_f\rangle = \left|\frac{1}{2}, \frac{1}{2}\right\rangle$ of ^{6}Li atoms. The scattering length diverges for $B = 834\,15G$. In the region just below this magnetic field, the scattering length is positive and therefore we have a repulsive system. for B above the resonance value, the scattering length is negative and we have an attractive fermionic system. The big width of this particular Feshbach resonance allow a fine tuning of the scattering length. The curve is obtain with the values from [18].

the value assumed by a_s far apart from the resonance. The importance of the Feshbach resonances lies on the possibility to manipulate the intensity of the interactions as well the sign of a_s, allowing the study of systems with on-demand interactions.

Is important to notice that a divergence of the scattering length a_s doesn't implies a infinity cross section, but rather a maximization of this quantity to $\sigma = \frac{4\pi}{k^2}$

The lithium case

The blue curve in Fig. 1.2 shows the values of a_s as a function of the magnetic field B across the Feshbach resonance between the two lower hyperfine states $|F, m_f\rangle = \left|\frac{1}{2}, -\frac{1}{2}\right\rangle$ and $|F, m_f\rangle = \left|\frac{1}{2}, \frac{1}{2}\right\rangle$ of ^{6}Li atoms. The scattering length is approximatly descibed by Eq. 1.17 with the values present in Table 1.1.

B_0	Δ	a_{bg}
$834.15G$	$300G$	$-1405a_0$

Table 1.1: Values of Eq.1.17 for the two lower hyperfine states $|F, m_f\rangle = \left|\frac{1}{2}, -\frac{1}{2}\right\rangle$ and $|F, m_f\rangle = \left|\frac{1}{2}, \frac{1}{2}\right\rangle$ of ^{6}Li atoms.

This number are unusual respect to the Feshbach resonances of other alkali atoms. In particular typical Δ are one or two order of magnitude lower [19]. The result is the possibility of tune the scattering length in a finer way and a more stable value of a_s against magnetic field fluctuations, making ^{6}Li a species with unique features for the study of strongly interacting Fermi gases in the BEC-BCS crossover.

1.2.3 The BEC-BCS crossover

The Feshbach resonance of Fig. 1.2 allows for the study of fermionic superfluidity in different interaction regimes. Superfluidity consists in the possibility of some fluids to flow without loss of kinetic energy. In fermionic systems, superfluidity arise from the condensation of couple of fermions with opposite spin. For negative interaction, fermions with opposite momentum can form Cooper pairs and the system is described by the Bardeen-Cooper-Schrieffer (BCS) theory [20]. For magnetic field B below the resonant value B_0, atoms bounds together in weakly bound bosonic molecules; in this case the superfluidity of the system can by understood within Bose-Einstein condensation theory. In the intermediate region where the scattering length diverges, the system is in the so called *'unitary regime'*. Although different regimes show different properties, the passage from the BCS regime to the BEC regime is not abrupt, but it is rather a smooth crossover that can be describe with the same many-body wave function [21, 13]. Considering the characteristic energy in a Fermi system E_F, the BEC-BCS Crossover is parameterized by the factor $k_F a_s$, where $k_F = \sqrt{\frac{2mE_F}{\hbar^2}}$ is the Fermi wave-vector.

BEC regime

In the BEC regime, the superfluidity is given by the condensation of fermions in a molecular state. In the vicinity of the Feshbach resonance, the binding energy is given by [17]

$$E_b = -\frac{\hbar^2}{ma_s^2}. \tag{1.18}$$

In the $k_F a_s \to 0$ limit the chemical potential in a mean field approach is given by [19]:

$$\mu = -\frac{\hbar^2}{2ma_s^2} + \frac{\pi\hbar^2 a_s n}{m}. \tag{1.19}$$

The first contribution to the chemical potential is given by the binding energy per particle. The second term arise from the energy contribution of the collision. This last term has the typical form of the chemical potential for attractive BEC $\mu_{BEC} = \frac{4\pi\hbar^2 a_s n}{m}$ [2]. This confirms the idea the in this case the system in described like a Bose-Einstein condensate. Is possible to argue that n this case diatomic molecules interactions are given by the collision of atoms forming them. The result is a repulsive interaction between molecules. By the comparison between the expression[2] $\mu_M = \frac{4\pi\hbar^2 a_{s_M} n_M}{m}$ and Eq. 1.19 one obtain $a_{s_M} = 2a_s$. Experimental results on Ref. [22] show that a more correct value should be $a_{s_M} \simeq 0.6a_s$, consistently with a beyond mean-field calculation.

BCS regime

Condensation in bosonic systems arises from a macroscopic occupation of one energy state. Because of the different statistic, in non-interacting fermionic system this is forbidden. However in case of attractive interaction, two fermionic particle moving in a background of a filled Fermi sea can form a bound state [23]; this is called *Cooper pair*. This bound states have a many-body origin, because the presence of a filled Fermi sea is essential for its formation [24].

For atomic gases, in the $k_F a_s \to 0$ limit, the mean field calculation obtain:

$$\mu = E_F, \tag{1.20}$$

$$\Delta = \frac{8}{e^2} e^{-\pi/2k_F|a_s|}, \tag{1.21}$$

[2]The M subscript indicates the molecular properties

where Δ is the, gap, namely the bound energy of the pairs. The chemical potential equals the Fermi energy, while Eq. 1.21 can be rewritten in the classical BCS theory result. Because of the exponential decay with $-1/k_F|a_s|$, Cooper pairs are very fragile in this limit. For this reason, the critical temperature is lowered moving toward the BCS regimes. In the experimental realization, condensation of attractive ^{6}Li pairs are therefore obtain for $1/k_F|a_s| < 1$

1.3 Superfluidity in fermionic systems

Superfluidity is mostly associated to condensed systems. By definition superfluids can carry current without dissipations. This is a common feature showed by different system, like Bose-Einstein Condensates and superconductive systems, with the only difference that we have a flow of charges in the second case. The underling theories describing the two systems are different. However this universal behaviour, despite the different physical description, is understandable by the Landau criterion, which reveals a strong connection between the superfluidity of a system and the properties of its excitation spectrum, and is well highlighted by the study of superfluidity in the BEC-BCS crossover.

1.3.1 Landau's Criterion for Superfluidity

In superfluids, flow without dissipation can occur up to a critical velocity v_c [3]. Above v_c the system can decrease the kinetic energy in favour of the formation of excitations in the sample. Let's consider a fluid of mass m moving with an initial velocity $\mathbf{v}_i$ and assume that an excitation with momentum $\hbar\mathbf{k}$ is created. Momentum conservation law requires that

$$m\mathbf{v}_i = m\mathbf{v}_f + \hbar\mathbf{k}, \tag{1.22}$$

where v_f is the fluid velocity after the creation of the excitation. Furthermore, the energy conservation principle requires that

$$\frac{m\mathbf{v}_i^2}{2} = \frac{m\mathbf{v}_f^2}{2} + \epsilon(\mathbf{k}), \tag{1.23}$$

where $\epsilon(\mathbf{k})$ is the energy of the excitation. Combining this two equation we obtain

$$\hbar\mathbf{k} \cdot \mathbf{v}_i = \epsilon(\mathbf{k}). \tag{1.24}$$

This equation can be solve for each value of $\mathbf{v}_i$ for which $v_i \geq \epsilon(\mathbf{k})/\hbar k$. The equal is valid in the case of $\mathbf{v}_i$ parallel to $\mathbf{k}$. For different orientation v_i must be bigger. Therefore the minimum velocity at which is possible to create excitations is given by

$$v_c = \min\left(\frac{\epsilon(\mathbf{k})}{\hbar k}\right) \tag{1.25}$$

For velocities below this critical value it's impossible to create excitation by degrading the velocity of the fluid and the system will exhibit a superfluid behaviour. In ultracold quantum gases, the superfluidity of a Bose-Einstein Condensate was tested by the evidence of a critical velocity in the early years after the discovery [25].

Critical Velocity in the BEC-BCS crossover

Eq. 1.25 show that the critical velocity strongly depends on the energy spectrum of the system, that changes moving across the BEC-BCS crossover . In the BEC limit, excitations are describe by the Bogoliubov theory of interacting bosonic gases [26]. In this regime the critical velocity correspond to the speed of sound $c_s = \sqrt{\mu_M/m_M} = \sqrt{\frac{4\pi\hbar^2 a_M n_m}{m_M}}$. In term of the single fermionic atom's properties

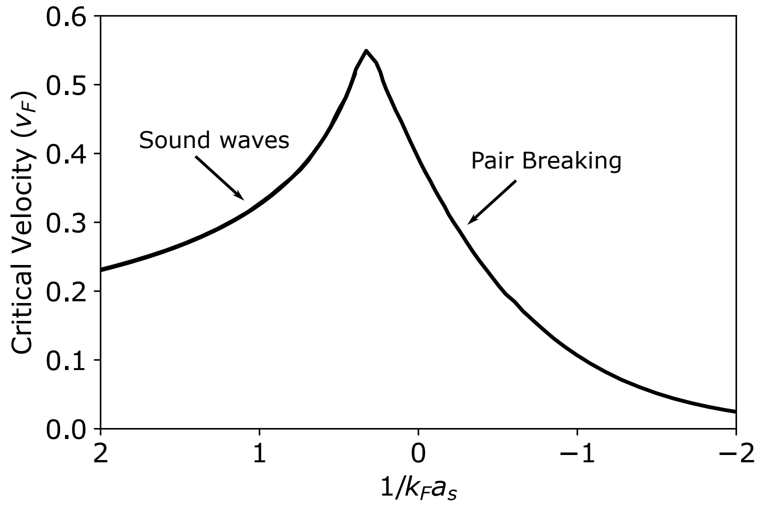

Figure 1.3: Critical Velocity across the BEC-BCS crossover. In the BEC side the critical velocity is given by the speed of sound, while in the BCS limit destruction of cooper pairs limit the maximum velocity for the superflow. In both the regimes, critical velocity increase for stronger interactions, so we have a maximum value around the resonance. Figure adapted from [19]

this takes the form $c_s = \frac{v_f}{\sqrt{3\pi}}\sqrt{k_F a_s}$. [13] In the BCS limit the excitations related to the critical velocity correspond to the breaking of Cooper pairs. In this case the critical velocity is approximately given by $v_c \simeq \frac{\Delta}{\hbar k_F}$. A fluid velocity above this v_c will break fermionic pairs.

In both the BEC and BCS regimes, the critical velocity increases as the interactions become stronger. Therefore a maximum value around the resonance is expected, as shown in Fig. 1.3 Measurements of the critical velocity across the BEC-BCS crossover show this expected behaviour [27] [28]. However, the measured critical velocity was always less than the expected value. The reason for this is mostly given by experimental deviation from the ideal case [27], like the inhomogeneity of a system in harmonic traps or the experimental procedures.

1.3.2 Vortices

The critical velocity plotted in Fig. 1.3, identifies sound waves and pair braking as the excitations limiting the superfluid flow. However some excitations are not considered in this calculation. One of this are quantized vortices. In many case formation of quantized vortices are the excitations limiting maximum velocity of the superfluid flow. Superfluid systems like Bose-Einstein condensates are described by an order parameter

$$\psi(\mathbf{r},t) = |\psi(\mathbf{r},t)|e^{i\phi(\mathbf{r},t)} \tag{1.26}$$

that is the macroscopic wave function of the condensate. $|\psi(\mathbf{r},t)|^2$ gives the density profile of the condensed part of the system, while $\phi(\mathbf{r},t)$ represent its phase. This quantity play is connected to the velocity field of the superfluid, that is:

$$\mathbf{v}(\mathbf{r},t) = \frac{\hbar}{m}\nabla\phi(\mathbf{r},t) \tag{1.27}$$

where m is the mass of one atoms. For fermionic superfluids $m \to 2m$ because in this case superfluidity arise from condensation of pair of particle.

Eq. 1.27 shows that the velocity field for a superfluid is irrotational $\nabla \wedge \mathbf{v}(\mathbf{r},t) = 0$. Therefore for simply connected region of space where $|\psi(\mathbf{r},t)| \neq 0$, using Stokes' theorem is possible to show that the circulation of $\mathbf{v}(\mathbf{r},t) = 0$ around a close path is always zero. More interesting physics appears when there exists a line of the sample where $|\psi(\mathbf{r},t)| = 0$. In this case we cannot use the Stokes' theorem. From Eq. 1.27 is easy to understand that a line integral of the velocity field between to points is related to the difference of the phase of the two points. When a closed line is considered the change in phase of the wave function $\Delta\phi$ must be a multiple of 2π, so that the circulation Γ can have only the values [29]

$$\Gamma = \oint \mathbf{v}(\mathbf{r},t) \cdot d\mathbf{s} = 2\pi n \frac{\hbar}{2m} = l \frac{h}{2m} \tag{1.28}$$

where l is a integer. This formula shows that Γ is quantized in units of $\frac{h}{2m}$. This condition of the system is a *quantum vortex* and l is its charge.

In the simplest case in which the phase increases linearly around the vortex core, namely $\phi = l\theta$ where θ is the azimuthal angle, the velocity field takes the form:

$$\mathbf{v}(\mathbf{r},t) = l \frac{\hbar}{2m} \frac{1}{r} \hat{\theta} \tag{1.29}$$

that shows a decrease of the velocity as the distance from the core of the vortex r increases. On the other hand, the velocity diverges in the limit of $r \to 0$. This non physical condition is resolved by a corresponding decrease of the density for lower values of r. In particular the density is zero in the core[3]. Therefore the presence of a vortex in marked as density depletion in the condensed density.

Feynman approach to the Critical Velocity

The critical velocities considered in Fig. 1.3 doesn't take in account the possibility of vortices excitation limiting the superflow maximum velocity. In 1955 Richard Feynman [30] obtained the corrisponding critical velocity for a superfluid flowing through a channel into an infinite reservoir. For velocity sufficiently high, the flow produces a series of vortex pairs from the corners at the end of the channel. The critical velocity above which vortex pairs are created is given by:

$$v_c = \frac{\hbar}{md} \ln\left(\frac{d}{\xi}\right) \tag{1.30}$$

where d is the width of the channel and ξ is the healing length.

1.3.3 Superfluidity and vortices: the ring geometry

A link between vortices and flow without dissipation is showed in the case of a superfluid trapped in a ring-shaped trap like the one showed in Fig. 1.4. In this case the system can flow in a perpetual motion in a toroidal trajectory. However the velocity $v(\mathbf{r},t)$ of the system is limited to discrete values. For the circulation Γ calculated integrating the velocity field along the orange dotted line in the figure, one obtain the same result of Eq. 1.28. Considering the case of cylindrical symmetry, in analogy to Eq. 1.29, the velocity field will be given by:

$$\mathbf{v}(\mathbf{r},t) = w \frac{\hbar}{2m} \frac{1}{r} \hat{\theta} \tag{1.31}$$

where the charge of the vortex indicated by l in Eq. 1.29 is replace by $w <$, which I will refer to as the *circulation* of the system. Therefore the velocity of a persisten current in a ring superfluid cannot take

[3] Note that this is consistent with the initial request of a line in which the density vanishes. In general cases, the vanish density at the core of the vortex avoid the problem of th

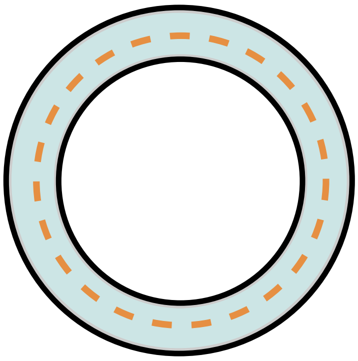

Figure 1.4: Superfluid flow in a ring. For superfluids confined in a ring-shaped potential the persistent flow is limited not only by the critical velocity. In fact, in analogy with the vortex case, the velocity must be quantized.

every values, but is quantized. Moreover, as in the vortex case, the velocity decrease as the distance from the centre of the ring increase.

By this point of view, a persistent flow of a superfluid through a ring with winding number ω can be seen as vortex of charge l in the centre of the ring.

1.4 Kelvin-Helmholtz Instability

The Kelvin-Helmholtz instability is an instability that occurs in the surface between two fluids flowing with different parallel velocities. It was initially introduced to explain the generation of waves in the sea by wind by H. v. Helmholtz [31] and Lord Kelvin [32]. However Kelvin-Helmholtz instabilities are also observed in other context, like the Red Spot on Jupiter or, in same case, in the clouds in our atmospheres.

Let's consider the 2D case shown in Fig. 1.5, where two fluids with density ρ_1 and ρ_2 flow with parallel velocity $\mathbf{v_1}$ and $\mathbf{v_2}$ along the x direction. This state in a stationary condition. However, if a small perturbation of the system occurs,is possible to show that this tend to increase in time. Cause small perturbations inevitably appear in real fluids, the configuration in Fig. 1.5 is not stable. For the following consideration, we will consider incompressible fluids with zero viscosity. In this cases, the dynamics of fluids is described by:

$$\frac{\partial \mathbf{v}}{\partial t} + (\mathbf{v} \cdot \nabla)\mathbf{v} = -\frac{\nabla p}{\rho}, \tag{1.32}$$

and

$$\nabla \cdot \mathbf{v} = 0, \tag{1.33}$$

where $\mathbf{v}$ is the Eulerian velocity field, ρ is the density of the fluid and p the pressure. Eq. 1.32 is known as Euler equation, while Eq. 1.33 is the continuity equation for incompressible fluids. The study of instabilities from a small perturbation of a stationary flow are usually performed in the following way: considering a stationary solution for the equation describing the fluid, with velocity $\mathbf{v_0}$ and pressure p_0, we look at the time evolution of a system with velocity field and pressure given by

$$\mathbf{v} = \mathbf{v_0} + \mathbf{v}' \tag{1.34}$$

and

$$p = p_0 + p', \tag{1.35}$$

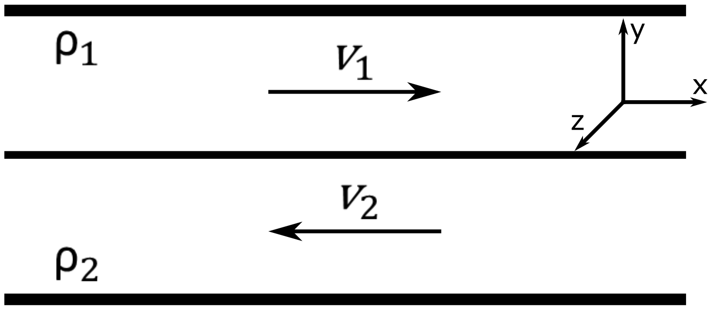

Figure 1.5: Parallel flow of two immiscible fluids with density ρ_1 and ρ_2 and velocity $\mathbf{v_1}$ and $\mathbf{v_2}$.

where $\mathbf{v_0}$ and p_0 describe the small perturbation of the system.

Substituting this in Eqs. 1.32 and 1.33, considering that $\mathbf{v_0}$ and p_0 are solutions of these equations, and neglecting terms over the first order we obtain for the perturbation $\mathbf{v}'$ and p' [33]:

$$\frac{\partial \mathbf{v}'}{\partial t} + (\mathbf{v_0} \cdot \nabla)\mathbf{v}' + (\mathbf{v}' \cdot \nabla)\mathbf{v} = = -\frac{\nabla p}{\rho}, \tag{1.36}$$

and

$$\nabla \cdot \mathbf{v}' = 0, \tag{1.37}$$

We consider now the the system in Fig. 1.5 presents a perturbation like in Fig. 1.6. In the case of non viscous fluids, the velocity field is constant both in the upper and the lower parts and a jump discontinuity in the velocity in present in the separation surface. We describe this perturbation with the displacement of the separation surface along the y axes $\zeta(x,t)$ depending on the x coordinate and on time. We can consider a perturbation for which all the quantity ζ, $p'_{1,2}$ $\mathbf{v'_{1,2}}$ are periodical function proportional to $e^{i(kx-\omega t)}$. From Eqs. 1.36 and 1.37, considering that the velocities $\mathbf{0}$ $\mathbf{v'_{1,2}}$ are along the x axes, using the relation

$$\frac{\partial \zeta}{\partial t} = v'_y - v_0 \frac{\partial \zeta}{\partial x}, \tag{1.38}$$

it is possible to obtain a relation between the perturbed part of the pressure p' and the displacement ζ [33]:

$$p'_1 = -\zeta \frac{\rho_1 (kv_1 - \omega)^2}{k} \tag{1.39}$$

$$p'_2 = \zeta \frac{\rho_2 (kv_2 - \omega)^2}{k} \tag{1.40}$$

Finally, considering that the pressure must be the same at the separation surface, from these last two equation we obtain the dispersion relation between ω and k:

$$\omega(k) = k\frac{\rho_1 v_1 + \rho_2 v_2}{\rho_1 + \rho_2} \pm ik \frac{\sqrt{\rho_1 \rho_2 (v_1 - v_2)^2}}{\rho_1 + \rho_2}, \tag{1.41}$$

that is formed by a real and a imaginary part. This equation is important for understanding the evolution of the perturbation. For simplify the calculation, we consider the case for which $\rho_1 = \rho_2$. In this case the ratio c between ω and k is:

$$c = \frac{\omega(k)}{k} = c_r \pm ic_i, \tag{1.42}$$

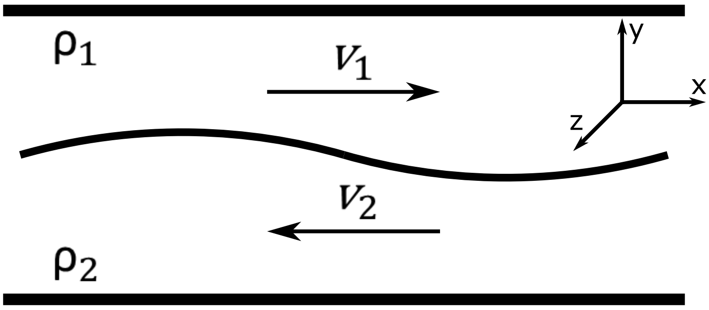

Figure 1.6: Sinusoidal perturbation of the separation surface between the two fluids.

with

$$c_r = \frac{v_1 + v_2}{2}, \qquad c_i = \frac{v_1 - v_2}{2}. \tag{1.43}$$

Therefore c is a complex quantity, with a realc_r and an imaginaryc_i part We consider now that the perturbation of the separation surface is described by

$$\zeta(x,t) = \zeta_0 e^{i(kx-\omega t)} = e^{ik(x-ct)}. \tag{1.44}$$

From this equation we understand that c_r is the velocity of the perturbation along the x axes and it depends on the sum of the velocity v_1 and v_2. On the other hand, the imaginary part generates an exponential increase (or decrease, depending on the sing in Eq. 1.42) of the intensity of the perturbation, depending on the velocity difference between the two fluids. Therefore, the displacement of the separation surface increase exponential for each initial perturbation of the system; in particular, for each value of k. In particular, the instability increase exponentially $\sim e^{\sigma t}$, with a rate

$$\sigma = kc_i = k\frac{\Delta v}{2}, \tag{1.45}$$

where $\Delta v = v_1 - v_2$. A linear increase of the exponential rate respect to k is obtained.

The result in Eq. 1.42, is obtained by considering a jump discontinuity in the velocity in the presence of the separation surface. However, when the component of the system are viscous fluids, this is not possible to occurs. A more realistic model can be studied taking into account the presence of a shear layer between the two region with uniform velocity $\mathbf{v_1}$ and $\mathbf{v_2}$, in which the velocity changes linearly. In particular, the velocity is this case is described by:

$$\mathbf{v} = \begin{cases} \mathbf{v1} & \text{for } y > \delta \\ \frac{\mathbf{v1+v2}}{2} + \frac{\mathbf{v1-v2}}{2}\frac{y}{\delta} & \text{for } |y| \le \delta \\ \mathbf{v2} & \text{for } y < -\delta \end{cases}$$

where δ is the dimension of the shear layer

In this case the dispersion relation takes the form [34]:

$$\omega(k) = k\frac{\rho_1 v_1 + \rho_2 v_2}{\rho_1 + \rho_2} \pm i\frac{v_1 - v_2}{4\delta}\sqrt{e^{-4k\delta} - (2k\delta - 1)^2}, \tag{1.46}$$

The rate of the instability increase linearly for low value of k, as in the case of the discontinuity jump in the velocity field. However for higher mode, σ tends to decrease, and the instability disappears for k such that $e^{-4k\delta} - (2k\delta - 1)^2 \ge 0$. This correspond to value of $k\delta \sim 0.6$. The suppresion happens to a similar value when we consider a shear layer in which the velocity changes in a hyperbolic tangent way.

The exponential increase of the perturbation gives rise to a self-similar swirling structure. The Kelvin-Helmholtz instability underlies the formation of structures like the one showed in Fig. 1.7

Figure 1.7: Sinusoidal perturbation of the separation surface between the two fluids.

Chapter 2

Excitation of persistent currents in fermionic superfluids

In this chapter I describe how it is possible to excite finite circulation states in a ring-shaped fermionic superfluid as the one shown in Fig. 1.4. In the first section I describe the protocol used for cooling down the atoms and create a fermionic superfluid. Next I present how is possible, using a Digital Micromirror Device (DMD), to create on demand optical potential, allowing for the realization of a ring trap. Finally I describe the procedure used to excite persistent currents in this geometry, that underlies the study of their instabilities presented in the following chapters. In particular, I will present general results about this. More details about the study of persistent currents are present in [35].

2.1 Create a degenerate ^{6}Li gas

From their first implementations in cooling ions and atoms in the late $'70$ of the last century, the techniques based on use of lasers and magnetic field for atom cooling and trapping had a great improvement. In this section I present how is possible to cool down to degeneracy a fermionic sample of ^{6}Li atoms. A detailed description of the apparatus used for this purpose is presented in [36].

At room temperature, lithium is at the solid state. Therefore, to obtain a sufficient high flux of atom in a gaseous state, the starting point consists in a oven, where a lithium sample is heated at the temperature of 420°C. The produced vapour reaches the rest of the experimental apparatus through a nozzle, creating an high-velocity collimated atomic beam.

2.1.1 Laser Cooling

The effect of a electromagnetic field acting of an atom is described, in a semiclassical approach, by a force [37]:

$$\mathbf{F} = \mathbf{F_s} + \mathbf{F_d}, \tag{2.1}$$

where the first term, $\mathbf{F_s}$, is know as the scattering force, and the second is the dipole force $\mathbf{F_d}$, which is a non dissipative force.

For a near-resonant laser, $\mathbf{F_d}$ is negligible. Therefore, the effect of the laser on the atoms is described by $\mathbf{F_s}$, that is a dissipative force. In the approximated case in which we describe atoms as a two-level system this has the form [37, 38]:

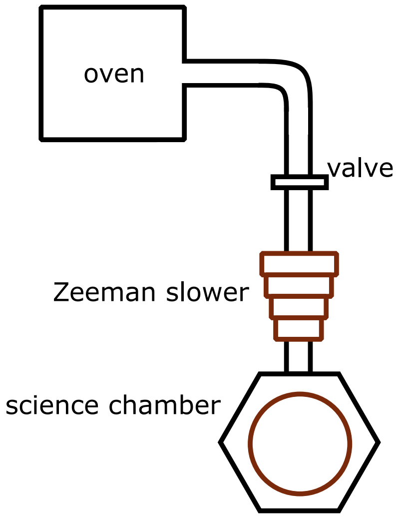

Figure 2.1: Experimental setup for laser cooling. A high temperature and collimated atomic beam flows from the oven to the rest of the experimental apparatus through a nozzle. The high velocity of the atoms is reduces by a Zeeman slower. Subsequently atom are trapped by a MOT in the science chamber.

$$\mathbf{F_s} = \hbar\mathbf{k}\frac{\Gamma}{2}\frac{I/I_{sat}}{1 + I/I_{sat} + 4\delta^2/\Gamma^2} \tag{2.2}$$

where $\mathbf{k}$ is the wave vector of the electromagnetic field, Γ is the atomic transition width, I the laser intensity and I_{sat} is the saturation intensity, namely the intensity for which the laser has excite $1/4$ of the atomic population into the excited state. $\delta = \omega - \omega_l$ is the detuning between the transition frequency ω and the laser frequency ω_l. This force arises from the total momentum gained by the atom after a series of absorption of photon from the laser beam (with a well defined momentum) and spontaneous emissions (that change the momentum of the atom by a random directed amount). This dissipative force can be used to cool down atoms.

In Appendix A it is reported the hyperfine structure of ^{6}Li atoms. In the experiment, two sources of laser are used, that are locked by subdoppler derivative spectroscopy to the D_1 and the D_2 fine transitions, respectively. A fine tuning of their frequency for different purposes is allowed by the use of Acusto-Optical Modulators (AOMs). For the cooling procedure, the D_1 and D_2 lasers are optimized to work on the $\left|2S_{1/2}, F = 3/2\right\rangle \rightarrow \left|2P_{3/2}, F = 5/2\right\rangle$ and the $\left|2S_{1/2}, F = 3/2\right\rangle \rightarrow \left|2P_{1/2}, F = 1/2\right\rangle$ transitions respectively. However, during the cooling procedure, it is possible that after a spontaneous emission atoms occupies the $\left|2S_{1/2}, F = 3/2\right\rangle$ state. This problem can be solved by *repumping* atoms in one the excited states, from which atoms can return to the $\left|2S_{1/2}, F = 3/2\right\rangle$ state via spontaneous emission. Thanks to the 228 MHz large separation between the two hyperfine levels of the ground state is possible to use the two sources of laser D_1 and D_2 lasers both for cooling and repumping. Fig. 2.1 shows the schematic representation of the experimental apparatus needed for the laser cooling of the atoms.

High-velocity atoms coming from the oven are initially slowed by the Zeeman slower [37]. Thanks to the presence of a spatially dependent magnetic field is possible to slow atoms with velocity up to $800m/s$ to around $50m/s$ by the use of a counter-propagating laser beam. Due to the Doppler effect, when the velocity of an atom is reduced, the Doppler shift of the laser frequency that this atom see changes; therefore it is expected that the laser beam is not resonant for all the slowing procedure. The role of the spatially dependent magnetic field is to keep the atom transition resonant to the laser frequency ω_l during the deceleration. This is allowed by the dependence of the atomic transition

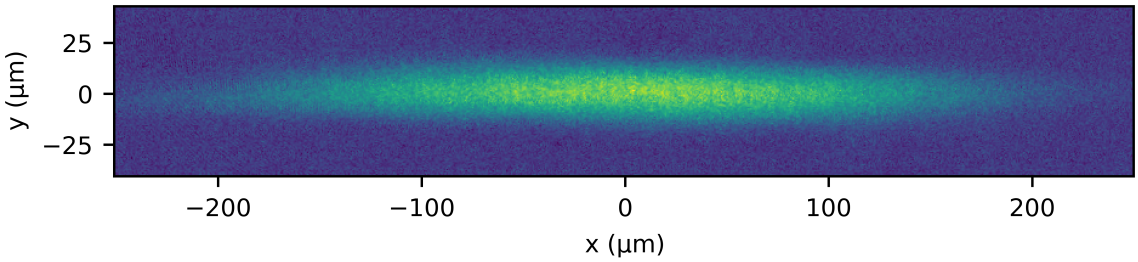

Figure 2.2: Atomic sample trapped by the combination of the IPG, Mephisto and $TEM_{0,1}$ laser beams in the unitary regime.

frequency by the magnetic field, effect known as *Zeeman effect*.

The slowed atomic beam is then captured in a magneto optical trap (MOT). Here the combination of a quadrupolar magnetic field produced by a pair of coils in a anti-Helmotz configuration and three couples of counter-propagating laser beam (one for each direction) create an effective viscous and harmonic force. The result is both a cooling and a trapping effect on the atoms. We trap $\sim 10^9$ atoms in the MOT with a temperature of $\sim 500\,\mu$K in 5-6 s. The lower limit of temperature reachable in a MOT is given by the Doppler temperature T_D estimated considering the energy exchange in a process of absorption of one photon by an atom. In the lithium case $T_D \simeq 140\,\mu$K. However, lower temperature are usually achieved by performing laser cooling in other alkali atoms [39], thanks to the Sisyphus cooling [37] [40]. In our sample this mechanism is repress by the unresolved hyperfine splitting of the $^2P_{3/2}$ level. However, a sub-Doppler cooling is realized by the implementation of grey molasses working on the D_1 transition [41]. With this process we are able to achieve a temperature of $\sim 50\,\mu$K.

2.1.2 Optical Dipole Trapping

The temperature reach with laser cooling techniques is not enough low to reach degeneracy in our system. Lower temperatures are achievable by the implementation of evaporative cooling, a technique based on use of dipole traps.

A far-off resonant laser beam exert a conservative force on an atom. In this case $\mathbf{F_s}$ is negligible respect to the $\mathbf{F_d}$. The potential energy associated to the conservative dipole force is

$$U(\mathbf{r}) = \frac{\hbar\Gamma^2}{8\delta}\frac{I(\mathbf{r})}{I_s}. \tag{2.3}$$

Therefore is possible to create a spatial dependent potential on the atomic sample by the use of out of resonance light with non homogeneous intensity as we have in the case of laser sources. The relation of $U(\mathbf{r})$ and $I(\mathbf{r})$ depends on the detuning δ, and in particular on its sign. In case of blue detuning ($\delta > 0$) the potential has the same sign of the intensity. As a consequence the positions $\mathbf{r}$ of maximum of intensity correspond to maxima of the potential $U(\mathbf{r})$. The atoms feel a repulsion from the laser beam. Blue-detuned laser can be used to create obstacle in sample or repulsive traps for atoms. On the other hand, a red-detuned laser ($\delta > 0$) create a minimum of the potential in the position of the maximum of the intensity. Using this kind of laser is possible to create attractive potential to trap atoms in the high intensity region of a Gaussian beam. These two type of trapping are known as optical dipole traps (ODT).

After the grey molasses stage described above, a high intensity infrared beam (IPG) is turned on and the a second stage of gray molasses and a first evaporation are performed. Evaporative cooling consists in the progressive reduction of the intensity of the trapping laser; in this procedure the more energetic atoms go out from the trap and, after a rethermalization of the system, the temperature decreases. In order to optimize the evaporation process, at the same time at which the IPG in turned on, we sweep the magnetic field to 832 G in the system, near to the Feshbach resonance between the $|F, m_f\rangle = \left|\frac{1}{2}, -\frac{1}{2}\right\rangle$ and $|F, m_f\rangle = \left|\frac{1}{2}, \frac{1}{2}\right\rangle$ states (see Fig. 1.2). The strong interactions allow to optimize the rethermalization process. For the realization of the evaporative cooling we lower the power of the IPG with an exponential ramp. After this a second high power infrared laser beam (Mephisto), crossed with the IPG by 14°, is turned on. At this point a second evaporation ramp is performed, decreasing the intensities of both the IPG and the Mephisto. At the end of this process we are able to obtain $\sim 10^5$ atoms per spin state at a temperature of 30 nK trapped in a cigar-shaped potential formed by the IPG and Mephisto.

Starting from this configuration, we use two laser blue detuned laser, obtain from the same Verdi V8 laser at 532 nm to manipulate the shape of the sample. One consists in a $\mathrm{TEM}_{0,1}$ beam. This beam is characterized by a waist in the vertical (z) direction of $\sigma_z = 8.73\,\mu$m and of $\sigma_{x-y} = 400\,\mu$m in the $x - y$ plane. The $\mathrm{TEM}_{0,1}$ beam is used to squeeze the sample in the z direction, as atoms are trapped in the minimum of intensity. By tuning his intensity, it is possible to study systems with different vertical dimensions. However, the system is a oblate 3D system. The trap frequency in the z direction ν_z is adjusted for the different regimes in order to keeping $h\nu_z/EF \sim 0.05$. Fig. 2.2 shows the atomic sample trapped using the combination of the IPG, Mephisto and $\mathrm{TEM}_{0,1}$ in the unitary regime.

The second blue-detuned laser is used to create arbitrary optical potential with a digital micromirror device (DMD), in order to manipulate the geometry of the system in the $x - y$ plane, as it will be further explained in the next section. When the atoms are loaded in the DMD potential, the Mephisto and IPG are switched off, and the system in trapped by the combination of the $TEM_{0,1}$ and the DMD pattern. The result is a homogeneous system in the $x - y$ plane.

2.2 High resolution imaging and arbitrary optical potentials

In order to detect the density distribution of the sample, we perform absorption imaging. A resonant pulse is shone on the system and then it is collect on a camera. The presence of atoms is marked by a shadow in the acquired light pattern, due to the absorption of photon by atoms. In our system is is possible to imaging atoms by shining a pulse both in the vertical and in the horizontal direction.

The vertical imaging is the most sophisticate. His main constituent is a high-resolution microscope objective. It is designed to feature the same focal point for both resonant light at 671 nm and blue-detuned light at 532 nm. In this way it is possible to use it for both imaging the cloud and for shining arbitrary optical potential with the DMD. For both the wavelength it is used for, the resolution of the imaging system is below 1 μm. With a lens of focus $f = 1000$ mm, the imaging light is focused on an Andor IXon3 EMCCD camera, of 13 μm x 13 μm pixels. The total magnification for the vertical imaging system is $M = 21.8$. More detailed information about the vertical imaging system and on the high resolution objective are discussed in [42].

The horizontal imagining system is formed by a telescope providing a magnification of 6.87, and the image are acquired by a an Andor Ultra camera, of 16 μm x 16 μm pixels. Another Stingray camera with 0.5 magnification can be placed along the horizontal imaging setup in order to image the cloud in the MOT.

Both the vertical and the horizontal camera are set on the Fast Kinetic Series (FKS) acquisition mode, allowing to take a sequence of a few images with a short delay time on the order of 200 μs. In order to detect the density distribution of the system, both for the horizontal and the vertical imaging we take three images. The first image is taken collecting the light shone on the atom sample, the second is taken in absence of atom, while the last is obtain without shining any light and is used to

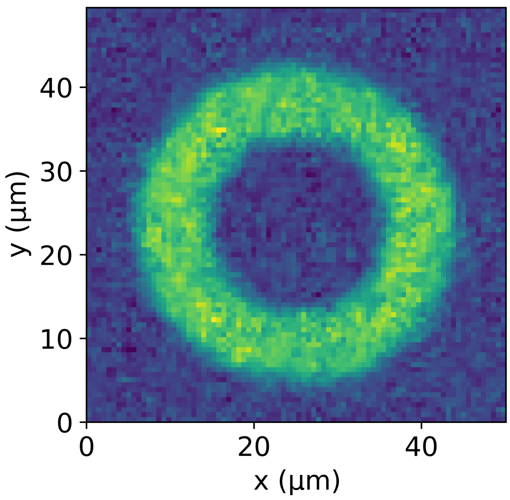

Figure 2.3: Ring-shaped superfluid in the BEC regime. Thanks to the DMD it is possible to create an annular potential for trapping the atoms.

remove the background from the other two. In the first and second images, we use pulses $4\,\mu$s long with an intensity $I \simeq 3I_s$ of resonant light.

This procedure is a destructive imaging. Therefore every images taken correspond to a different realization of the sample starting from the atomic beam coming out from the oven. Therefore is impossible to follow the dynamic of a single sample.

As I have already mentioned, the vertical imaging setup is used also for the realization of arbitrary optical potential using a DMD. This object is composed by an array of 1024 x 768 squared micromirrors with a side of $13.68\,\mu$m. Using an external voltage, it is possible to control the tilt of each micromirror. In particular, two tilt states are available, giving the opportunity to reflect the light on the atom when the mirror is in one state, or to disperse the light when it is in the other configuration. Therefore, by controlling the state of each mirror is possible to arbitrary shape the intensity profile of a laser beam and of the corresponding optical potential on the atomic sample. The reflected light passes thought a first telescope to be then focused on the atomic cloud by the microscope objective. This setup provide a total demagnification of 55, so that 1 DMD pixel has a $0.25\,\mu$m size on the atomic cloud.

Finally, the DMD can also create dynamic potentials. In particular it is possible to load on the DMD a discrete series of images that will be shone on the sample at different time during the same realization. This possibility is useful for the realization of persistent currents in the ring geometry as we will see in the next sections. The timing between two different imaging is tunable. The maximum frame rate allowed is 22 kHz, corresponding to a time between the images of $44\,\mu$s.

Thanks to high-resolution vertical setup, we are able to both create arbitrary optical potential and image the atomic sample with very high spatial resolution.

2.2.1 The ring-shape potential

Fig. 2.3 shows the ring-shaped fermionic superfluid obtained with a proper potential created by the DMD in the BEC regime. In particular the sample in the figure has an inner radius of $9.94\,\mu$m and an external one of $20.22\,\mu$m. This is the geometry mostly use for the work presented in this and the next chapters. The system is trapped by the combination of the $\mathrm{TEM}_{0,1}$ in the vertical direction and the DMD pattern, resulting a quasi-homogeneous density profile.

The thermodynamic properties of ring superfluids are calculated as follow. Under the polytropic approximation [43, 44], the density profile for a spin state over the BEC-BCS crossover is given by

$$n(r,z) = \left(\frac{\mu}{g_\gamma}\right)^{\frac{1}{\gamma}} \left(1 - \frac{z^2}{R_z^2} - V_{ring}(r)\right)^{\frac{1}{\gamma}} \tag{2.4}$$

where R_z is the Thomas-Fermi radius in the z direction and $V_{ring}(r)$ is the potential create by the DMD pattern. γ is the polytropic index, that takes the values $\gamma = 1$ in the BEC limit and $\gamma = 2/3$ in the BCS and UFG regimes [44]. g_γ is a prefactor depending on the interaction regime. In particular $g_{BEC} = 4\pi\hbar^2 a_M/2m$, with $a_M = 0.6a_s$, for $(k_F a_s)^{-1} > 1$, $g_{UFG} = \xi\frac{\hbar^2}{2m}(6\pi^2)^{3/2}$, where ξ is the Bertsch parameter taking the value of 0.37 at the unitarity, for $-1 < (k_F a_s)^{-1} < 1$, $g_{BCS} = \frac{\hbar^2}{2m}(6\pi^2)^{3/2}$ for $(k_F a_s)^{-1} < -1$. Approximating the system as homogeneous in the $x-y$ plane, we consider $V_{ring}(r) = 0$ for $r \in (R_{in}, R_{out})$ and $V_{ring}(r) = +\infty$ otherwise.

Integrating the density profile in Eq. 2.4 over the space, we obtain the total number of particle for a spin state from which we compute the chemical potential: [45]

$$\mu = \left(\frac{\Gamma(\frac{1}{\gamma}+\frac{3}{2})}{\pi^{3/2}\Gamma(\frac{1}{\gamma}+1)} \frac{\sqrt{m}\omega_z N g_\gamma^{1/\gamma}}{R_{out}^2 - R_{in}^2}\right)^{\frac{2\gamma}{\gamma+2}} \tag{2.5}$$

where Γ is the Gamma function. The resulting Fermi energy is given by

$$E_F = 2\hbar\left(\frac{\hbar\omega_z N}{m(R_{out}^2 - R_{in}^2)}\right)^{1/2} \tag{2.6}$$

2.3 Excitation of persistent currents

Persistent currents in a toroidal superfluid have been observed in both bosonic [46, 47] and fermionic atomic condensed gases [48]. It is possible to create excitation of persistent flow in a ring-shape trap in different ways, like transferring momentum with a two photon transition [46] or by stirring an obstacle along the ring [48, 49]. In our system, we excite persistent current in a ring using a *phase imprinting* method based on a spatial dependent optical potential [50].

2.3.1 The phase imprinting method

To realize persistent currents in our system we use the DMD to imprint a well defined phase on the atomic sample. As we have already seen, a far off resonance laser frequency acting on an atom, create a optical potential proportional to the intensity of the light (Eq. 2.3)

Due to the ring-shape geometry, it is convenient to study the problem in cylindrical coordinates (r, θ, z). Assuming that the light comes from the z direction, is possible to describe our sample like a 2D system depending on r and θ.

If the optical potential in Eq. 2.3 acts for a time Δt much smaller than the typical timescales of the system, setted by $\hbar/\mu$, it is possible to neglect the atomic motion caused by this potential. However the presence of U determinate an extra phase factor in the normal phase evolution of the system's wave function $\psi(r, \theta, t)$. Therefore, after a pulse of duration Δt, the wavefunction is changed to [50]:

$$\psi(r, \theta, t_0 + \Delta t) = e^{-\frac{i}{\hbar}U(r,\theta)\Delta t}\psi(r, \theta, t_0) \tag{2.7}$$

Hence, in the limit of small Δt, the potential will simply add the phase $\phi(r, \theta) = -U(r, \theta)\Delta t/\hbar$ to the ground-state wave function ψ. Using a DMD, it is possible to realize an on demand potential $U(r, \theta)$

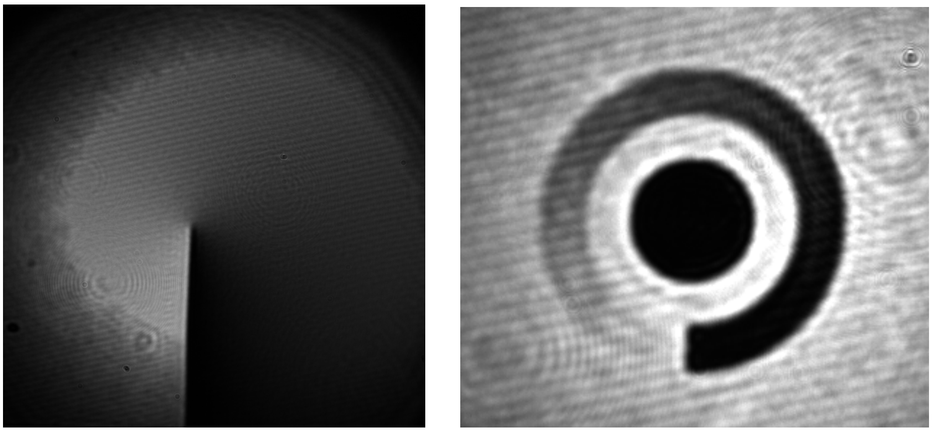

(a) (b)

Figure 2.4: (a)Light pattern with linearly increasing intensity along the azimuthal direction. (b)Light pattern used for the excitation of persistent current in the ring. Here is shows how the light pattern realized by the DMD is used both for create a ring trap and for imprint a phase pattern. Neglecting for the moment the internal black disk, whose need is explain in the next section, light create a repulsive ring-shaped trap consisting in a bright inner circular barrier and in a outer light background. In the middle, corresponding to the region where atoms are present, intensity of the light increases linear by changing the angular coordinate, implementing the procedure just described.

by creating a dependence of the intensity on the position.This allows for creating persistent current in our sample, by the realization of a linearly angular dependent potential $U(r,\theta) = U_0\theta$. In this case the phase of the system after a phase imprinting pulse is given by

$$\phi(r,\theta) = -\frac{U_0\Delta t}{\hbar}\theta \tag{2.8}$$

Considering Eq. 1.27 for the velocity field, for a phase pattern given by Eq. 2.8, the system acquires a velocity described by:

$$\mathbf{v}(r,\theta) = -\frac{U_0\Delta t}{\hbar}\frac{1}{r}\hat{\theta} \tag{2.9}$$

Therefore the system starts to flow through the ring with a velocity in modulus constant along ϕ and that decrease like $1/r$. A current is created. As I explain in detail in the following section, in this way is possible to excite currents in the system with a velocity field as in Eq. 1.31, with a circulation w. I will also refer to w as the winding number of the system

Fig. 2.4a shows the considered light pattern with a linearly increasing intensity along the azimuthal direction as it is created by the DMD. However, the actual patter used for the phase imprinting in our system is showed in Fig. 2.4b. Here the light pattern realized by the DMD is used both for create a ring trap and for imprint a phase pattern. Neglecting for the moment the internal black disk, the need of which is explained in the next section, the light creates a repulsive ring-shaped trap consisting in a bright inner circular barrier and in a outer light background. In the middle, corresponding to the region where atoms are present, the intensity of the light increases linearly along the azimuthal coordinate, implementing the procedure just described.

This method allows for the realization of persistent currents in a more controllable and reproducible way respect to others. By changing the interval Δt during which the light is shone on the sample, it is possible to manipulate the velocity field. In particular for longer Δt atoms gain a higher velocity.

However the validity is limited to values of Δt much less respect to the typical timescales of the system, namely for $\Delta t \ll \hbar/\mu$.

For imprinting bigger velocity without increase to much Δt is also possible realize *'multi gradients'* imprinting patterns, in which the intensity of the laser present n linear ramp moving through the angular direction, where n is a natural number. In this work the gradient showed in Fig. 2.4 is mostly used, but also gradient with $n = 2$ and $n = 4$ have been implemented in particular for excite larger winding number. However use of larger n gradient pattern reduce the manipulation level of the method: for example, for the $n = 2$ case, it is not possible to populate the state $w = 1$ with high precision as in the single gradient case. Therefore we constrain the usage of multiple gradient only for imprinting high circulation states. The excitation of high circulation is achieved also by the use of multiple imprinting pulses,shining the same simple gradient pattern for more than one pulse. Multiple pulses are separated by 10 ms in time, in order to let the system relax. By using a single pulse and a simple gradient pattern for the imprinting procedure, we are able to imprint circulation up to $w = 6$.

In the realization of this method we are also limited by a minimum Δt; due to technical limitation of the DMD, we cannot imprint a time Δt less than $50\,\mu$s, corresponding to the minimum interval in which the DMD can change the light pattern shined on the atoms.

2.3.2 Experimental procedure

The protocol used in the experiment to excite currents in a ring is showed in figure Fig. 2.5. The first image of the DMD is shined on the atom in the cigar trap (Fig. 2.2). then we ramp down the Mephisto and the IPG and atoms are loaded in two semicircle separated by a $2.4\,\mu$m barrier (Fig. 2.5a). At this point the system is trapped in the vertical direction by the $TEM_{0,1}$ and the light pattern created by the DMD. The result is a quasi-homogeneous system in the $x - y$ plane with arbitrary geometry created by the DMD. The barrier in the sample create a line with no atom, cause his height is well above the chemical potential. The presence of this barrier is planned to stop the possible flow that can be crated by the loading from the cigar trap to this configuration. Now a circular barrier is adiabatically ramped up(Fig. 2.5b-c), by shining with the DMD a sequence of fifteen images with an increasing intensity of this barrier, separated by 0.1 ms. After 40 ms waiting, the barrier used to stop the flow is ramped down (Fig. 2.5d) with a sequence of fifteen images, one every 5 ms. At the end the final configuration is obtain and atoms are trapped in a ring and an inner circle(Fig. 2.5e), which is used for determine the circulation state of the ring superfluid, as I will explain in the next section.

Every parameter is chosen in order to create a still gas at the end of this routine. Persistent currents in the sample are created by the application of the phase imprinting method in the external ring in this final configuration.

2.4 Persistent Currents

The previous section describes how it is possible to create currents in our system, allowing the creation of a velocity field as in Eq. 2.9. The method used gives the possibility of tuning the velocity's modulus as we like. On the other hand persistent currents in a ring must be described by Eq. 1.31, that shows a quantization of the velocity. Despite this two equations look non consistent, they are both true. The discrepancy between them is solved as described in the following. Immediately after the imprinting-pulse, the velocity field is described by equation 2.9, and no quantization is required. In a time on the order of $\sim 1ms$ this density depletion is observed to disappear, and the system rearranges in a velocity field in the form 1.31. Therefore at the end a persistent current with a defined circulation w is created.

Energy argument lead to the following considerations. As pointed out in [47], free energy against the total angular momentum per particle is characterized by local minima in proximity to values of $L/N = w\hbar/2$, corresponding to the quantized velocities 1.31. Other values of L are possible, in

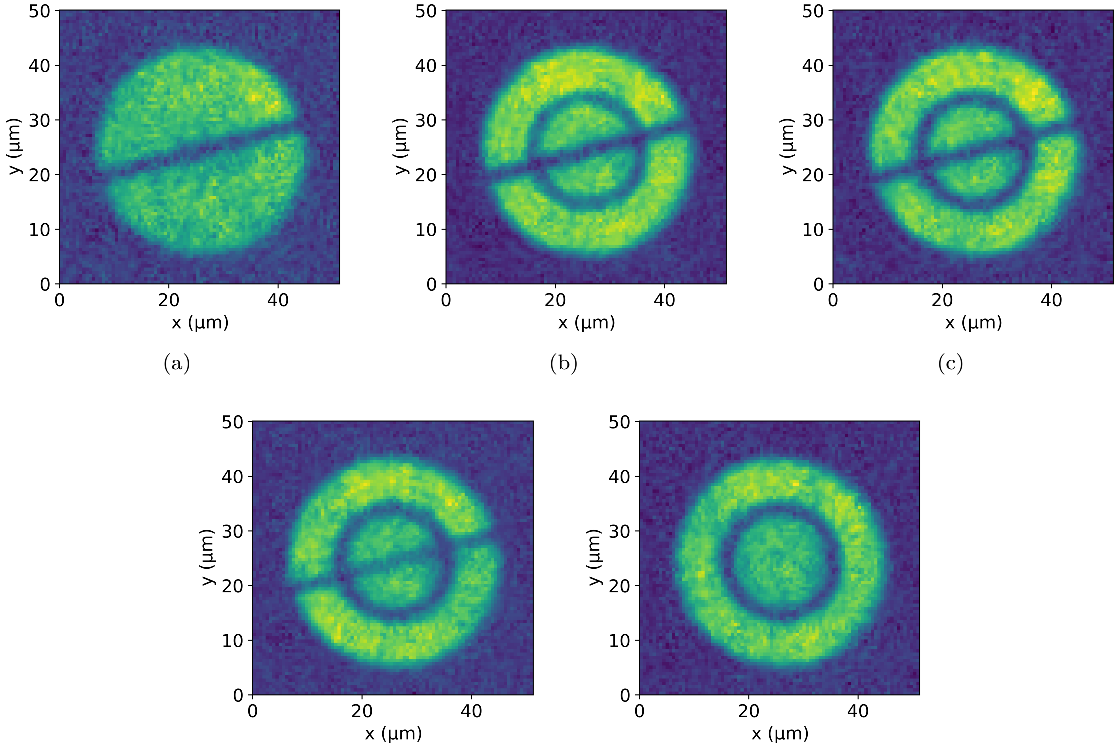

(a) (b) (c) (d) (e)

Figure 2.5: Experimental protocol implemented for the excitation and observation of persistent currents. From the cigar shaped trap squeezed in the vertical direction by the $TEM_{0,1}$ laser, atom are first trapped in two semicircle (a), after that IPG and Mephisto are ramped down. From this moment, the system is trapped by the combination of the $TEM_{0,1}$ and the light pattern created by the DMD. The result is a quasi-homogeneous system in the $x-y$ plane with arbitrary geometry created by the DMD. The presence of a barrier is designed in order to stop possible flow arising from the loading of this configuration from the cigar trap. After 200 ms we start to ramp up a circular barrier (b). This process is done in a sequence of fifteen different images from the DMD separated by 0.1 ms and we obtain the configuration in (c). After 40 ms we start to ramp down the linear stopping barrier (d). The final configuration (e) consist in an atomic sample trapped in an external ring and an inner disk, used for the measurement of the circulation w in the ring. At this point the phase imprinting protocol is performed in the external ring.

particular immediately after the phase imprinting procedure. In this case system tend to decay in to one of the local minima. Therefore despite phase imprinting can create an arbitrary velocity, the final results of the procedure is to excite the system in a state with a quantized circulation w. Increasing the imprinting time Δt the local minimal to which the system tends to evolve changes. Thus the resulting circulation w is expected to show a step-like behaviour against the imprinting time. This is actually what is observed in our system, at least for low w [45]. For higher circulations, the method reduces his reproducibility and the step-like trend his lost due to technical limitations. The energy corresponding to this local minima increase for bigger w. Therefore circulation of $w > 0$ are expected to be metastable state.

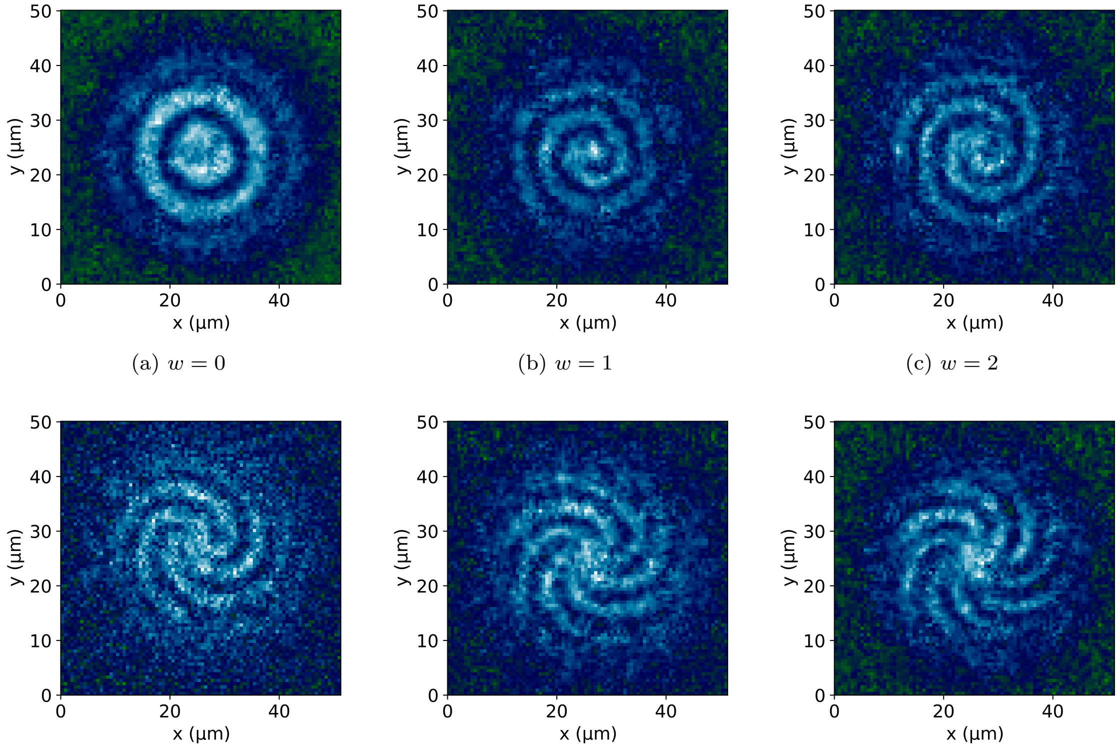

(a) $w = 0$ (b) $w = 1$ (c) $w = 2$

(d) $w = 4$ (e) $w = 6$ (f) $w = 8$

Figure 2.6: Detection of the circulation state w in the ring. To quantify the circulation state of the ring we let it interfere with the inner circle performing a TOF free expansion measurement. The phase ϕ_1 of the inner disk is constant, while the phase ϕ_2 of the external ring depends on the circulation $\phi_2 = w\theta$. The interference measurement allow to get information about the relative phase between the two system. When no flow is excited in the external ring, we obtain a density modulation as is shown in (a) formed by concentric circumferences. On the other hand, when a circulation in excite in the ring, the phase different between the two condensates depends on the angular position θ and the interference pattern is formed by spirals. In particular, the circulation state of the condensate in the ring can correspond to the number of the arms of the observed spirals. The images are obtained with a TOF of 1.3 ms and are relative to the observation of persistent currents in the BEC regime.

2.4.1 Detection of persistent currents

Early work on currents in bosonic ring superfluids use simply time-of-flight (TOF) techniques to detect them [46]. In this methods, the trap apparatus is switched off abruptly and the atomic sample evolves in free space for a time usually in the order of 1 - 10 ms. The presence of non-zero circulation is observed by the presence of a hole in the density after the expaThe dimension of the hole measures the winding number: it is bigger for higher circulation states. However, this method is not a good way to study circulation number in our case, because it does not allow to distinguish very well state with very high w. An other way to quantify the number of circulations in the system relies of the possibility to detect the phase of the system, that is directly connected to the velocity field. This is possible by performing interference measurements [51, 52, 53].

Interference between condensed systems is one of the most fascinating effects related to the phase coherence of these systems, that arises from the possibility to describe them by a macroscopic wave function in the form of Eq. 1.26. For the one particle case, the wave nature leads to interference effects; a famous example is the double slit experiment. An analogous in many-body systems consists in the interference coming from two bosonic condensed system that overlap in a TOF free expansion [54]. As an example, we consider the 1D problem of two bosonic condensed systems in harmonic traps described by Gaussian wave function $\psi_1(\mathbf{r},t)$ and $\psi_2(\mathbf{r},t)$ centred in the points $r = \pm d/2$, with global phase ϕ_1 and ϕ_2. The density profile is given by:

$$n(r,t) = |\psi(r,t)|^2 = |\psi_1(\mathbf{r},t) + \psi_2(\mathbf{r},t)|^2 = |\psi_1(\mathbf{r},t)|^2 + |\psi_2(\mathbf{r},t)|^2 + 2\,\mathrm{Re}\{\psi_1(\mathbf{r},t)\psi_2^*(\mathbf{r},t)\} \tag{2.10}$$

where $\psi(r,t) = \psi_1(\mathbf{r},t) + \psi_2(\mathbf{r},t)$ is the total wave function of the system. The last term in this equation is responsable to the emergence of an interference pattern due to the overlapping of the two wave functions. Considering the free expansion of the two wave packets, in the limit of a long TOF t is possible to show that [55]

$$\mathrm{Re}\{\psi_1(\mathbf{r},t)\psi_2^*(\mathbf{r},t)\} \propto \cos\left(\frac{mrd}{\hbar t} + \phi_1 - \phi_2\right) \tag{2.11}$$

Therefore the density profile shows an interference pattern caractherizzed by a wavelength $\lambda^{-1} = 2\pi\frac{mrd}{\hbar t}$. Moreover, this density modulation depends on the initial difference between the two global phases of the two systems $\phi = \phi_1 - \phi_2$. This last consideration is exploited in our detection of persistent currents. This is the reason why we prepare the system not only with an external ring but with also the presence of an inner disk (see Fig. 2.5e). To quantify the circulation of our system we realize a TOF expansion letting the two system overlapping. For each direction θ is possible to consider the expansion like the 1D problem just explained. Therefore after a free expantion t the density distribution has the same form of Eq. 2.10. In particular the interference term can be written as:

$$\cos\left(2\pi\frac{r}{\lambda} + \phi_1(\theta) - \phi_2(\theta)\right) \tag{2.12}$$

We refer to ψ_1 as to the internal disk, and ψ_2 to the external ring. If no circulation is excite in the system, both ϕ_1 and ϕ_2 do not depend on θ and the interference pattern is the same in all the directions. Therefore a TOF measure will give rise to concentric circles in the imaged density, corresponding to the series of peaks and minima of the interference along r.(see Fig. 2.6a).

When a circulation w is excited in the ring, while the phase ϕ_1 is still constant, the phase ϕ_2 increases linearly with the angular direction, namely $\phi_2(\theta) = w\theta$. So the interference term take the form :

$$\cos\left(2\pi\frac{r}{\lambda} + \phi_1 - w\theta\right). \tag{2.13}$$

Therefore the peaks of interference pattern are shifted for different θ directions, in particular they follow a trend like $r_{peak}(\theta) = n\lambda - (\phi_1 - w\theta/2\pi)\lambda$, where n is an integer and indicate the order of the peak. The results is thus a linear shift of the interference pattern along the θ direction and thus finite circulations in the ring results as spirals in the TOF interferogram. Moreover the phase term is given by $\phi = \phi_1 - w\theta$ in this case. For a fixed radial position r, Eq. 2.13 shows a periodicity in the angular dimension of $2\pi/w$. Therefore the system will show spirals with as many arms as circulation w in the ring. In this way is possible to determine the circulation state of the system by simply counting the number of arms of the spirals in the TOF interference pattern. Fig. 2.6 shows the interference pattern obtained for different circulations.

2.4.2 Persistent currents in the BEC-BCS crossover

In the study of persistent currents we mainly concentrate in the in three regimes of fermionic superfluidity, whose values of $1/k_F a_s$ are reported in Tab. 2.1.

	B	$\frac{1}{k_F a}$
BEC	702 G	3.6
UFG	834 G	0.0
BCS	862 G	−0.4

Table 2.1: Values of $1/k_F a$ and of the corresponding magnetic field B for the three regime of fermionic superfluidity studied in the persistent currents topic.

The interference measurement proposed above is a good method for the determination of the circulation state of the system. However, it has been observed that the interference pattern in fermionic superfluids strongly depends on the value of $1/k_F a_s$ [56]. In particular, increasing the magnetic field B, the visibility of the interference drops down very quickly as soon as we reach the strongly interacting regime $|1/k_F a| < 1$, preventing the direct use of the interference method for the study of persistent currents in the unitary and the BCS regimes, as in the strongly BEC regime.

The BEC regime we studied is characterized by $1/k_F a > 1$. As a consequence the interference pattern is well visible in this condition. By contrast, in TOF measurements in the UFG and BCS regimes no spirals is present in the interference pattern. In order to study of persistent currents in this regimes, we first excite circulation states at the corresponding magnetic field. To obtain the circulation state, we perform an adiabatic sweep of the magnetic field in 50 ms and after other 10 ms of equilibration, we do a TOF measurement. The target magnetic field of the sweep is set to the one of the BEC regime, for which the interference pattern is well visible.

This protocol allows to detect of presence of currents in the BEC-BCS crossover. In order to study the persistence of the currents, the detection is performed with the following protocol. After the excitation of current of the wanted circulation w, the system is let evolve for a variable holding time t. After the evolution a TOF image is taken. As I have just explained, in the UFG and BCS regimes, after the time t we sweep the magnetic field to the BEC regime, and the TOF imaging is realized after other 60 ms. The holding time t is varied from few milliseconds to few seconds. Persistent currents in the sample are observed up to $w = 8$ in the BEC and UFG and up to $w = 6$ in the BCS regimes. For this value of circulation, no decay of w is observed for holding time below or of the order of the typical lifetime of the sample in the different regimes. Due to the low temperature reached in this experiment, collision between atom and interaction with the laser that create the trap can easily excite atom out of the condensate. As the condensed atom number decrease, the visibility of the interference pattern become worst. Therefore the persistent of currents are detectable as long as the contrast of interference fringes is sizeable.

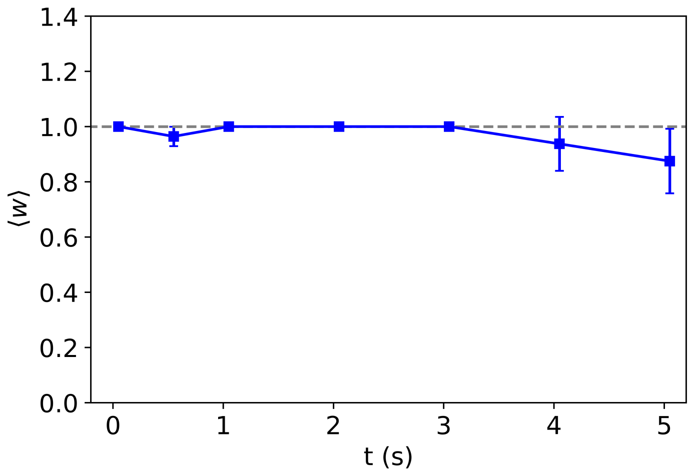

Figure 2.7: Time evolution of the average winding number w for a system initially prepared in $w = 1$. The circulation is stable up to 3 s. For longer holding time a small dacay of the current is observed. For longer time circulation starts to decay. However this timescale correspond to the typical lifetime of the sample in the UFG regime.

2.4.3 Long time behaviour

As we already pointed out, quantized persistent currents in a ring are metastable states, corresponding to local minima of the free energy. The absolute minima correspond to the state with $w = 0$, thus to a state in which the system is still. It is therefore interesting to study the timescale for the decay of this metastable states, in other word, to pick out how long persistent are these currents. For study this, we analysed the time dependence of the winding number in the unitary regime for a starting circulation of $w = 1$ for long holding time.

Fig. 2.7 shows the time evolution of the winding number of the system, obtained from the average of 20 repetition for each value of the holding time t, error bars are the standard deviation of the mean. The circulation is stable up to 3 s. For longer holding time a small decay of the current is observed. However, this time are on the order of the system lifetime in this regime, therefore this supercurrent is persistent up to the life of the sample. For larger holding time the condensed atom number is very low.
As is shown in Fig. 2.8 the interference pattern for holding time larger than 3 s is not well defined and his low visibility make the circulation state difficult to determinate in this case. However, in mostly of the case the circulation state is observed to survive also up to 5 s. Finally, Fig.2.8h shows the TOF image of a particular repetition for a holding time $t = 6$ s for which the interference pattern reveals that the circulation is still present in our sample. This long time behaviour can be important for future investigation or technological implementations

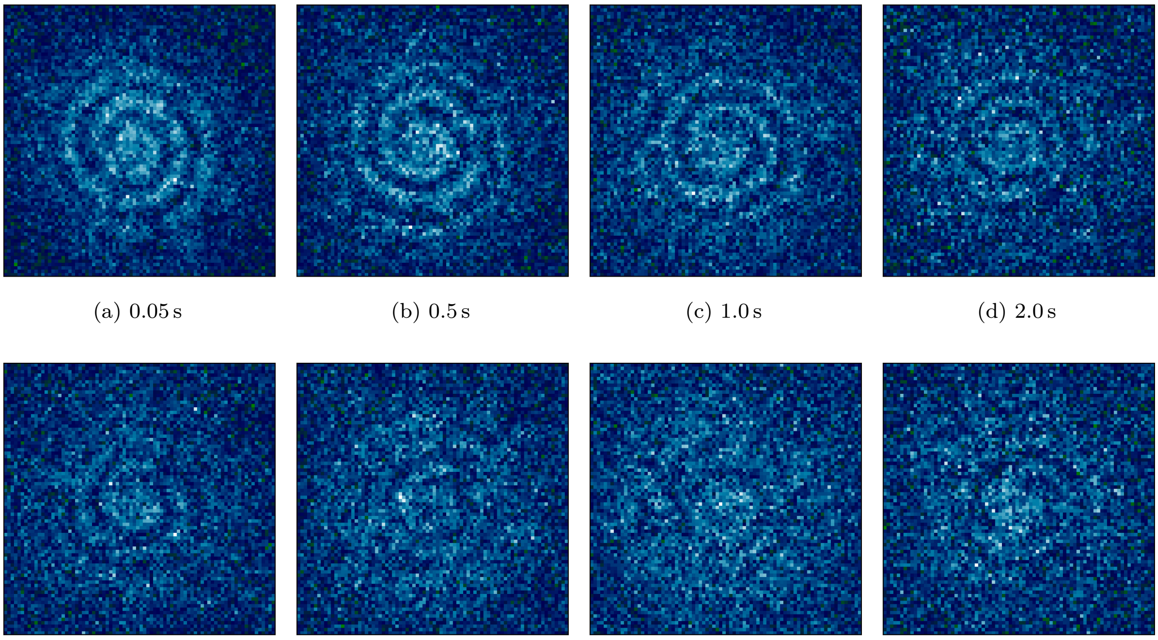

(a) 0.05 s (b) 0.5 s (c) 1.0 s (d) 2.0 s

(e) 3.0 s (f) 4.0 s (g) 5.0 s (h) 6.0 s

Figure 2.8: Time evolution of the interference pattern in the 1 circulation case in the unitary case. Imaging is performed after a sweep to the BEC regime. Subcaptions indicate the holding time between the phase imprinting procedure and the starting of the sweep. Spirals are well defined up to 2 − 3 s. Data of 4 s and 5 s are not really reliable for the low contrast of the interference pattern. However, some images reveal the persistence of circulation up to this time.

2.5 Additional effects of the phase imprinting

The phase imprinting method allows to excite persistent currents with a high degree of reproducibility and tunability. However, the practical implementation in our system has some further effects due to technical imitations with respect to the ideal case method described above. The most important are the creation of a density depletion and the nucleation a vortices immediately after the imprinting procedure.

2.5.1 Density depletion

If an image is taken a few microseconds after the phase imprinting procedure, a depletion and an accumulation of the density appear close to the gradient discontinuity. The origin of them rely on the actual intensity profile of the DMD for imprinting procedure. As we already explained, a linear increase of the intensity profile moving in the angular direction θ, is required. Therefore the light go from $I = 0$ at $\theta = 0$ to his max value I_{max} for $\theta = 2\pi$; around the position $\theta = 0 = 2\pi$ a jump discontinuity of the intensity is required. Obviously this is impossible to achieve experimentally, due the finite resolution of the system. As a result, the maximum of the intensity is connected to the minimum through a gradient with opposite sign respect to the one properly used for the imprinting procedure. As a consequence the imprinted phase will induce to the atoms in this region a velocity in the opposite direction respect to the desired rotation. To avoid this problem the presence of a barrier in proximity of the *antigradient* has been proposed [50]. However the high resolution of our system

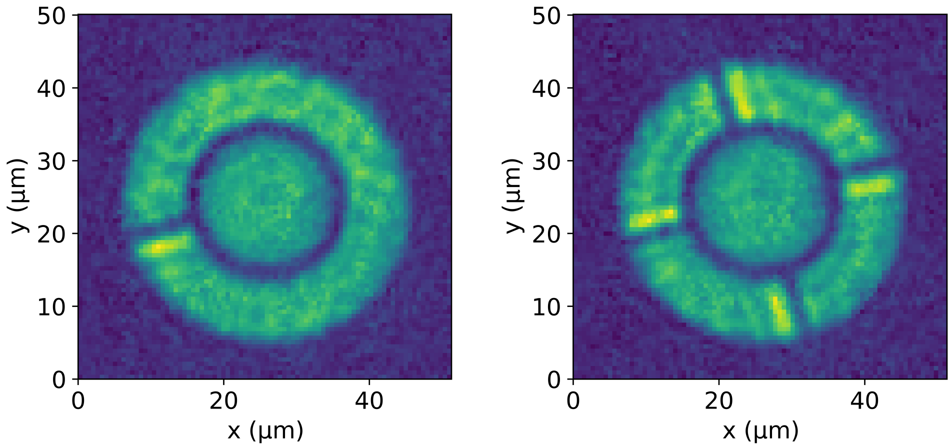

(a) 1 gradients

(b) 4 gradients

Figure 2.9: Density profile of the sample observed immediately after the phase imprinting procedure. Due to the finite resolution of the imaging system, the imprinting pattern present an antigradient profile between the maximum and the minimum intensity. The atom in this region are excite with high velocity. As a result, a density depletion and a corresponding accumulation are observed after the imprinting procedure. The non homogeneity of the system disappear in a few ms. In this images are show the effect of the imprinting pattern with $n = 1$ (a) and $n = 4$ (b) gradients for the BEC regime.

allows to reduce the problem concentrating this antigradient in a small region of $\Delta\phi \sim 0.2$rad and we succeed in creating persistent currents without the use of a barrier. However, the antigradient is much sharper with respect to the imprinting gradientand creates a depletion and a corresponding accumulation of density. As it is expected for longer imprinting time , a deeper depletion (and a larger accumulation) is observed. Fig. 2.9 shows this effect for an imprinting time of 100 µs in the BEC superfluid for different number of gradient used in the imprinting procedure. For larger gradient number, the system is more perturbed, and therefore we expect the realization to be more similar to the theoretical protocol for low gradient number. The density perturbation disappears in few ms [45].

2.5.2 Vortices nucleation from phase imprinting

A more problematic additional effect generated by phase imprinting is the creation of vortices in the ring. The decay of the density depletion generated by the antigradient is followed by the formation of density waves in the sample. This density excitations are able to create vortices close to the inner radius of the ring, Despite they do not affect the persistence of the currents, their presence can be a problem during the investigation of the vortices formation in case of supercurrents decay or in the realization of the quantum Kelvin-Helmholtz instability that are presented in the next chapters.

In Fig. 2.10 it is shown the number of vortices arising from the imprinting procedure for different Δt. Data are taken 20 ms after the first pulse, for an imprinting pattern with one gradient. Data relative to the cases in which one pulse (green curve) and two pulses separated in time by 10 ms (blue curve) are performed. Data are obtain from 20 repetition of the measure. Point are obtained from the average value of the observed number of vortices, the error is the standard deviation of the mean. The number of this *'spurious vortices'* is observed to increase for longer imprinting time. Moreover this number in the two pulses case is approximately double respect to the single pulse case. Anyway, the imprinting procedure creates vortices even for low values of Δt. The creation of vortices from the imprinting procedure has been confirmed by numerical simulations. However,in this case, vortices formation is observed only for imprinting time able to excite circulation states $w > 4$.

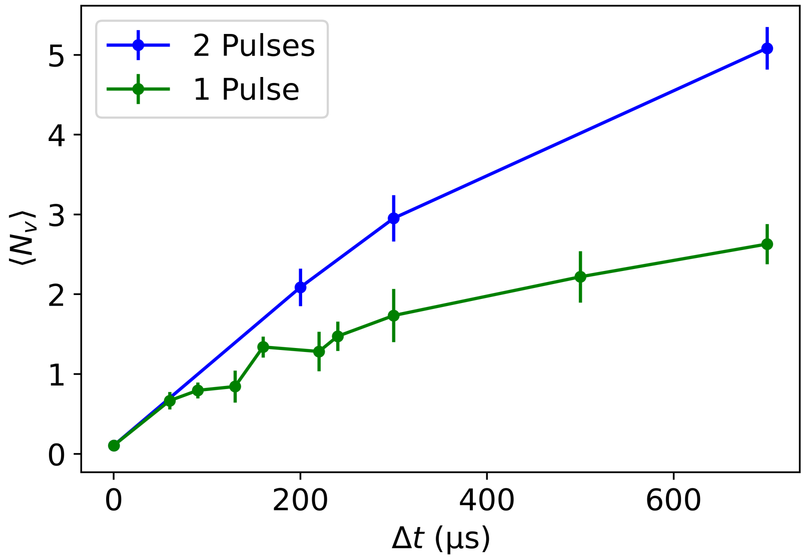

Figure 2.10: Number of vortices in the ring after an imprinting time Δt. The green and blue curve represent respectively the cases in which one and two imprinting pulse are performed. In both the single gradient pattern is used. An increase of the number of vortices for longer imprinting time is observed. Anyway, Spurious vortices are present even for low values of Δt. Images are taken 20 ms after the first pulse.

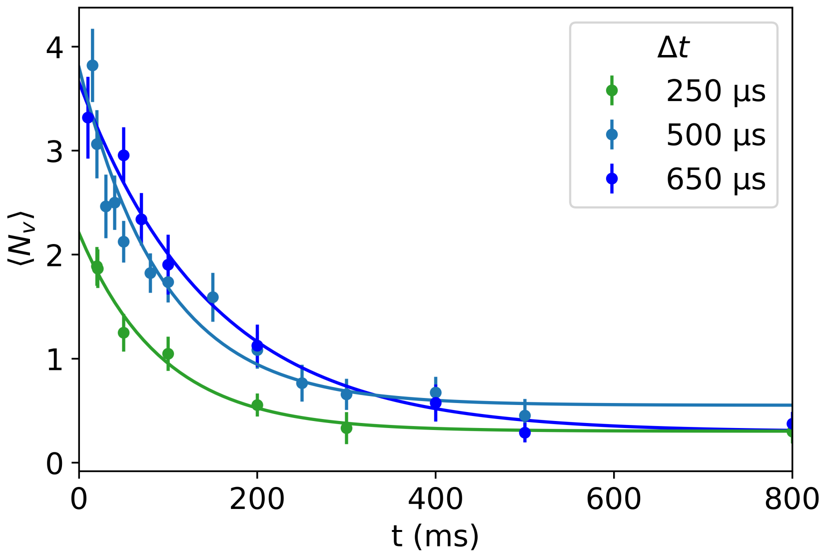

Figure 2.11: Exponential decay of the number of vortices in the sample arising from the imprinting procedure. The legend indicates the imprinting time corresponding to different colours. An exponantial fit $\sim e^{-t/\tau_{decay}}$ is performed, the resulting τ_d is around $\sim$ 100 ms for the three cases. After 300 ms the average number of spurious vortices are below 1 for all the cases.

However, as shown in Fig. 2.11 the number of vortices in the ring is observed to exponentially decreases in time. Here the experimental data of the number of vortices in the external ring as a function of the holding time t for different imprinting time are plotted: $250\,\mu$s (the green circles in the plot), $500\,\mu$s (the light blue circles) and $650\,\mu$s (the dark blue circles). In all the three case the number of spurious vortices is observed to decay exponentially with a decay constant τ_d on the order of 100 ms. Is important to notice that after 300 ms the average number of spurious vortices are below 1 in all the cases.

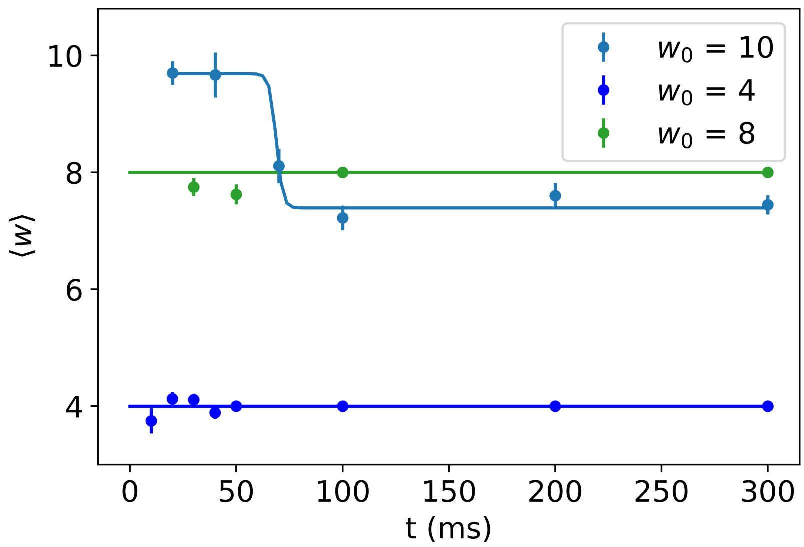

Figure 2.12: Evolution of the winding number in the BEC superfluid for different initial circulation $\langle w_0 \rangle$. The maximum stable circulation is observed to be $\langle w_0 \rangle = 8$. Higher values of initial circulation decays to this values. The light blue curve show the behaviour of an state in the initial circulation of $\langle w_0 = 10 \rangle$. An sigmoid fit is performed. The circulation of the system is observed to decay in tens os ms. The green and the dark blue lines correspond to $\langle w = 8 \rangle$ and $\langle w = 4 \rangle$ respectively. Each point is obtain from the average of ~ 15 experimental realization and the error bars are the standard deviation of the mean.

2.6 Tuning the Ring Geometry

The realization of the ring-trap and phase imprinting by the a light pattern created by a DMD gives us the possibility to tune some parameters of the system. In particular we can choose with an high degree of freedom the values of the inner and the outer radii of the ring, and consequently its width. In this section, I present the geometry effects on the stability of persistent currents. In particular I show how different parameters affect the maximum winding number excitable in the ring in the BEC-BCS crossover. In the last part I show how it is possible to excite persistent current in a thin-ring configuration, that could be important in future investigations, in particular for the study of physics in low dimensions.

2.6.1 Maximum winding number for different geometries

In the previous section it is shown that we can excite persistent currents in the ring up to $w = 8$ for the UFG and BEC regimes, $w = 6$ for the BCS regime. However, it is also possible to imprint higher circulation states, but in this case the flow is not persistent and a decay in a timescale of ten of ms is observed. Fig. 2.12 shows the average winding number evolution in time for different initial circulation states w_0 in the BEC regime. While states with circulation $w \leq 8$ are observed to survive up to a timescale comparable to the sample lifetime, for larger w_0 the circulation decays to the maximum persistent value. Data are obtained from the average of ~ 15 experimental realizations, error bars are the standerd deviation of the mean. The light blue curve in this figure shows the evolution in the $w_0 = 10$ case. A sigmoidal fit is performed and a decay constant $\tau_{decay} \simeq 40\,\text{ms}$ is obtain.

This results are relative to the geometry explored in the previous section, consisting in a inner radius of $R_{in} \simeq 10\,\mu\text{m}$ and an external radius of $R_{out} \simeq 20\,\mu\text{m}$, the width of the ring is therefore $\Delta R \simeq 10\,\mu\text{m}$. In order to understand how the geometrical parameters can affect the stability of the

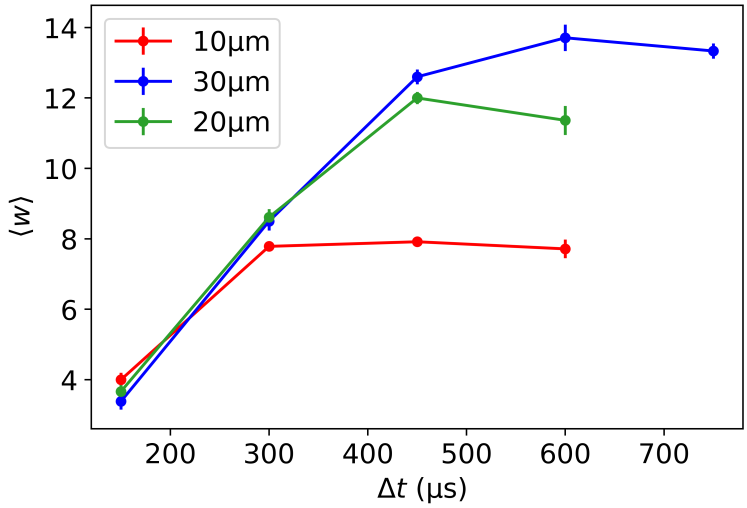

Figure 2.13: Measured average circulation 500 ms after the imprinting versus the imprinting time Δt. The results are relative to a pattern with 4 gradients. Different colours correspond to different inner radius of the ring R_{in}. For each geometries a saturation of w is observed.

currents in the ring, and in particular the maximum persistent circulation in the system, we study the persistence of the currents in different configurations. This study is important for future experiment, setting persistent currents properties in different geometrical configurations. In order to determine the maximum persistent circulation in a given geometry, we measure the winding number of the system 500 ms after the phase imprinting procedure in the BEC regime. We perform the same experimental procedure describe in the previous section. During the evolution time, states with winding number above the maximum persistent circulation are expected to decay. Considering the typical timescale pointed out by the analysis in Fig. 2.12, we detect the final winding number by the observation of the interference pattern 500 ms after the phase imprinting procedure.

The results show that the maximum persistent circulation do not depends on the outer radius of the system and only weakly on its width. On the other hand it strongly depends on the inner radius is. Fig. 2.13 shows the number of circulation in the system for different imprinting time Δt in the BEC regime, the phase imprinting protocol is performed using a four-gradient intensity pattern. Different colours correspond to different inner radius of the system. For each dimension of the inner disk, the measured winding number saturates for large values of the imprinting time. This is caused both by technical limitation of the phase imprinting (for long Δt the condition of small imprinting time is not satisfied) and, principally, for the decay of higher imprinted circulation. In fact during the evolution time circulation above the maximum persistent currents decays and we observe always the same final w state.

From Fig. 2.13 it is evident that bigger inner radii allows the creation of persistent currents with larger circulation in the system. This effect can be understood considering the velocity dependence on the radial coordinate r. The presence of a maximum winding number is related to the critical velocity of the system, whatever is the excitation causing the velocity dissipation. Higher circulation states correspond to higher velocities of the atoms flowing in the ring. Due to the velocity scaling as $1/r$, for a given circulation, the velocity field has a maximum of the modulus in correspondence of the inner edge of the ring. Therefore critical velocity of the system must be compared with the velocity field nearby the inner ring. Increasing the inner radius R_{in}, a given circulation w corresponds to a lower velocity and thus the critical velocity is reached for larger circulation w states. With this measure we

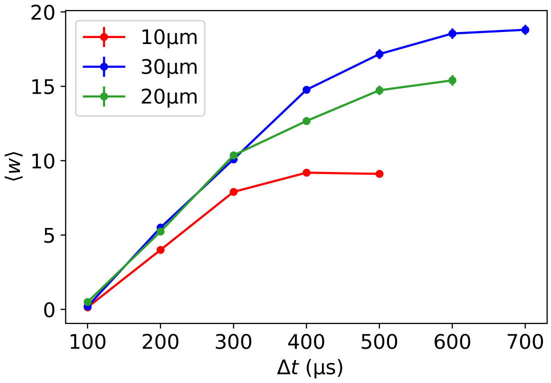

(a) Circulation after 500 ms versus imprinting time for different inner radius in the UFG regime

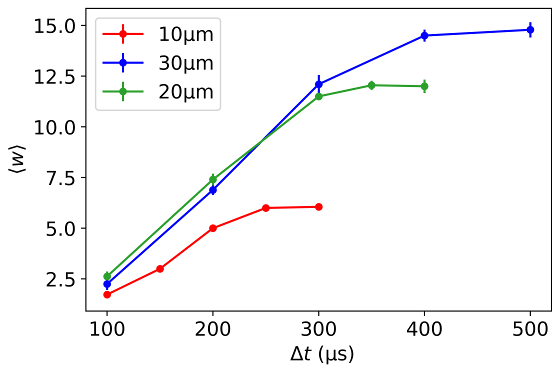

(b) Circulation after 300 ms versus imprinting time for different inner radius in the BCS regime

Figure 2.14: Observed circulation versus the imprinting time Δt in the UFG (a) and BCS (b) regimes, 500 ms and 300 ms after the imprinting respectively. The results are relative to a pattern with 4 gradients. Different colours correspond to different inner radii R_{in}. Also in these regimes we observe a saturation of w, and an increasing of the maximum persistent circulation as the radius of the system is increased.

underlined the possibility to excite persistent currents in the system with winding number $w > 8$ by increasing the inner radius of the system.

2.6.2 Geometry effect over the BEC-BCS crossover

The previous results are relative to the BEC case. However, excitation of circulation state above the maximum persistent one are possible and they are observed to decay in a similar way to the BEC case shown in Fig. 2.12. The possibility to observe this high circulation states suggests that the sweep of the magnetic field implemented in order to obtain a visible interference pattern do not affects the maximum persistent circulation in the BCS and in the UFG. In particular, for the UFG case, it is possible to argue that, since the maximum observed persistent circulation $w = 8$ in the same of the BEC regime, it is possible that during the sweeping of the magnetic field an higher circulation in the UFG regime is mapped in a $w = 8$ in the BEC. However, the experimental observation of $w > 8$ state in the UFG performing the same sweep of the magnetic field implies that this is not the case. Also in UFG and BCS regimes, we measure the circulation for different imprinting time after a long holding time for a four-gradient imprinting pattern changing the radius of the system. The results are shown Fig. 2.14. Also in this case we observe a saturation behaviour and an increasing maximum persistent circulation as the inner radius becomes bigger.

2.6.3 Persistent current in a thin ring

As we already mentioned, the maximum persistent circulation state depends mainly on the inner radius of the system. However an effect is observed also changing the width of the system. In particular the maximum persistent w remains constant until the ring is squeezed to sufficiently low width. In this last part of the chapter I will show that is possible to excite persistent current even in a thin superfluid ring by phase imprinting.

Fig. 2.15a shows the thinnest ring we are able to produce with the DMD pattern. In this configuration the system is not homogeneous in the redial direction, but rather can be described by a Gaussian with a full width at half maximum of 2.7 μm. Performing the same sample preparation and imprinting protocol as in the larger ring case, we observe that is possible to create circulation state

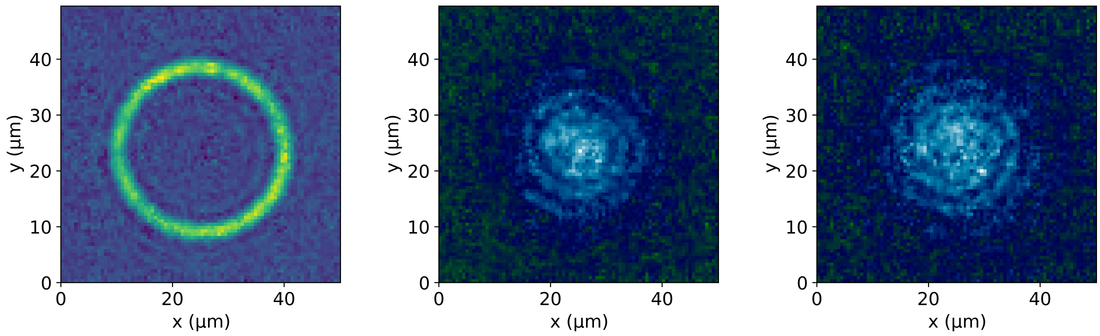

(a) Image of the thinnest ring we can realize from the DMD pattern

(b) $w = 1$

(c) $w = 2$

Figure 2.15: (a) In situ images of the thinnest ring we are able to create with the DMD pattern. In the radial direction the system is described by a Gaussian with FWHM = 2.7 ms. This value is on the order of the typical size of the pairs in the strongly interacting regime. (b)-(c) Interference pattern obtain by circulation states with $w = 1$ and $w = 2$ for this geometry.

with $w = 1$ and $w = 2$ even in this extreme geometry. Moreover this circulation are observed to be persistent in time. Fig. 2.15b-c show the interference pattern obtained for this two circulation states in this geometry.

The typical size ξ_0 of the pairs in the strongly interacting regime is on the order of the width in this geometry. In particular $\epsilon_0 \sim 1/k_F \simeq 0.3\,\mu$m in the unitary regime. In the BCS regime $\xi_0 \sim 1/k_F e^{-\pi/2k_F a_s} \simeq 0.6\,\mu$m for $k_F a_s = -0.4$.

In this case, the system is in a quasi bidimensional configuration (note that the dimension of the z direction is still present). The observation of persistent current in such geometry is important for future investigation on one dimensional out-of-equilibrium dynamics [57, 58]

Chapter 3

Supercurrents instability against an obstacle

In the previous chapter we described the protocol used in our system to create on demand circulation states. Observing the persistence of the currents through the ring, we also observe the superfluidity of the system across the BEC-BCS crossover. However, as we point out in the first chapter, superfluidity in a system can occur for velocity of the fluid below the critical velocity v_c, that depends on the excitation spectrum of the system. In particular, it is not obvious that the dissipative mechanism reducing the flow of the system for $v > v_c$ is the same for different type of superfluidity: as we saw in the first chapter, without considering vortices formation, in the BEC-BCS crossover the maximum superfluid velocity is limited by sound wave excitations in the BEC side and breaking of Cooper pairs in the BCS regime. The investigation of the type of excitation limiting the flow is particular interesting. In order to understand the decay process, we test the persistence in the case in which an obstacle in inserted in the ring. Decay of persistent currents has been already observed in bosonic superfluids in a ring trap. With our system we are able to study the decay mechanism in different type of condensed system. Despite the universality of the superfluidity in the three regimes, differences can emerge in the decay process, from the value for the critical velocity to the dissipative excitations.

In this chapter I present the results obtained from the study of the supercurrent behaviour across the BEC-BCS crossover in the presence of the obstacle. In the first section, I will describe the experimental protocol used for this experiment, and I will present the effect of the obstacle on the time evolution of the circulation w in the BEC-BCS crossover. In the second section I will focus on the observed excitations causing the dissipation in the system. In the last section, I will discuss further consideration about the decay mechanism.

3.1 Current dynamics in the presence of an obstacle

To probe the stability of the currents in the presence of an obstacle, the experimental protocol is slightly enriched respect to the one described in the previous chapter, in order to use the DMD also for the realization of the obstacle. In particular, we perform the same protocol described in section 2.3 (see Fig. 2.5), using a stopping barrier to prevent a flow from the loading from the cigar and obtain a configuration with a ring and an inner disk as is shown in Fig. 2.5e. Starting from this configuration we excite circulation state on the system using the phase imprinting method to obtain the desired w in the system. At this point we adiabatically ramp up an obstacle with a series of 26 DMD images, separated by 0.5 ms in time, for a total duration of the ramp of 13 ms. By considering that the light from the DMD create a repulsive potential, the obstacle is obtained by illuminating a

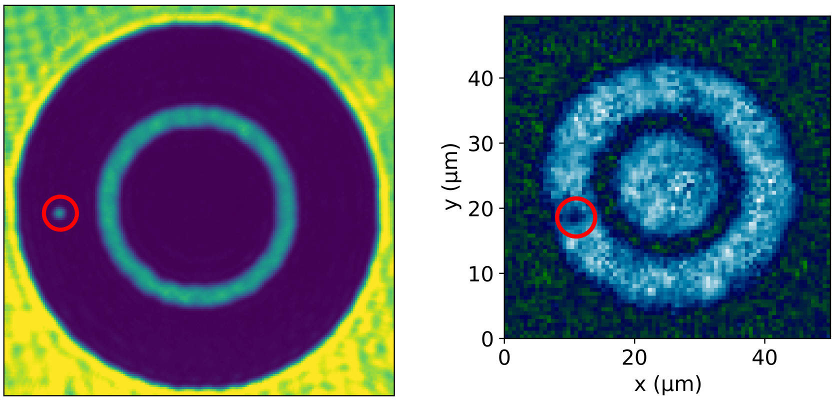

(a) (b)

Figure 3.1: (a) Typical light pattern created with the DMD in order to add an obstacle to the system. Considering the repulsive potential created by this light, the obstacle is realize by illuminating a small region in the ring. (b) Insitu images of the atomic sample with the obstacle on. The image is taken in the BEC regime. This figure is obtain from a single absorption imaging.

small region in the ring; in particular the obstacle is placed in the medium radial position between the inner and the external radii. At this point we let the system evolve, with the obstacle on. The holding time considered in the following is counted starting from the last image of the ramp, namely when the obstacle is completely ramped up. When measurements are performed on the BEC regime, after the chosen holding time, we directly perform a TOF images in order to detect the circulation from the spiral interference pattern obtained from the overlapping between the external ring and the inner disk. However, as we pointed out in the previous chapter, the same protocol is not applicable directly in the UFG and BCS regimes, because no interference pattern is visible in this cases. Moreover, also the sweep of the magnetic field in 50 ms performed in the study of the persistent currents is not directly applicable. In fact, the presence of the obstacle during the slow magnetic field sweep can affect the experimental results. In particular if the system with a circulation w in the BCS or UFG regimes do not present dissipation even in the presence of the obstacle, it can occur that during the changing of the magnetic field, a circulation decrease occurs, if the same w is not stable in the BEC regime when the obstacle in on. This effect is amplified considering the fact that the absolute height of the obstacle in the UFG and BCS regime is bigger respect to the BEC case. To solve this problem an additional step is implement in the DMD routine: after the desired holding time, we remove the obstacle from the system by adiabatically ramping it down. Also in this case, a series of 26 images, one every 0.5 ms, is used. At the end of this process the obstacle is not present and the current in the system is persistent[1]. At this point the sweep of the magnetic field to the BEC side is performed and the circulation is obtain from the interference pattern. Considering that the maximum persistent circulation takes the minimum value, $w = 6$ in the BCS regime and it is the same in the UFG and BEC (w=8), there is no possibility that the sweep affects the results of the measure. The waiting time between the end of the ramp used to remove the obstacle and the beginning of the magnetic field sweep is not relevant, because in this configuration the currents are persistent. This time is set to 30 ms.

Fig. 3.1a shows the pattern shone by the DMD on the atomic sample during the holding time when the obstacle is on. This images is observed by comparing imaging the DMD display on a 'service'

[1]This is true considering an initial circulation w_0 below or equal to the maximum persistent circulation observed in the previous chapter. In fact, if decay occurs during the holding time with the obstacle on, the final circulation after the obstacle is removed can be only below the initial one, and therefore persistent.

	B	$1/k_F a_s$	$\mu/\hbar$	V_0/μ	V_0/E_F
BEC	702 G	3.6	1.0 kHz	0.8	0.1
UFG	834 G	0.0	8.9 kHz	0.4	0.2
BCS	862 G	−0.4	10.0 kHz	0.26	0.2

Table 3.1: Intensity of the obstacle respect the chemical potential and the Fermi energy for the three cases of $1/k_F a_s$ studied.

camera in the projection setup [42]. Thanks to the high resolution of the system, we are able to create a circular obstacle with dimensions comparable with the characteristic length of the superfluid by the use of the DMD. This is important when we want to compare the observed critical velocity with the Landau criterium prediction: in particular it is predicted the the measured critical velocity approaches the Landau critical velocity in the case of vanishing perturbation in the system [59]. The light pattern creating the obstacle has a Gaussian shape, with an approximately round profile of full width at half maximum (FWHM) of 1.6 μm. This dimension must be compared to the healing length ξ of the system, namely the typical length scale in which the density of the system relaxes to the perturbation given from an external potential. The healing length consists also in the minimum length scale for the change in the phase and density of the system. For a BEC superfluid, $\xi = 1/\sqrt{8\pi n a_s}$. At the unitarity, $\xi \sim 1/k_F$, and increase moving towards the BCS regime following $\xi \sim 1/k_F e^{-\pi/2k_F a_s}$. Typical healing length in the three regimes are on the order of $0.1 - 1\,\mu$m. Therefore the external perturbation inserted in the ring is comparable to this scale. The intensity of the obstacle is chosen in order to be comparable to the chemical potential of the system in BEC superfluid and increased while moving to the strongly interacting regime to observe the instability despite the higher chemical potential. In fact this quantity depends on $k_F a_s$. In particular μ increases as we move to bigger magnetic field. In particular the chemical potential in the three regimes is 1.0, 8.9 and 10.0 kHz in terms of $\hbar$, respectively in the BEC, UFG and BCS regime. Therefore the intensity is increased in the experiment passing from the BEC to the BCS. Table 3.1 are showed the values of the chemical potential, and the peak intensity of the obstacle V_0 respect to the chemical potential and to the Fermi energy.

In order to calibrate V_0 we realize the following procedure in the BEC regime. By imaging, we measure the atom number in a small region around an obstacle shone by the DMD light for different values of the intensity. As this intensity is increased, the atom number is expected to decrease. However the curve af the atom number versus the intensity of the light is expected to shows a kick for $V_0 = \mu$. In this way is possible to calibrate the intensity of the obstacle in term of μ [60]. However the calibration obtained from this protocol is not particularly precise, due to the small size of the obstacle.

3.1.1 Current decay

In the previous part of this section it is presented the experimental protocol implemented to study how the system, excited in a persistent circulation state, evolve in the presence of an obstacle across the ring. The first effect observed is that, in some cases, the circulation state decays and then stabilizes to a lower value of w; therefore a dissipation occurs. In particular we track the value of the circulation for different holding time t for which the obstacle is kept on the system; in the following a detailed discussion of our observation in the three superfluid regimes investigated is observed. In the last part of this section the results for all the three regimes are discussed.

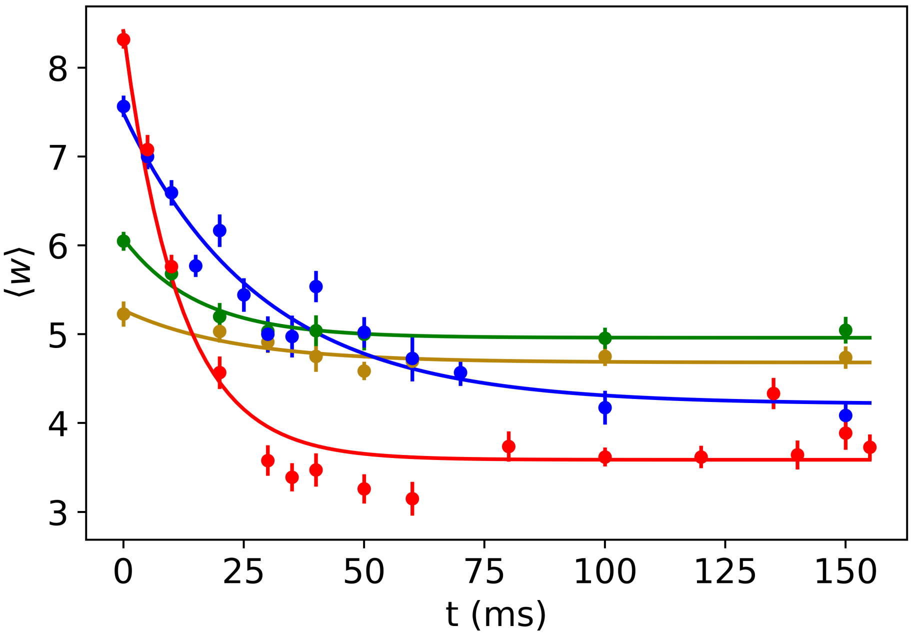

Figure 3.2: Time evolution of the circulation in the BEC regime for different initial circulation w_0. An exponential decay of the circulation is observed for $w_0 > 5$. The blue plot corresponds to an initial circulation slightly above 5 and a small decay is observed in this case too.

BEC regime

In the BEC regime we test the persistence of the currents by adding an obstacle of intensity $V_0/\mu = 0.8$. Considering the maximum persistent circulation of $w_{max} = 8$ in this regime, we investigate the current stability for circulation states with $w_0 \leq 8$.

Fig. 3.2 shows the results relative to the BEC regime. We check the circulation states of the system versus the holding time with the obstacle acting on the system for different initial circulation. For low circulation states no dissipation is observed, and therefore they are not reported in the plot, while for higher w_0 the winding number is observed to decrease in time. In particular, the system is stable despite the presence of the obstacle up to initial circulation states of $w_0 = 5$, while for $w_0 > 5$ an exponential decay is observed. Each point is obtained from the average of the circulation of at least 20 repetition, error bars are the standard deviation of the mean. For $w_0 \geq 6$ an exponential fit is performed:

$$\langle w \rangle(t) = \langle w_0 \rangle e^{-\frac{t}{\tau}} + \langle w_f \rangle. \tag{3.1}$$

Therefore from these results two quantities are obtained: the decay time τ, namely the typical timescale in which the system decays to lower circulation states, and the final circulation $\langle w_f \rangle$. In fact, after a first decay, the circulation of the system stabilizes to a final value that shows to be persistent despite the presence of the obstacle. It is important to notice that this final value is not the same for all the initial circulation state. Typical timescales of the decay are on the order of $\tau \sim 10\,\text{ms}$.

UFG regime

To point out the behaviour of persistent currents in the crossover we perform the same measurement in the unitary and BCS regimes, considering an obstacle intensity $V_0/E_F = 0.2$ in order to induce the

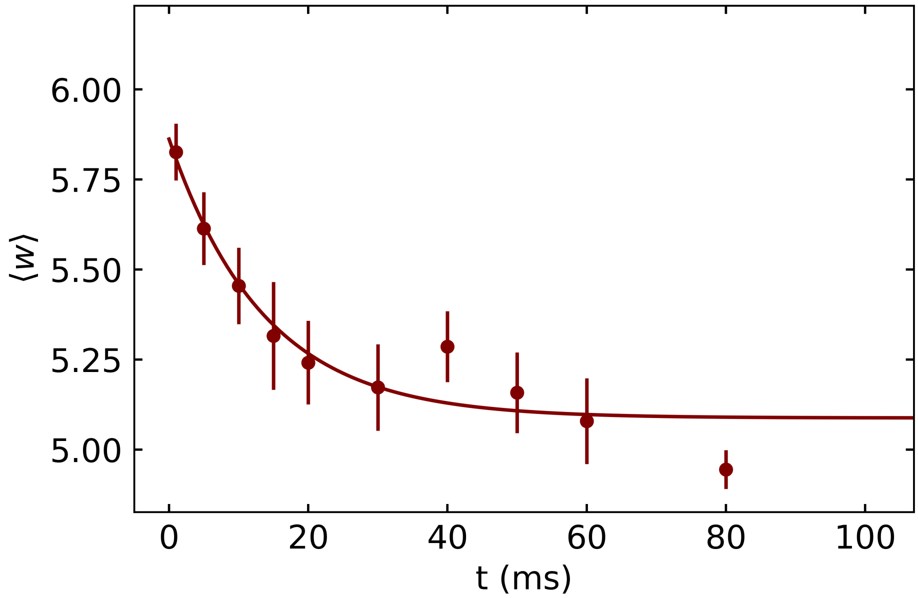

Figure 3.3: Time evolution of the circulation in the BCS regime for an initial circulation state $w_0 > 5$ in presence of an obstacle of height $V_0/\mu = 0.2$.

circulation to decay and to observe the excitations responsable of the velocity dissipation. In fact this regimes are expected to be more robust respect to the BEC, because of their highr chemical potential. the results obtained for the unitary regime show that no decay occurs in this case for any circulation. For all the value of the initial circulation $w_0 \leq 8$, w is contant in time and no dissipation is observed.

BCS regime

Finally we perform the measurement in the BCS regime. In this case the obstacle height assuring a $V_0/E_F = 0.2$ correspond to $V_=/\mu = 0.26$. The investigation of the effect of the obstacle on the circulation state is limited for the maximum persistent circulation at state with $w_0 \leq 6$. Fig. 3.3 shows the time evolution of the circulation in this regime. Dissipation is observed to happen only for $w_0 = 6$.

General results

The general results of the persistent current decay in the BEC-BCS crossover are shown in 3.4. In particular here it is plotted the value of the final winding number, $\langle w_f \rangle$, versus the average initial circulation state of the system $\langle w_0 \rangle$. By comparing the results for different regimes we observe that the UFG superfluid is the most stable one. In this case no dissipation is observed and we are not able to estimate the critical circulation in the presence of the obstacle.

On the other hand, we observe a dissipation effect in both BEC and BCS regimes. The critical circulation is $w_c = 5$ in both the case. In Table 3.2 are resumed the corresponding velocities at the inner radius and they are compared to the calculated speed of sound. Despite the same critical circulation, due to the different speed of sound c_s, the BCS has a lower critical velocity respect to the sound velocity. In the next section we will explore the dissipative mechanism that induce the circulation decay.

Fig. 3.4 shows final circulation state $\langle w_f \rangle$ versus $\langle w_0 \rangle$ for the three regimes studied. The grey line corresponds to a $\langle w_f \rangle = \langle w_0 \rangle$. Therefore, when a point is on this line, it indicates that no decay occurs. Currents with $w_0 \geq 6$ in the BCS and BEC regime are far apart from this line, signature that they undergo to dissipation. Moreover it is important to underline that the final circulation for $w_0 > 5$ in the BEC regime is not constant. In particular, it decreases for larger value of $\langle w_0 \rangle$. This can appears counterintuitive. In fact, one can argue that the final circulation of the system must be the one with a velocity next to the inner radius equal to the critical velocity. As a consequence the same $\langle w_f \rangle$ is expected for $\langle w_0 \rangle > 5$, in contrast with our results. An interpretation of the observed decreasing $\langle w_f \rangle$ is given by numerical simulation , as we will see in the following section.

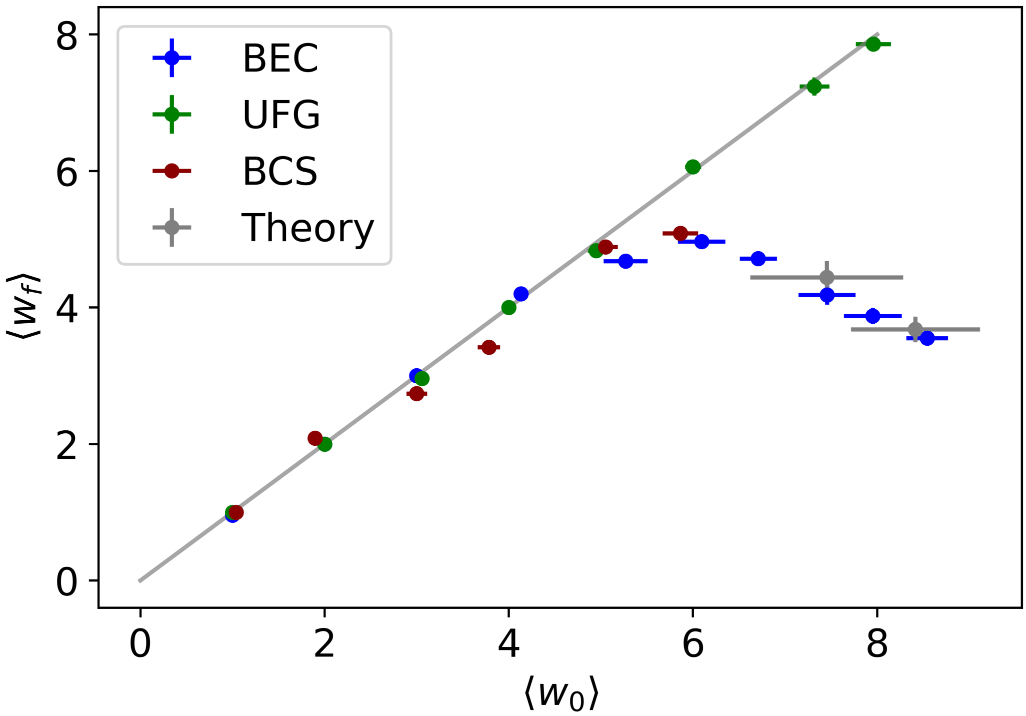

Figure 3.4: Final circulation state w_f versus w_0 for the three regime studied when the obstacle acts on the system. The line indicate the $w_f = w_0$ case. The grey circles are results obtained from numerical simulation, that are introduced in the following section.

	B	$1/k_F a$	w_c	v_c	c_s	v_c/c_s
BEC	702 G	5.53	5	2.3 mm/s	5.4 mm/s	0.46
BCS	862 G	−0.42	5	2.3 mm/s	14.4 mm/s	0.18
UFG	834 G	0.0	> 8	> 3.7 mm/s	14.1 mm/s	> 0.26

Table 3.2: Critical velocity in the presence of an obstacle for the different regimes. w_c is the critical observed circulation in the system, and v_c the corresponding velocity in proximity of the inner ring. c_s is the speed of sound.

From the confront between the UFG and BCS regimes, we observe an interesting behaviour. Despite that in the BCS the obstacle height is lower with respect to the chemical potential, a dissipation is observe for lower value of $\langle w_0 \rangle$. This effect demonstrate the presence of dissipative effects linked to the fermionic nature of the system, like pair breaking mechanism.

3.2 Vortices nucleation from supercurrent decay

The presence of dissipation in two different regime gives us the possibility to study the type of excitations that make the circulation unstable, namely the excitation related to the critical velocity of Eq. 1.25 in different type of superfluidity. As it is shown in the first chapter, under certain condition, the excitation limiting the maximum superfluid velocity are sound waves in the BEC case, while pair braking in the BCS. Therefore different excitations can be dominant in different regimes. However in our case the decay process is induced by emission of quantized vortices in both the cases. The process in which a flow in a channel is dissipated by vortices emission in know as phase-sip.

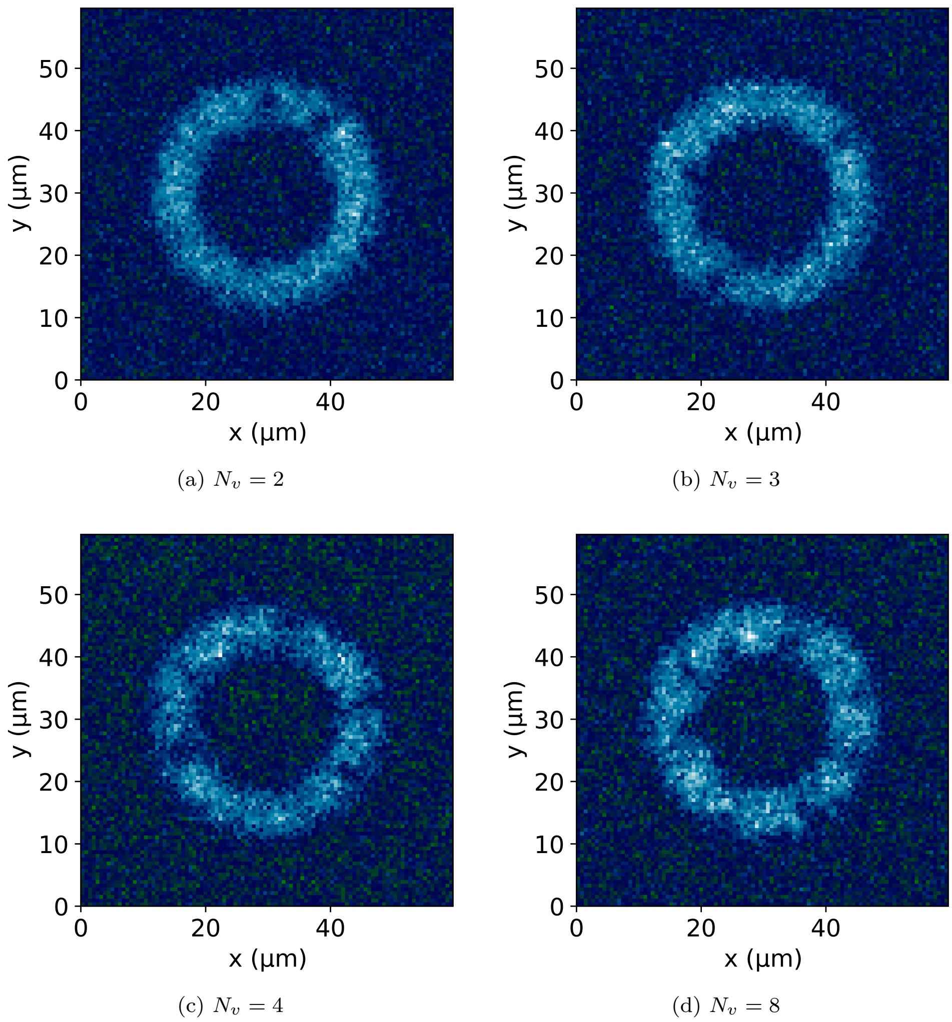

Figure 3.5: Images of vortices observed in the ring as a consequence of the circulation decay. The imaging protocol is described in the main. Vortices appear like holes in the density profile. The images are relative to the measure in the BEC regime with an initial circulation of $\langle w_0 \rangle = 7$ and 8. Subcaptions indicate the number of vortices in the image.

3.2.1 Vortices detection

In order to detect vortices created as a consequence of the circulation decay, we prepare the sample without the inner disk. keeping only the external ring. In this way during the expansion, no interference pattern is formed and this make the vortices more visible. Starting from the sample in the configuration in Fig. 2.5a, we load the atoms in in a ring, without putting the inner disk. Then the stopping barrier is removed and we use the phase imprinting protocol to excite the desired circulation state; doing this, we use the same Δt for the excitation of the same circulation in the case with the inner disk, in which we can estimate the value of w.

In order to reproduce the procedure described in the previous section for the study of the circulation decay, we adiabatically ramp up the obstacle in 13 ms and then we wait a variable holding time t. In contrast with the protocol described in the previous section, we ramp down the obstacle in all the regimes. In fact its presence can be confused as a vortex due to the density depletion induced and it can affect the vortex dynamic during the TOF. In order to detect the presence of vortices we perform an imaging of the superfluid density after a TOF; vortices appear in the sample as holes in the density. However, the detection of vortices from a simple TOF expansion is complicated, as during the TOF the atomic density gets substantially reduced, reducing the contrast of vortices. To maximize the vortices visibility we perform a more complicated trap release: in particular we abruptly switch off the $\mathrm{TEM}_{0,1}$, used for provide the vertical confinement on the sample, and, starting at the same time, we turn off the $x - y$ optical potential created by the DMD light pattern with a linear ramp 1 ms long. We then let the gas expand in the free space for other 0.5 ms before imaging the density. In this way we are able to detect vortices with higher contrast.

However, as it is shown in Fig. 2.10, vortices are created also during the imprinting. In order to be sure that they are no present in the sample during the current decay, we wait 300 ms before performing the measure. To be sure that this does not affect the results, we verified that the time evolution of the circulation in the system does not change whether we ramp up the obstacle 300 ms or 30 ms after the imprinting procedure.

This process is directly applied in the weakly interacting BEC regime. In this case the condensed fraction of the system is about 85 % and the hole in the density corresponding to the presence of a vortex is clearly visible. As in the case of the interference pattern, in the BCS regime, the visibility of the vortices is reduced. The mainly reason is that in this case, quasiparticle excitation, namely unbounded particle, occupy the empty region in the vortex core. Therefore, we are not able to detect vortices directly in the BCS regime. Moreover, the procedure applied in the study of the circulation decay is not applicable in this case. In fact, in that case, we perform an adiabatic sweep of the magnetic field, relying on the persistence of the currents we want to observe. On the contrary, vortices dynamics happens in a faster timescale: they tend to exit from the ring in tens of ms and their number is not constant. Therefore, to detect vortices in the BCS regime, we perform a rapid sweep of the magnetic field in the BEC regime [61]. In particular, after the ramping down of the obstacle is completed, we linearly sweep the magnetic field to 702 G in around 5.5 ms. During the last 1.5 ms of this ramp, the same TOF imaging protocol for the vortices detection in the BEC is used.

3.2.2 Vortices emission

Fig. 3.6 shows the results about the number of vortices observed in the ring at different holding time t in the BEC regime. In order to quantify the vortices emission we track their average number $\langle N_v \rangle$ as a function of the holding time of the obstacle t. The number of observed vortices in the ring quickly increases in the first $5 - 10$ ms and reach a saturation value. This suggests that the obstacle acting on the superfluid excites vortex nucleation, but that after few milliseconds this formation is stopped. Furthermore, after ~ 50 ms, N_v starts to decrease, suggesting that vortices, after a certain time inside the superfluid, go away from the ring. The measurements are performed for value of initial circulation w_0 for which decay of circulation in presence of the obstacle is observed, with the same circulation of Fig. 3.2. Each point is obtained by averaging the number of observed vortices of twenty repetitions, error bars correspond to the standard deviation of the mean. In order to extract quantitative information a fit is performed with the function:

$$\langle N_v(t)\rangle = \begin{cases} N_e(1-e^{\frac{t}{\tau_1}}) + N_s & \text{for } t < t_0 \\ (N_e + N_s)(e^{\frac{t-t_0}{\tau_2}}) & \text{for } t \geq t_0 \end{cases}$$

The first part of this formula ($t < t_0$) describes the exponential increase of the number of vortices observed for low value of the holding time t. From the fit we can evaluate the value of N_e and τ_1. The first represent the value to which the number of vortices tend to saturate; we can interpret this as the value of the total vortex emitted in the decay process. τ_1 simply represent the typical timescale of the process. N_s is the number of spurious vortices producted in the imprinting procedure, that are still present also after 300 ms after the imprinting procedure. In all cases $N_s < 1$

In order to understand the dissipative mechanism responsable of the circulation decay in the BCS regime, we detect the presence of vortices also in this case. The results are shown in Fig. 3.7. We realize the measure only for the $w_0 \sim 6$ case, the only one where we observe the current decay. The results show a similar trend to the one observed in the BEC case, consisting in an increase of the number of vortices in the ring and a subsequent decay. This observation demonstrates that the flow of a fermionic superfluid in a ring moving against the presence of an obstacle can be decrease by the formation of vortices also in the BCS regime.

Dissipative process via emission of vortices have been already observe in superfluid Helium [62, 63] and in simply-connected condensed gases [64], as well as in toroidal Bose-Einstein condensates [11]. Phase-slip as a possible process of dissipation in toroidal Bose-Einstein condensed has been studied in theoretical work [65]. In this type of process, vortices and antivortices enter in the sample reducing the velocity of the system and provoking the phase jump necessary to reduce the circulation. The Feynman's approach to the critical velocity (Eq. 1.30) takes into account this phenomena, and in some cases it reveals a good way to estimate the critical velocity [12], although this formula set only the order of magnitude for v_c [11]. However, this formula is obtained by simple energetic considerations. Vortex nucleation in the system must instead be driven by dynamical excitation on the surface of the system. As a consequence the critical velocity can increase with respect to the Feynman approach, in order to consider the energetic threshold given by the formation of the surface mode [66]. An estimation for this critical velocity in non-homogeneous gases in harmonic trap is derived in [67]and an application to toroidal Bose-Einstein condensate is obtained in [68], where the expression for the critical velocity is the same, but, due to the $1/r$ decay of the velocity field, the critical velocity will be reached in the inner part of the system for lower circulation states. Therefore despite phase slip can occur both with antivortices entering in the system from the external radius or vortices the inner, this last process limits the critical velocity to lower value.

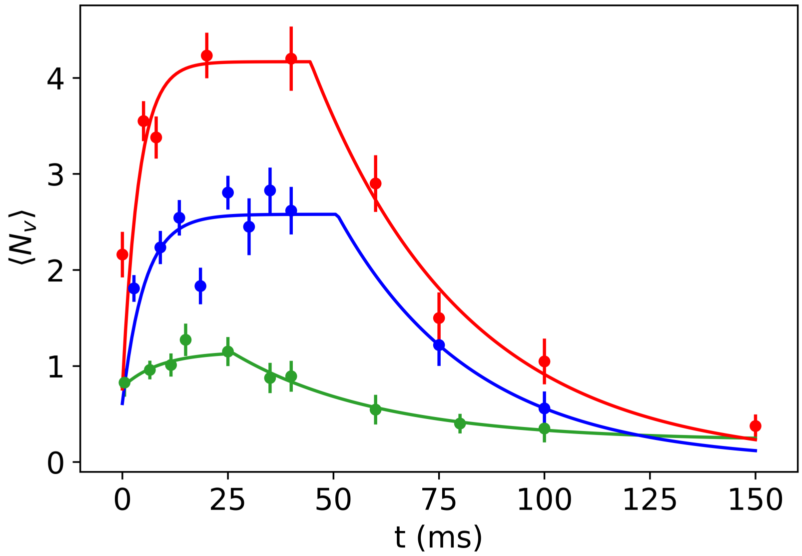

Figure 3.6: Number of vortices N_v in the sample as a function of the holding time t in which the obstacle is on in the BEC regime. The data are relative to the measure for which a decay is observed. After a fast increase, of the vortices number stabilize to a maximum value. Successively, a decay process is observed. The lines represent fits of the data.

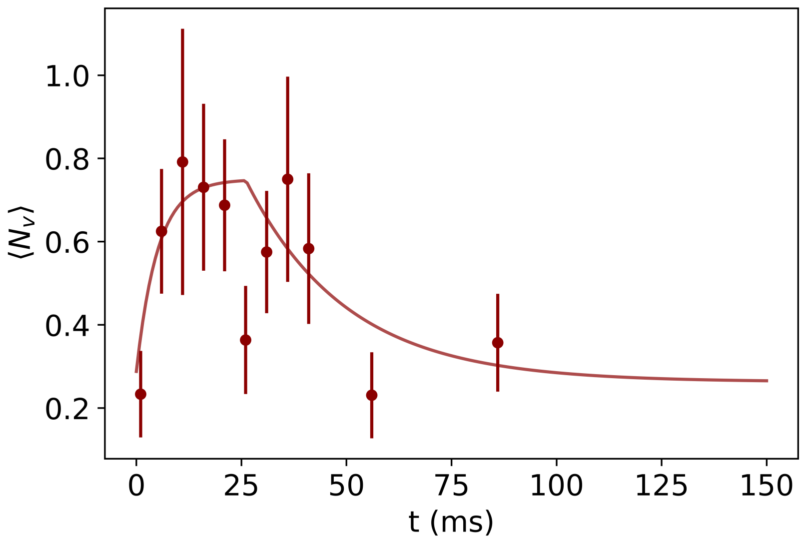

Figure 3.7: Number of vortices N_v in the sample versus the holding time t in which the obstacle is on in the BCS regime for an initial circulation $w_0 = 6$. As in the BEC case, the plot shows a fast increase of the number of vortices followed by an exponential decay

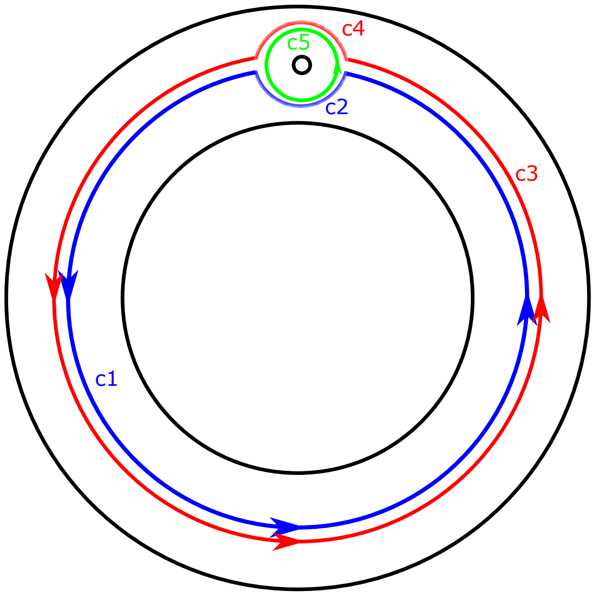

Figure 3.8: Circulation in the ring in the presence of a vortex. Calculating the circulation over the blue path, in the inner part of the ring respect to the vortex position, we circulation reduced by one respect to the one calculated over the red line. This can explain how the generation of vortices can reduce the circulation of the system

3.3 Dissipative mechanism

To understand how the generation of vortices can reduce the circulation of the system we consider the situation showed in Fig. 3.8. In this plot, the superfluid is trapped inside a ring, as in our case and a vortex of charge $l = 1$, represented by the black circle in the upper part of the ring, is present inside the system. Let' consider the circulation of the velocity in two side of the superfluid: one in the inner part of the ring respect to the vortex position (the blue curve in the plot c1+c2), the other in the outer part of the sample (the red curve c3+c4). Considering w and l positive for anticlockwise flow, the circulation of the velocity field calculated for the green curve c5 around the vortex itself is:

$$\Gamma_{\mathrm{c5}} = \oint_{\mathrm{c5}} \mathbf{v} d\mathbf{s} = \frac{h}{2m} \tag{3.2}$$

corresponding to the circulation of a vortex with charge one. Similarly, we can also calculate the difference between the two circulation discussed above. In particular, considering the curve c1 and c3 as the same, this difference is

$$\Gamma_{\mathrm{c3+c4}} - \Gamma_{\mathrm{c1+c2}} = \Gamma_{\mathrm{c4}} - \Gamma_{\mathrm{c2}} = \oint_{\mathrm{c4}} \mathbf{v} d\mathbf{s} - \oint_{\mathrm{c2}} \mathbf{v} d\mathbf{s} \tag{3.3}$$

The combination of the last two integral is equivalent to the integral over the curve c5. Therefore we obtain that

$$\Gamma_{\mathrm{c3+c4}} = \Gamma_{\mathrm{c1+c2}} + \frac{h}{2m} \tag{3.4}$$

Therefore, if the circulation calculated in the inner part of the system it has a value corresponding to a winding number w_i, in the outer part of the ring we have a winding number $w_e = w_i + 1$. Note that this result is intuitively understandable considering that the velocity field has opposite directions, on

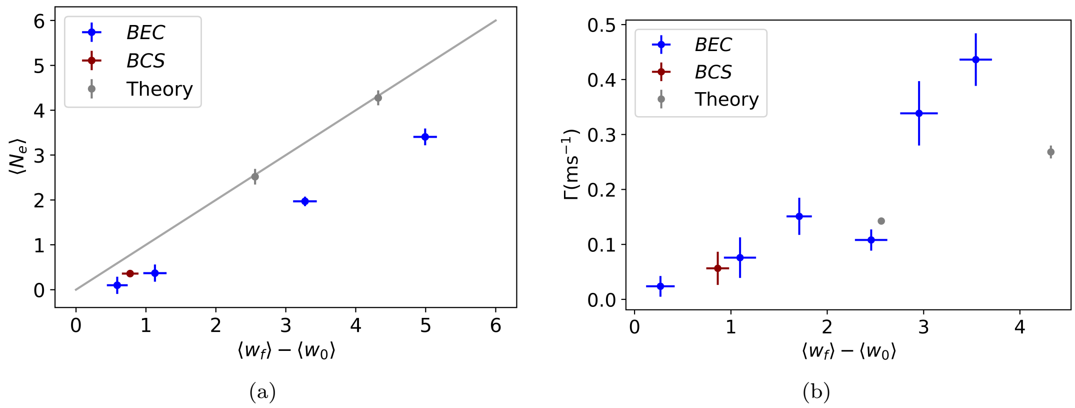

Figure 3.9: (a) Value of total emitted vortices N_e fas a function of the circulation reduction during the decay. The number of vortices is observed to be almost the same of the number of lost circulation. (b) Decay rate Γ of the circulation decay. The grey circles are results obtained from numerical simulation.

the opposite sides of the vortex. In the following I explain how this behaviour can be used in order to understand the lowering of circulation via vortices emission. We consider an initial situation of the superfluid in an unstable circulation state w_{in}. Due to the presence of an obstacle, the circulation decay and a vortex is emitted. We can consider that the vortex is formed from the inner surface of the system. When the vortex is not completely inside the ring, the circulation of the velocity is $w_{in}h/2m$ everywhere. However, as soon as the vortex enters in the superfluid we can apply the consideration of the circulation states just described. In particular the circulation calculated for a curve passing from the inner part of the vortex will give a winding number of $w = w_{in} - 1$, while for a curve passing from the outer part we obtain $w = w_{in}$. During its evolution the vortex exit from the ring through the outer surface. At this point every circulation is calculated in the inner part respect to the vortex and the system is in a state with winding number $w = w_{in} - 1$. In this way it is possible to understand how a vortex that enters in the ring from the inner surface, crosses all the ring and finally exits from the outer surface is actually able to reduce the circulation state of the system. The same effect is obtained in the case of an antivortex (with charge $l = -1$, namely a vortex with the same velocity field of the $l = 1$ case but flowing in the clockwise direction) coming from the external surface that exits from the inner surface after having crossed radially all the system. However, as we already mention, surface instability necessary for the creation of vortices from the inner radius occurs for lower circulation state, as the velocity in this region is higher.

Fig. 3.9a shows the number of total emitted vortices N_e obtained from the fit of data in Fig. 3.6 and 3.7 versus the number of lost circulation during the decay process for the same initial circulation state w_0. We observe that the total number of vortices is always lower than $w_0 - w_f$. However they are quiet similar. The results obtained corroborate the idea of the decay process described above. In particular each vortex emitted correspond to approximately the decrease of one circulation. Furthermore, the timescale τ relative to the decay of circulation is usually bigger respect to the corresponding timescale for the vortices nucleation τ_1. The slight discrepancy can be explain in different ways. First, we need to consider the experimental protocol used to detect vortices. In fact the 13 ms employed for ramping down the obstacle, are enough to perturb the vortex dynamics. Moreover the timescale needed to reach the saturation of the number of vortices is of the same order of the decay timescale τ_2 in which vortices can escape from the ring. Therefore it is possible that some vortex is already gone away from the system in the time necessary to reach the saturation, inducing a lower estimation of the total emitted vortices by N_e. Finally is not obvious that the system behaves in the same way with and without the inner disk and this could affect the number of emitted vortices, because of the differences in the boundary conditions on the inner ring radius. In Fig. 3.9b it is shown the obtained decay rate for the different initial circulation states versus the number of emitted vortices. An increase of this quantity in observed for larger number of emitted vortices and the timescale in the BEC and BCS regimes look consistent.

In order to understand more deeply the dissipative process and describe the microscopic mechanism of vortex emission, Gross-Pitaevskii simulation has been realized by Kljedja Xhani. In particular a system with the same geometry has been studied, using the experimental parameters. Also in this case a circulation state is created in the system by phase imprinting, employing the same imprinting potential of the experiment. To compare directly the data obtained from numerical simulation to the experimental ones, the same interferometric technique is realized in order to detect the circulation state.

The small dimension of the obstacle makes the calibration of V_0/μ not extremely precise. Therefore, numerical simulation are performed for different value of $V_0 \sim \mu$. To find the V_0 that best fits the experimental data.

In the simulation, the decay is observed to occur for initial circulation $w_0 \geq 6$, comparable with the critical value for the experimental BEC $w_c = 5$. In the case of $w_0 = 7$ and $w_0 = 8$, the circulation is observed to decay by the emission vortices from the inner part of the ring, proving our consideration about the decay mechanism process. It is important to notice that the simulations confirms that the number of emitted vortices is well described by $\langle N_e \rangle = \langle w_f - w_0 \rangle$. Furthermore, also in simulation it is observed that higher circulation states decay to lower $\langle w_f \rangle$. Probably this is caused by the presence of a bigger number of vortices in the system.

The numerical results provide a way to understand the mechanism leading to the formation of the vortices. For $w > w_c$ the density profile reveals the presence of low-density channel between the obstacle and the inner radius of the ring. In the same part of the system, the velocity is observe to increases. At the same time, the velocity field in this region is observed to overcome the local speed of sound[2]. When this happens, a vortex is formed in the low density channel from the inner part of the ring, and the phase slip occurs, reducing the circulation of the system. After the creation of the vortex the velocity in the region is reduced in line with the reduction of the gradient of the phase of the system related with the phase slip. However the velocity can increase again when the vortex is gone away from the region of the obstacle. In this case, if the velocity overcome again the speed of sound, a new vortex nucleation can occur. Also in the case of $w_0 = w_c$ an increase of the velocity and a decrease of the density is observed. However, in this case the resulting velocity is not high enough to exceed the local speed of sound and the phase slip process does not occur.

As we pointed out above, the vortex creation in the superfluid must be driven by the creation of surface mode on the inner or the outer part of the ring. In this case the presence of the obstacle create a region between itself and the inner ring of the obstacle where the velocity field exceeds the local speed of sound, allowing the creation of wave in the system and exciting the inner surface in proximity of the obstacle position.

[2]Note that the velocity field bigger than the critical velocity is obtain by two factors: first, the increase of the velocity induce by the obstacle in the low-density channel, second the reduction of the sound velocity due to the lowering of the density

Chapter 4

Currents instability in a two-ring geometry

The high degree of manipulation om the potential acting on the atomic sample offer by the DMD, allows to explore more complex geometries. A natural improvement, respect to the potential studied in the previous chapter, is the realization of a superfluid trapped in double concentric rings separated by a barrier in order to study dynamical instabilities of the currents in this configuration. In this chapter I will present the characterization of this geometry. In the first section, I will describe the potential used for this study and the protocol used for imprinting persistent current in the two rings. In the second section I will present what happen to the system when the barrier between the two ring is removed. This process allows the formation of a crystal of vortices in the separation surface. This state of the system represents the configuration in which a dynamical instability is observed. This study is realize in order to explore the dynamical instability of the vortices array, that cis related to the Kelvin-Helmholtz instabilities in classical fluids. In the last part of this chapter I will show some preliminary observation and results of this instability. All the results showed in this chapter are obtain in the BEC regime.

4.1 Double Ring Potential

To realize the double ring potential with the DMD we use the light pattern showed in Fig.4.1a. A bright circular region creates a barrier between the two superfluids rings, that will be confined in the two black regions, as the potential created with the DMD is repulsive. An inner bright disk provide a repulsive region with no atoms in the centre of the sample. The most internal radius is $R_{in} = 9.95\,\mu$m, while the most external one is $R_{out} = 44.77\,\mu$m. The barrier designed in order to be in the middle of these two radius. Fig. 4.1b shows the cut along the x direction in the centre of the intensity profile. As we can see the intensity of the circular barrier between the two rings is less intense respect to the inner and the outer confinement potentials. However, once projected onto the atomic cloud, the barrier height this is well above the chemical potential of the BEC, creating a region with zero density. Therefore this intensity is sufficiently high to separate the two condensed rings. The parameter of the DMD necessary to create this barrier has been chosen in order to be the minimum allowing the existence of persistent currents in the two rings independent from the other ring. In order to characterize the circular barrier, I start from the images in Fig. 4.2a, showing the same intensity profile of 4.1a. The system is analyzed in polar coordinates. In particular 4.1b shows the intensity profile in polar coordinates r and θ, where $r = 0$ correspond to the red point in the Fig. 4.1a. Then, selecting a radial region around the barrier, I perform a Gaussian fit of the intensity

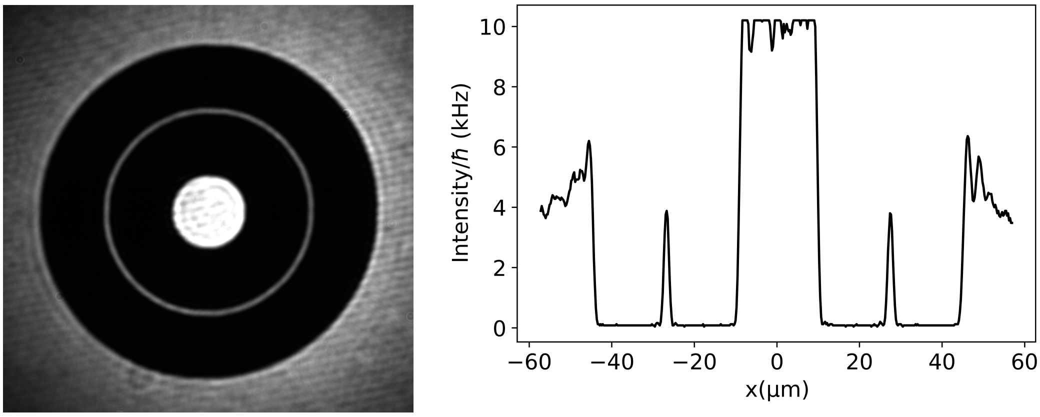

(a) (b)

Figure 4.1: (a) Light pattern created with the DMD for the realization of the double ring superfluid.(b) Linear cut of the potential along the centre along the x direction.

profile:

$$V_0 e^{-\frac{1}{2}(\frac{r-R_b}{\sigma})^2}. \tag{4.1}$$

The results for the fit for different angular position. The results show some fluctuations are shown in Fig. 4.2c.The barrier parameter show a dependance on θ. Therefore data obtained for different angular position are averaged. The resulting value for the circular barrier are:

$$\frac{V_0}{\hbar} = 3.8 \pm 0.3\,\text{kHz}, \tag{4.2}$$

$$\sigma = 1.15 \pm 0.05\,\mu\text{m}, \tag{4.3}$$

and

$$R_b = 27.4 \pm 0.2\,\mu\text{m}, \tag{4.4}$$

where the error is the standard deviation. R_b is the radial position of the centre of the circular barrier, which is confirmed to be approximately in the middle between R_{in} and R_{out}. The above results are relative to the potential used for study of superfluids in a double ring configuration in the BEC regime. In the UFG and BCS regimes, due to the larger chemical potential, the intensity is increased by a factor of 2 and 2.75 respectively.

The characterization of the double ring configuration is important in order to realize more complicated systems with the possibility of excite circulation states in both the rings independently. This configuration is the fundamental starting geometry for different possible experimental observation like the dynamical instability [69] analogous to the Kelvin-Helmholtz instability in classical fluid that is introduced in the last section of this chapter, or the study of the Josephson effect. On this line, in the next part of the section, I will describe the experimental protocol used the realization of a superfluid trapped in a double ring geometry and the excitation of persistent currents in this case.

4.1.1 Double-ring condensate preparation

The experimental protocol used for creation of the in the double ring geometry is similar to the one used for the single ring superfluid. However modify the experimental sequence to prepare the double ring. In particular, the first image that is shone on the atoms directly in the cigar trap load the sample in a homogeneous disk, as is shown in Fig. 4.3a. Respect to the preparation for the single

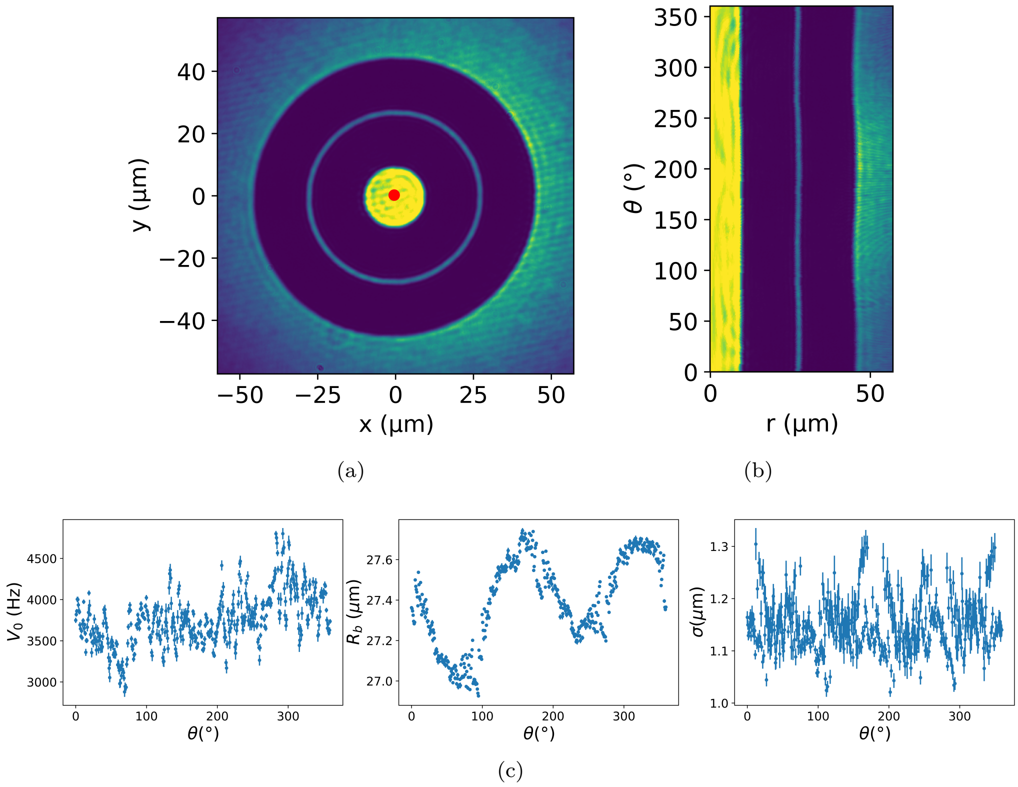

Figure 4.2: (a) Intensity pattern used for realize the double ring trap. the red spot indicates the centre of the profile. (b) Unwrapped intensity around the red spot in (a) used for the characterization of the circular barrier.(c) Results from the fit for different values of the angular coordinate θ. The fluctuation on the position are on the order of the resolution.($\sim 0.25\,\mu$m).

ring configuration, we do not employ the stopping barrier in order to stop the flow, and this result was obtained. In fact, in the double ring configuration However, in the double ring configuration we observe that the gas was not still if a stopping barrier was added in the experimental protocol. On the contrary we observe that even with the presence of the stopping barrier the system in the double ring configuration was not exactly still. In order to solve this problem we start we initially realize a half-stopping barrier, cutting the sample only for a radius of the disk, not in the full diameter as in the single ring case. In the previous configuration the single ring is fully disconnected in two half rings, whose phase can evolve independently. When the barrier is removed and the ring is connected, the accumulated phase difference can generate a current in the ring. In the half-stopping barrier case, the ring is not fully disconnected and therefore we expect a more stable situation, as confirmed experimentally. However the system circulation states at the end of the process was still observed. In order to create a still gas we try to reduce the intensity of this barrier. In particular, we start to see a more stable gas when the intensity of the stopping barrier is reduce to low value, such that the atomic sample is not full disconnected, namely the density in the region of the stopping barrier was not zero. We finally obtain a completely still system by completely remove the stopping barrier. A possible explanation for this is that, when stopping barrier on, the evolution of the phase on the side of the barrier is independent, and, as before, can lead to a circulation state when the barrier is removed. When no barrier is present, this phenomenon do not occurs. In order to understand why the gas was stable in the single ring case also with the presence of the stopping barrier we need to underline that

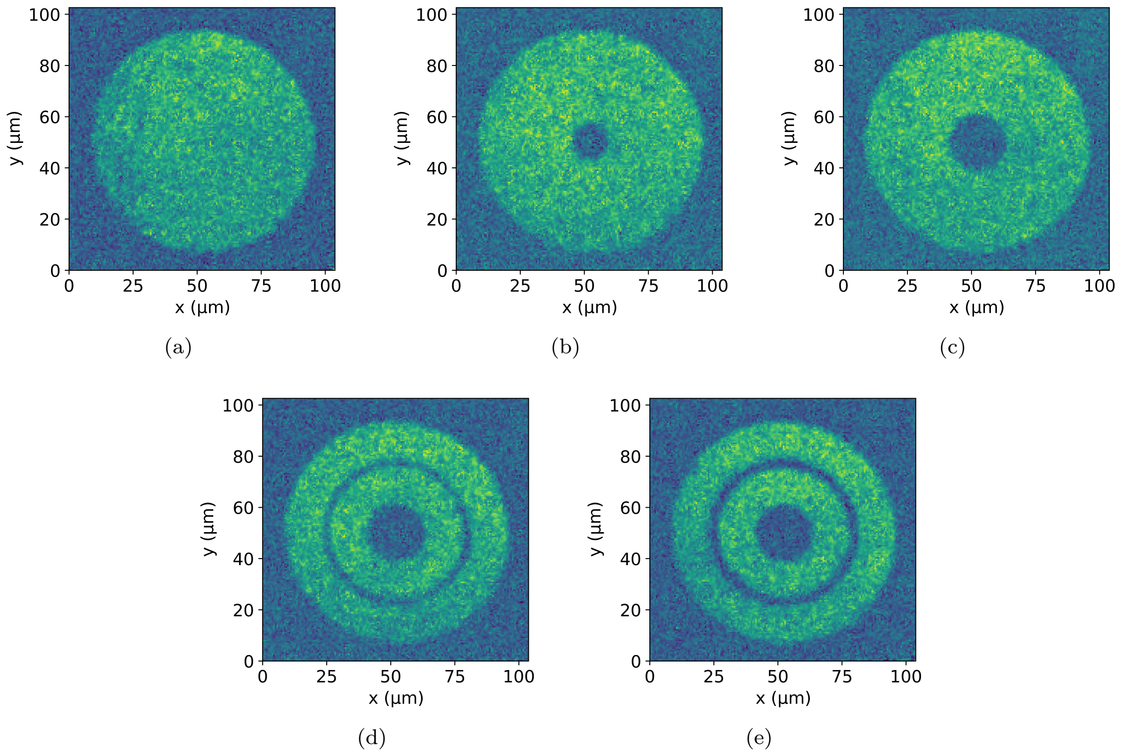

Figure 4.3: Experimental protocol implemented for the excitation of persistent current in the double.ring geometry. From the cigar shaped trap squeezed in the vertical direction by the $TEM_{0,1}$ laser, atom are first trapped in a homogeneous disk (a). From this configuration we start to cave hole in its centre, by shining a small repulsive disk and successively increasing his radius (4.3b) up to the final configuration in 4.3c Then the circular barrier is ramped up with a sequence of 15. In the final configuration the system is in a double-ring configuration as in 4.3e.

the experimental procedure for the double ring realization need more time with the stopping barrier on (if it is present) and therefore the possible phase evolution is larger.

From the initial configuration of a disk in Fig. 4.3a, we start to cave hole in its centre, by shining a small repulsive disk and successively increasing his radius (4.3b) up to the final configuration in 4.3c, with a radius of the hole of $9.95\,\mu$m, the same of R_{in}. This procedure is adiabatically realized with a sequence of 57 different DMD images from, separated in time by 0.5 ms, in order to not excite the system. Then, after 10 ms of equilibration in this geometry, the circular barrier is ramped up with a sequence of 15 images separated by 2 ms. In the final configuration the system is in a double-ring configuration as in 4.3e. In this system, we usually load $\sim 10^4$ pairs. At this point, persistent currents in the sample are created by using the phase imprinting method.

4.1.2 Excitation and detection of persistent current in a double-ring geometry

Like in the single ring case, also in this configuration we excite persistent currents in the two rings using a proper DMD light pattern. The high resolution of the vertical imaging system allows to create independent intensity profile for each ring. In particular we can choose to realize intensity profile with different gradient of the intensity, or different number of gradients in the two rings. Furthermore it is possible to shine the sample in the two ring for different imprinting time. By combining all this possible arbitrary independent parameter, we can excite the system in a state with with on demand circulations w_i for the inner ring and w_o for the outer one. However, for the first study connected to the double ring geometry ,The realization of the Kelvin-Helmholtz instability in one component superfluids, we are interest only in the excitation of state like $w_i = -w_o$, with opposite circulation in the two rings. More complicated combination of the circulation can be useful for future investigation, like the observation of Josephson effect in the two ring superfluid configuration with different circulation states.

In order to detect the state of the circulation state system, we perform interferometric measures between the two rings. In this case the inner circle is not present, but from the interference pattern between the two rings we can obtain information on the relative circulation $w_o - w_i$ as it is explained in the following. Starting from Eq. 2.12 for the interference pattern between the ring and the inner disk, we can rewrite this formula considering the interference between the inner ring, with phase $\phi_i(\theta)$, and the outer ring, whose phase is $\phi_o(\theta)$. The interference term takes the form:

$$\cos\Big(2\pi\frac{r}{\lambda} + \phi_i(\theta) - \phi_o(\theta)\Big). \tag{4.5}$$

However, in this case both $\phi_o(\theta)$ and $\phi_i(\theta)$ depend on the angular coordinate θ. In particular, considering a state with circulations w_i and w_o, is possible to write the phases as $\phi_i(\theta) = w_i\theta$ and $\phi_o(\theta) = w_o\theta$. Therefore the interference term is:

$$\cos\Big(2\pi\frac{r}{\lambda} + (w_i - w_o)\theta\Big). \tag{4.6}$$

As a result, the same consideration done for Eq. 2.13 can be applied also in this case, considering $(w_i - w_o)$ instead of w. Therefore the interference pattern of the double ting will also shown spirals, and the number of arms correspond to the value of $|(w_i - w_o)|$. In order to identify the sign of $(w_i - w_o)$ we note that the spirals are clockwise for $(w_i - w_o) < 0$ and anticlockwise if $(w_i - w_o) > 0$. Therefore from the interference between the two ring is possible to extract the relative circulation between them. Despite all the possible configurations for imprinting in the two rings are potentially implementable, in the following we will always consider the case in which we imprinting each ring for the same imprinting time Δt, with the same number of gradient, but with opposite direction of the gradient in the intensity pattern, creating circulation state with opposite sign.

In the last part of this section, I will present the characterization of the relative circulation $\Delta w = w_i - w_o$ versus the imprinting time for different configuration of the imprinting pattern and the corresponding observed number of vortices generated by the imprinting procedure. This characterization is interesting for the study of the persistence of currents in the double ring geometry. Furthermore, the calibration of the relative circulation is useful for the determination of the initial condition of the Kelvin-Helmholtz instability I will introduce in the last section of this chapter. For this purpose, also the number of imprinting vortices in the sample has a crucial role.

Fig. 4.4 shows the evolution of the number of vortices $\langle N_v \rangle$ generated by the imprinting procedure for different imprinting time Δt. The result in this case are relative to an phase imprinting realized using one gradient in the DMD pattern. However two imprinting pulses are performed. The number of imprinted vortices is observed to exponentially decay in time. Fig. (b) and Fig. (c) show the number of vortices in the inner and the outer ring only. The lines in the figures are exponential fit.

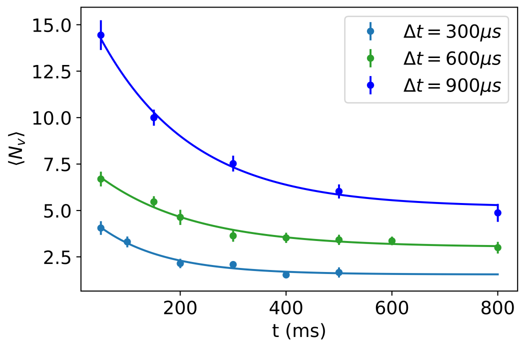

(a) Total vortices

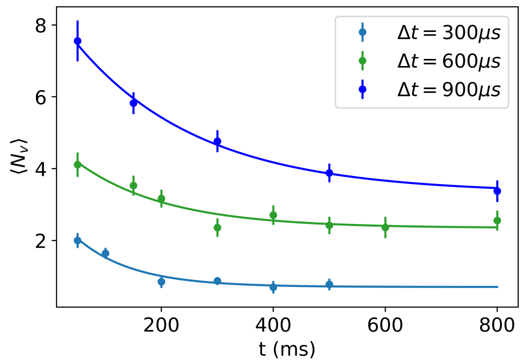

(b) Vortices in the inner ring

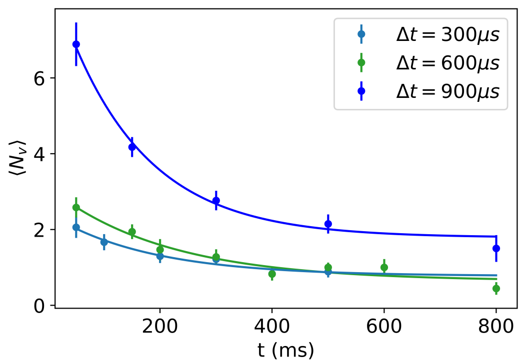

(c) Vortices in the outer ring

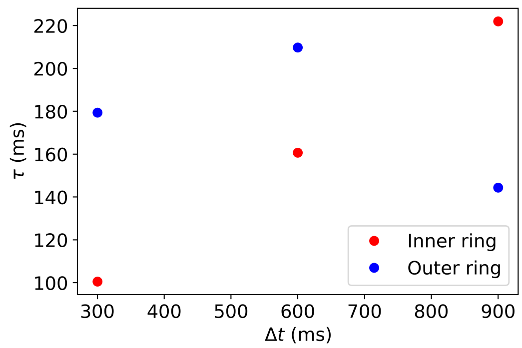

(d) Decay time pf the exponential decay

Figure 4.4: Exponential decay of the imprinting vortices in the double ring configuration. The results are relative to an imprinting protocol with a single gradient imprinting pattern. The imprinting is performed two times. (a) shows the number of total vortices varing the holding time t after the imprinting. (b) and (c) show respectevly the evolution of number of vortices in the inner and the outer ring. In (d) is plotted the decay time obtained from the fitting for different imprinting time Δt.

As we can see, the imprinting vortices in the inner ring are initially more than those in the outer ring. Furthermore, the number of vortices in the inner ring, show a slower decay down to a higher final value. A possible explanation of this effect is that the presence of the external ring reduces the possibility for the vortices to escape from the inner ring, since it influences the boundary conditions of the inner ring. However is important to underline that the observed high number of vortices in this case is due both to the long imprinting time used, in particular high number of vortices are generated for $\Delta t = 900\,\text{ms}$, and to the implementation of the double pulse. In general, the use of a multiple gradient pattern is preferable respect to the use a multiple pulse imprinting protocol considering the lower spurious vortices generated. As a consequence, in order to excite persistent current, in the system, we usually use a single pulse with, in case, a multiple gradient pattern. In particular we use the single and four gradient pattern.

In order to acquire control on the generation of persistent currents in the double ring configuration, we realize a calibration for both 1 and 4 gradients imprinting patterns. The results are shown in Fig. 4.5 Some interesting features arise from these plots. The number of circulation and spurious vortices are measured 300 ms after the imprinting procedure. From the number of imprinted circulation in the one gradient case (Fig. 4.5(a))we observe a linear increase up to a saturation at around$\Delta w = 12$. This

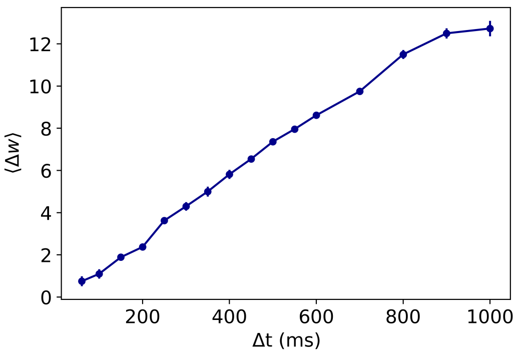

(a) 1 gradient, Relative ciruclation calibration

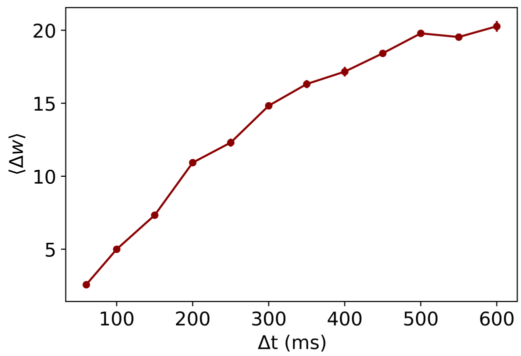

(b) 4 gradient, Relative ciruclation calibration

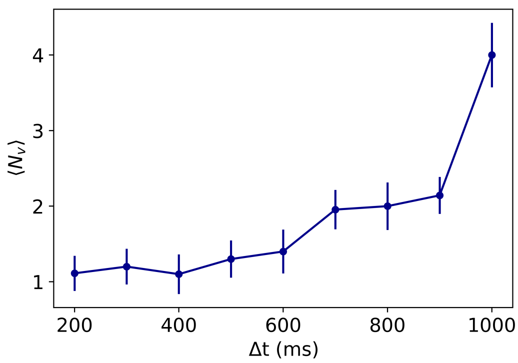

(c) 1 gradient, Spurious vortices calibration

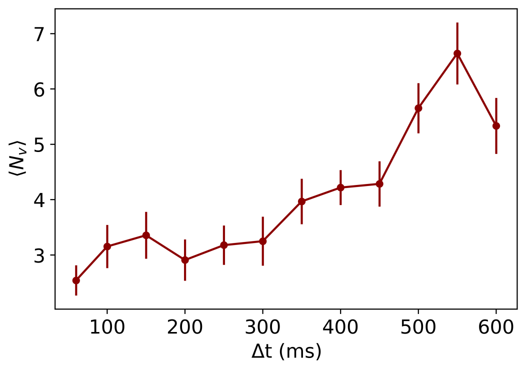

(d) 4 gradient, Spurious vortices calibration

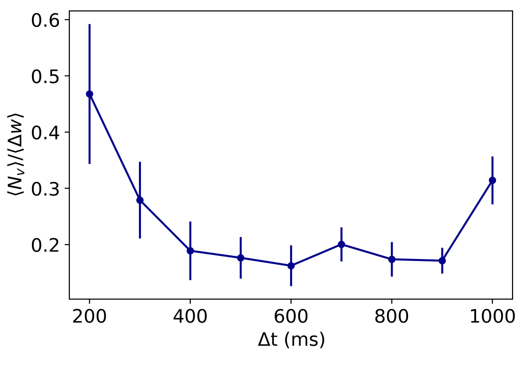

(e) 1 gradient, Spurious vortices over number of spirals

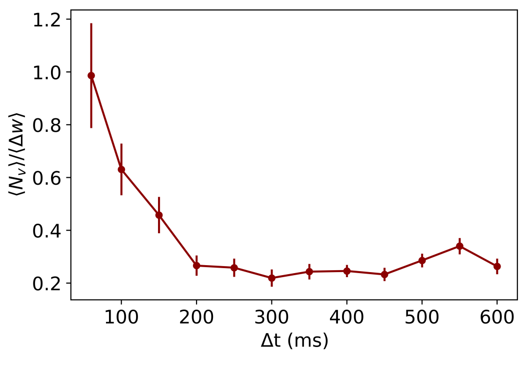

(f) 4 gradient, Spurious vortices over number of spirals

Figure 4.5: Characterization of the imprinting procedure in terms of the relative circulation and the number of spurious vortices versus the imprinting time Δt. the plot on the left are relative to the single gradient case, the ones on the right to the 4 gradient case. The upper and middle panels report the number of relative circulation and number of spurious vortices from the imprinting measured 300 ms after the imprinting procedure. The lower panels represent the number of measured vortices divided by the number of corresponding circulations.

is comparable with the limitation of the imprinting procedure observe for the single ring geometry. In that case, in fact, the imprinting using only one gradient and one pulse in the BEC was able to excite a maximum of $w = 6$ (this limitation arises from the too long imprinting time, that make the condition of short Δt fall). Considering that now we are exciting two ring with opposite circulation, the results are in agreement. We consider now Fig. 4.5(b), representing the number of circulation versus the imprinting time for the 4 gradient case. Here a interesting trend is observed: Δw increases linearly with Δt up to $\Delta t = 350\,\mu$s, corresponding to a relative circulation $\Delta w = 16$ (circulation $\pm$ 8 in each ring). For $\Delta t > 350\,\mu$s, the dependence is still linear, but with a different slope. Finally, for high values of the imprinting time, a saturation is observed. The explanation of this behaviour is understandable in therm of the maximum persistent circulation in the rings. The change of slop in the linearly increase of the relative circulation occurs for the imprinting time corresponding to the excitation of $w_i = 8$. This correspond to the critical persistent circulation in the single ring geometry. In this case the inner radius of the internal ring is the same of the single ring geometry. Thus the same maximum persistent circulation is expected[1]. However, this argument is valid only for the inner ring, cause the external one has a bigger inner radius and thus can support higher circulations. Therefore the change of the slope arise from the fact that, for $\Delta t > 350\,\mu$s, increasing the imprinting time we increase the circulation only in the external ring. Finally, the saturation occurs when also for the external ring the maximum persistent circulation is reached, which correspond to a relative circulation of $\Delta w = 20$. Considering that here $w_i = 8$, we expect a circulation of $w_o = 12$. This value is consistent with the saturation value observe in Fig. 2.13, considering that the external ring has a radius of $\simeq 30\,\mu$m. However, it is possible that limitation from the imprinting procedure arises also in this case. In order to realize state with $\Delta w > 12$ we need necesarly use the 4 gradient imprinting pattern. However, the state with $\Delta w > 16$ are formed by a state with unbalance circulation in the rings $w_i = 8$ and $w_o = -(\Delta w - 8)$.

We consider now Figs 4.5(c-d). They show the number of vortices coming from the imprinting procedure that survive after 300 ms. For low values of the imprinting time, the number of spurious vortices is almost constant, only a slightly linear increase in observable. However, this minimum number of vortices is higher in the 4 gradient case. In (c) an abrupt increase of vortices is observed in proximity of the saturation of the relative circulation. A similar behaviour is observed in (d). In particular here it is observed both when we have the saturation of the circulation in the inner ring (a small step increase is observed at $\Delta t = 350\,\mu$s) and when the saturation occur in the outer ring. A possible explanation is that, in the 4 gradient case, some vortices can arise from the decay of high circulation state to the maximum persistent circulation.

Finally we consider the two lower plots (e-f). These represent the ratio between the number of imprinting vortices and the number of excite circulation state as a function of the imprinting time. This plot is important in order to confront which is effectively the better way to excite persistent currents in the two rings. By comparing the two plots we observe that in order to excite up to $\Delta w = 10$, the simple gradient is convenient. This is understandable considering that for the 4 gradient case wa have always at least 3 spurious vortices. Due to the abrupt increase of vortices in the one gradient case, in proximity of the saturation, for $\Delta w > 10$ the 4 gradient pattern reveals more convenient. In the realization of the desired circulation state, we have considered the results obtained from this calibration, in order to use the more convenient pattern for each situation. Anyway, the number of spurious vortices in the sample after 300 ms is always at least the 20 % of the relative circulation.

It is important to notice that measurements are performed 300 ms after the imprinting procedure make both the imprinting vortices decrease in time and the possisble not persistent circulation to stabilize to the maximum persistent circulation. This effects are important in the experimental realization with high control on the preparation of the system, because in this case is not desiderable to work with spurious random vortices and circulation state that decay in time

[1]As we have argue in the previous chapter, that the maximum winding circulation depend on the inner radius of the ring

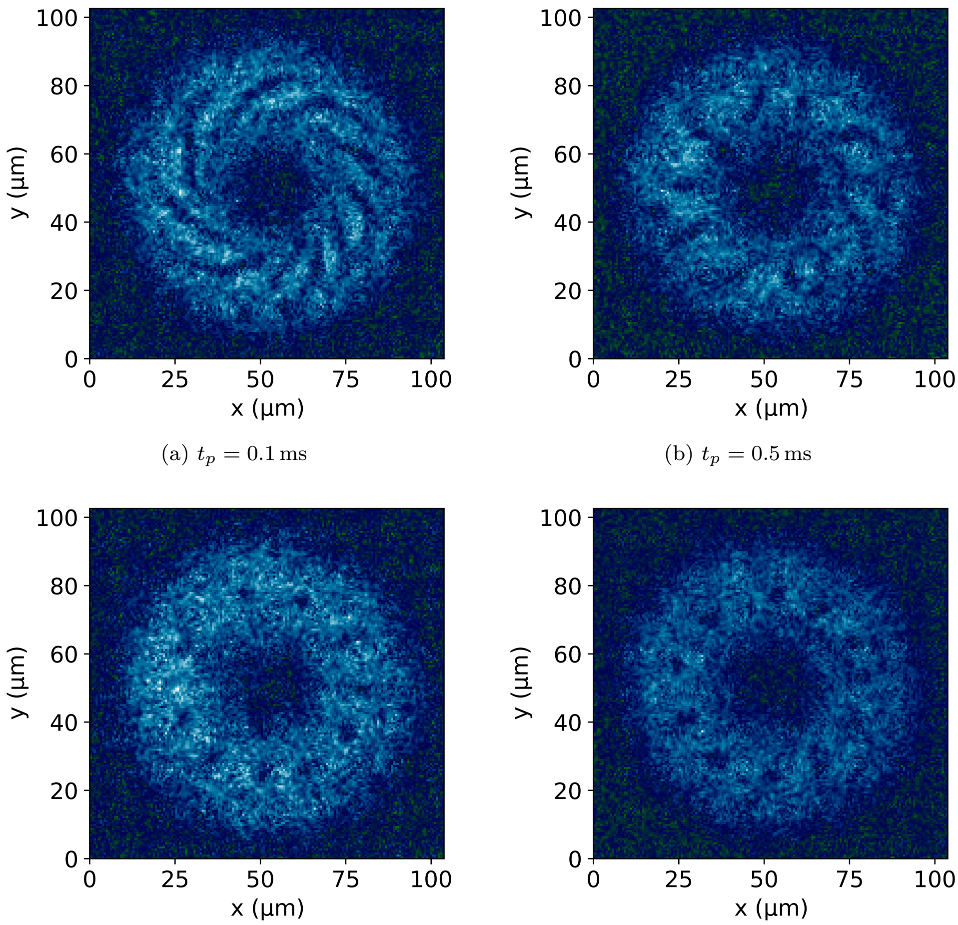

(a) $t_p = 0.1\,\mathrm{ms}$

(b) $t_p = 0.5\,\mathrm{ms}$

(c) $t_p = 0.8\,\mathrm{ms}$

(d) $t_p = 0.9\,\mathrm{ms}$

Figure 4.6: Merging of the two-ring condensates after removing the circular barrier separating them. A ramp of 15 images with different barrier heigh is performed. Subcaptions indicates the time between the picture t_p. For a fast removal of the barrier we observe the formation of a spiral soliton [70], for slow ramping down, an array of vortices is formed. Images are obtained by a single absorption imaging with a 1.5 ms TOF in the BEC side. The relative circulation before the rampdown of the circular barrier is $\Delta w = 10$ for each images.

4.2 Merging two rotating condensed rings

In the previous section we described the procedure for the excitation of circulation in the two ring configuration. Moreover currents are observed to persist also in this configuration, and we show the method used for obtaining the relative circulation of the two rings $\Delta w = w_i - w_0$. In order to observed interesting physical effects we remove the circular barrier separating the two rings. This procedure allows the study of dynamical instabilities arising from a system initially prepared with two counterflowing persistent currents.

Starting from the configuration in Fig.4.3e, after the excitation of the desired circulation state with the phase imprinting procedure, we wait 300 ms in order to let the number of spurious vortices decreases. Then, the circular barrier separating the two condensates is lowered down with a series of 15 images with a decreasing intensity of the barrier. The final state that we obtain depend on the

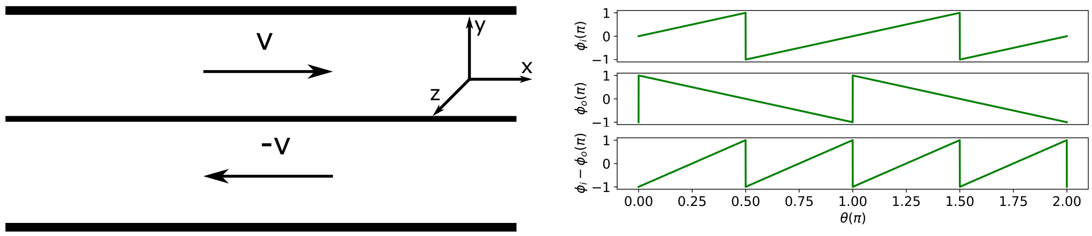

(a) (b)

Figure 4.7: (a) Model of double-ring as two linear channels with opposite flow and periodic boundary conditions. (b) Ohase dependence on the angular coordinate θ for the superfluid in the inner ring (ϕ_i), in the outer ring (ϕ_o) and the difference in phase between the two superfluid for $w_i = -w_o = 2$

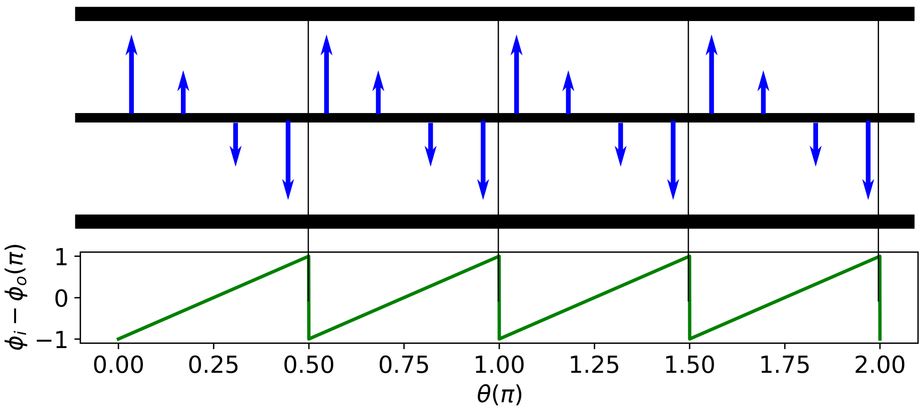

Figure 4.8: Schematic representation of the spiralic soliton formation. Blu arrows indicates the velocity of the soliton. Due to the different $\Delta\phi$ for different angular position , this velocity depends on θ. When the jump discontinuity is present, the velocity of the soliton changes its sign and the line breaks in a spiralic soliton. The observed number of arms correspond to Δw.

duration of the barrier removal. Fig. 4.6 shows the final state for different value of the t_p. When the barrier is removed in a fast way, a spiral soliton structure appears (a). However, slowing down the time necessary to remove the circular barrier, an array of vortices is formed. This results are obtain for the gas in the BEC side. The images are relative for a relative circulation of $\Delta w = 10$.

4.2.1 Fast barrier removal

In order to understand the formation of the regular structure showed in Fig.4.6 we consider the phase pattern of the system. As we already mentioned, in my study I consider situation in which we imprint for the same imprinting time and with the same number of gradient in the two rings, but opposite directions. As a result the two rings are excited, at least in the low imprinting time case, in opposite circulation states $w_i = w$ and $w_o = -w$. Therefore the corresponding velocity in proximity of the separation surface (at the same radial position) satisfies $v_i = -v_o$. We can model our double-ring configuration as the two straight channel of Fig. 4.7a), where the velocity is constant along the channel. Fig. 4.7b shows the phase dependence on the angular position θ for the superfluids in the inner and in the outer rings for the $\Delta w = 4$ case. The phase difference is also plotted. This last quantity is fundamental for understanding the mechanism underlying the formation of system like in Fig. 4.6. It is important to notice that the phase difference shows a series of jump discontinuities,

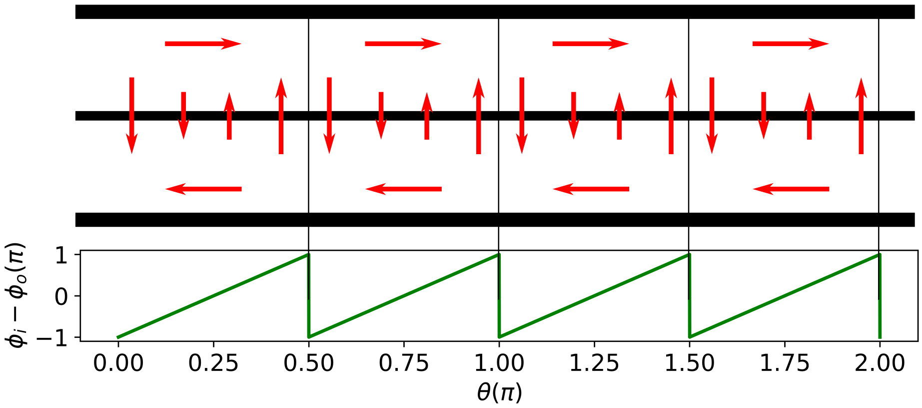

Figure 4.9: Schematic representation of the vortices array formation. Blu arrows indicates the velocity of the soliton. Due to the different $\Delta\phi$ for different angular position , this velocity depends on θ. When the jump discontinuity is present, the the velocity of the soliton changes his sign and the line breaks in a spiralic soliton. The observed number of arms correspond to Δw.

that are equal in number to the relative circulation $\Delta w = w_i - w_o$.

When the barrier removal is fast, a spiral soliton structure is observed [70]. Considering a 1D system, solitons in BEC are solution of the Gross-Pitaevskii equation [2, 55] consisting in a region of the condensate where a density depletion is present. At the two side of the depletion a change of phase $\Delta\phi$ is observed. This modulation of the density moves in the sample preserving its shape in time. The soliton moves in the sample with a velocity opposite to the change of phase $\Delta\phi$ with a velocity of $v_{sol} \sim \cos(\Delta\phi/2)$ [71].

When the circular barrier is removed in a fast way, a soliton arises from the corresponding density depletion. However, due to the different phase jump depending on θ the velocity will be different. In particular, in correspondence of the jump discontinuity of the phase difference, the soliton move in opposite direction at the two side of the discontinuity and it must break. As a results, a spiral soliton structure is formed, and the number of arms corresponds to the relative circulation Δw. A schematic explanation of the spiral soliton generation is showed in Fig. 4.8. The formation and the time evolution of this soliton structure will be subject of future investigations.

4.2.2 Slow barrier removal

When t_p is long enough, the final state is formed by an array of vortices equally spaced along the angular direction [69]. As for the previous case, the cause is the changing phase difference between the two ring along the θ coordinate. Considering that the velocity field is proportional to the gradient of the phase, this will lead to a velocity across the separation that depend on the angular position. The velocity field is schematically shown by the red arrows in Fig.4.9. It is important to notice that when the difference of the phase between the two superfluids has a jump discontinuity, the velocity field changes the sign. When this behaviour is added to the flow in the external and the internal ring, is possible to understand that the fluid flows around this points of the interface. This points immediately evolve in quantized vortices with the same charge. The number of vortices created N_v is the same of the number of discontinuity of the difference of phase between the two rings. As a consequence we are able to create an array of vortices in number $N_v = \Delta w$. Due to the linear dependence of the phase in both the ring on θ, the position of vortices is equally spaced.

A possible explanation for the fact that different final configuration are obtained for different t_p is the following: considering the fast removing , the region before occupied by the circular barrier gives rise to a density depletion. When the ramping down of the circular barrier is completed, this density depletion form the soliton structure. On the other hand, when we gradually reduce the intensity of the circular barrier, a flow between the two rings can occurs before the barrier is completely removed, with the velocity field given by the difference in phase as I have just explained. In this case the vortices are formed. The final configuration consists in a single ring and a crystal of vortices equally spaced. The experimental results about this configuration for different value of Δw, and consequentially for different number of vortices are shown in Fig. **??**. As it is possible to see, spurious vortices coming from the imprinting procedure are often present. This images, like the images of the next section, are obtained with the TOF imaging procedure described in the previous chapter for the detection of vortices arising from the decay of persistent current in the single ring.

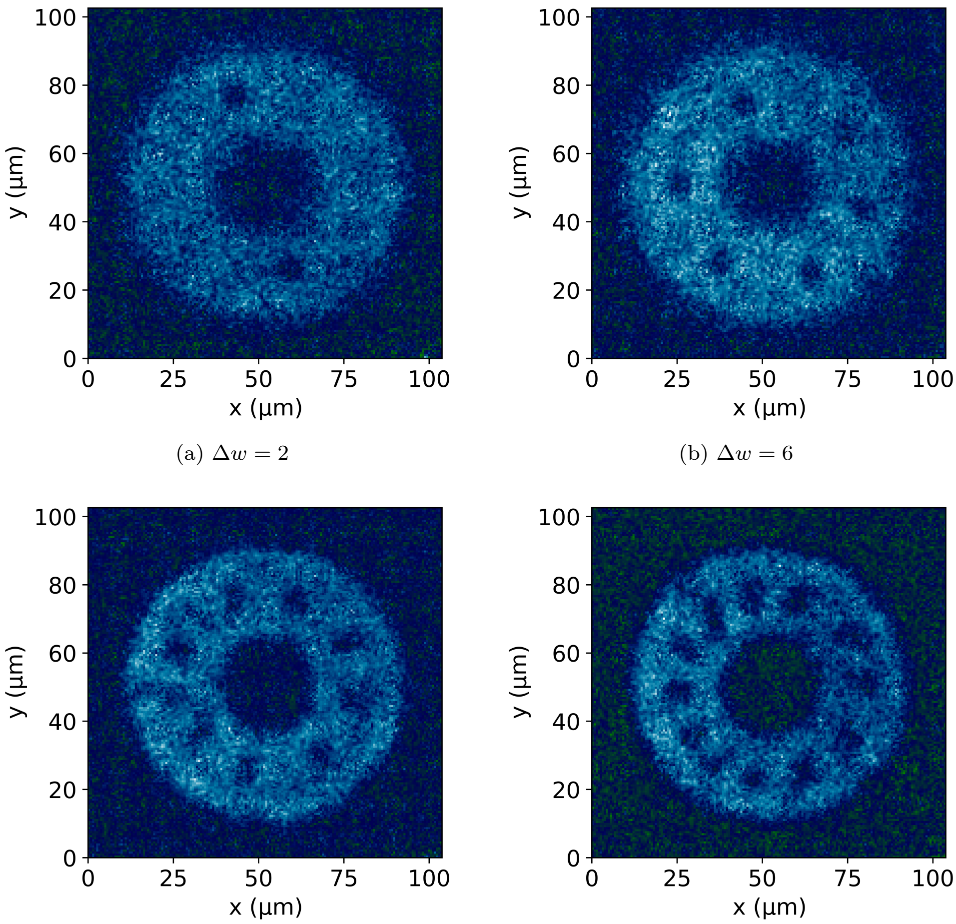

(a) $\Delta w = 2$ (b) $\Delta w = 6$

(c) $\Delta w = 8$ (d) $\Delta w = 12$

Figure 4.10: Crystal of vortices arising from the merging of the two rings. Subcaptions indicate the value of Δw before the removal of the circular barrier

4.3 Kelvin-Helmholtz instability in a one component superfluid

In the previous section, I presented the procedure used in our experiment to realize an array of vortices equally spaced in a ring. However, this configuration is not stable. In particular the array of vortices is observed to break itself after tens of ms. The motion of the vortices can be related to a well known instability that occurs in classical fluids: the Kelvin-Helmholtz instability. In the last section of Chapter 1 I present the basics of this instability. As it is shown, this instability occurs in the separation surface between two classical fluids. The Kelvin-Helmholtz instability occur both in the case of a jump discontinuity between in the surface of separation between the two fluids with different velocity and in the case that two fluids with different velocities are separated by a shear layer with a continuos change in the velocity field. In this last case a quenching of the instability for high k is predicted. It is important to notice that the mathematical description of the KHI the instability occurs also for fluids with zero viscosity. Therefore we can expect that it will take place also in the inviscid flow of superfluids.

As a demostration, effects of the KHI have been observed in the superfluid phase of ^3He [72, 73]. In the last years the Kelvin Helmholtz instability has been studied also in Bose Einstein condensates. Experiment and numerical studied on this instability have been performed considering two merged heterogeneous Bose Einstein condensates [74, 75, 76]. In this case, the separation surface is well defined and the instability is observable by detecting the surface displacement like in the case of classical fluids. Furthermore, as we point out in the first chapter, the evolution of the instability leads to the formation of vorticous structures like in Fig. 1.7. In the case of two components BECs, this dynamics creates quantized vortices in the sample.

It is important to notice that KHI takes place when the density of the two fluids are equal. In particular it can happen also in one component fluids. Numerical calculation for the KHI in a one component superfluid ha been performed in [69, 77]. In the case of one component superfluids, as we have already saw, when the two counter-flowing superfluids merge, an array of equally spaced vortices appears in the separation surface. Therefore the evolution of this instability is detectable by tracking the position of this vortices. In particular, the vortices in the initial configuration track the position of some equally spaced point of the virtual separation surface. This argument can appear misleading. In fact, in two component counter-flowing fluids, KHI is responsable to the generation of vorticous regular structure like in Fig. 1.7. In the single component case the regular array of vortices is not the results of the KHI, but rather the starting point of the instability. The vortices only track the position of the initial separation surface. Their formation is only obtained from the phase difference between the two condensate ring, a purely quantum property, and therefore is not related to the KHI. The dynamical instability as it is observed in our system is described in the following. We consider the starting point ($t = 0$) as the moment in which the circular barrier separating the two condensate is completely removed, at which we have the array of vortices configuration. Then we let the system evolve. As soon as a perturbation acts on the separation surface, namely when the position of a vortex is perturbed respect to the ideal position in the radial direction, this will increase exponentially, following the dispersion relations discussed in the first Chapter. As a result, we expect to observe a radial displacement of the vortices position. However, in analogy to what is observed for the classical fluids the vorticous structure already mentioned that appears in two component fluid, in this case, consists in a displacement of the vortices position in the azimuthal direction. The combination of the radial and angular displacement of the vortices position leads to the formation of clusters of vortices, al least in the first evolution of the system. The images of the system following this evolution are shown in Fig. 4.13.

From both the dispersion relation in Eq. 1.46 and Eq. 1.41, we expected modes with high values of k to exponentially increases with a lower time constant. Furthermore, not all the mode are revealable in our system. In particular, considering the periodically boundary condition, that actually are present in our ring geometry, the possible k are limited to value of $k = n/R_B$, with n is an integer number and R_b is the radial position of the circular barrier. Furthermore, considering that our surface in the initial configuration is formed by a regular array of vortices, we are limited by a maximum k in our observations, that are based on the position of the vortices. An estimation of the maximum observable k is $k = N_v/2R_b$. The wavelength of this mode is double the distance (along a circumference of radius R_b) between vortices and correspond to a opposite displacement in the radial direction for adjacent vortices. Further, considering the background velocity in the rings, adjacent vortices are also displaced in opposite azimuthal direction. As a result, we expected that, in the first part of the dynamic, the instability evolves from the crystal of vortices, to a sequence of cluster formed by two vortices. Subsequentially the modes with lower k become important, and the system is expected to evolve into a configuration with cluster formed by a bigger number of vortices. This effects is visible in Fig. 4.13, at least for short evolution time t.

4.3.1 Analysis on the Kelvin-Helmholtz instability

In this last part of the section I present a first approach to the a possible analysis for the study of the dynamical instability of the vortices array, consisting in the analysis of the Fourier transform of the density. The procedure is explained in the following. For different each holding time after the complete removing of the circular barrier we acquire 30 images. For each of that the study the system in polar coordinates (Fig. 4.11) The resulting density profile in Fig. 4.11b is then integrated along the radial direction to obtain the integrated density profile along the azimuthal direction is obtained. The Fourier transform of the obtained quantity is then performed for each image, and then averaged over the 30 repetition is performed. Fig. 4.11 shows the trend of the average Fourier transform versus time, with k_θ obtained from the wave vector along the circumference $k_\theta = k/R_b$.

Considering the initial condition, the Fourier spectra at $t = 0\,\mathrm{ms}$ are expected to have a maximum value for $k_\theta = N_v$. In this case the system is prepared in a state with an array of 16 vortices. During the evoltion the crystal of vortices breaks down. When clusters of vortices are formed we expect that the Fourier trasform will present a maximum for lower value of k_θ, signaling the existence of a new order in the system . As a consequence, the obteined data shows a shift of the maximum of the Fourier trasform to lower value of the k_θ.

Further detailed analysis of the data, in order to exctract quantitative information from the data, are on going.

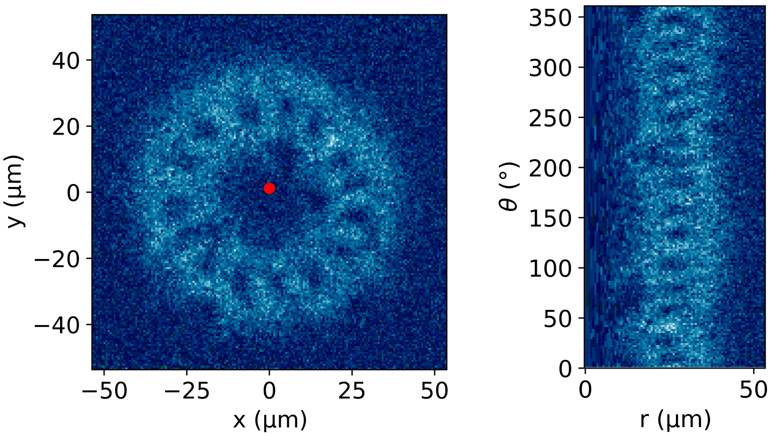

(a) (b)

Figure 4.11: (a) Images of the array of vortices at $t = 0\,\mathrm{ms}$. (b) Unwrapped density around the red spot in (a) used for the analysis.

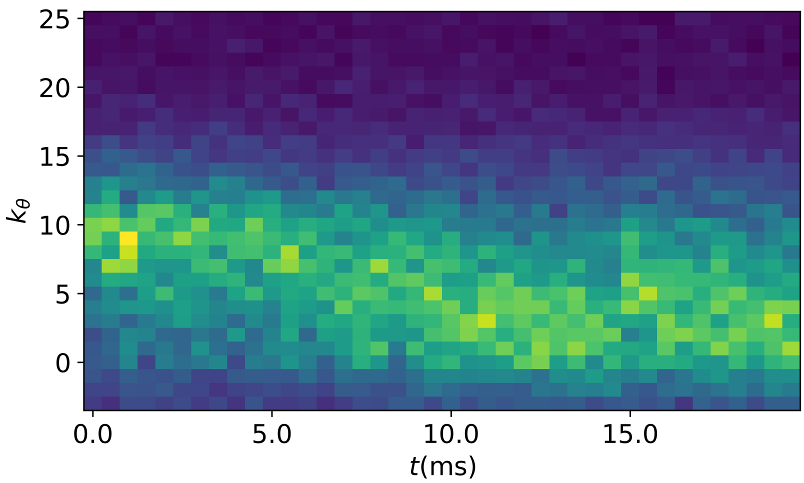

Figure 4.12: Time evolution of the Fourier transform. This result is relative to the case of 16 vortices in the initial array

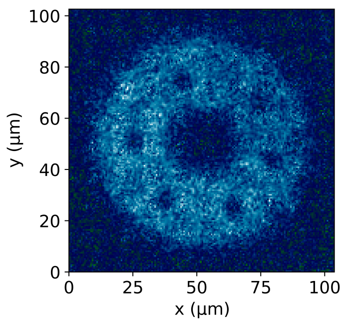

(a) $\Delta w = 6$, $t = 0\,\mathrm{ms}$

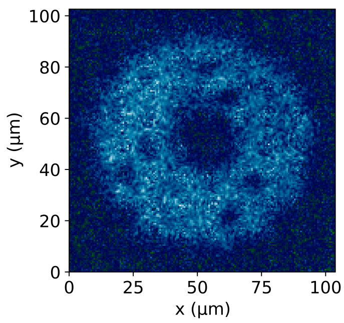

(b) $\Delta w = 6$, $t = 90\,\mathrm{ms}$

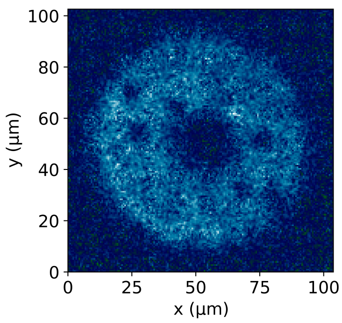

(c) $\Delta w = 6$, $t = 120\,\mathrm{ms}$

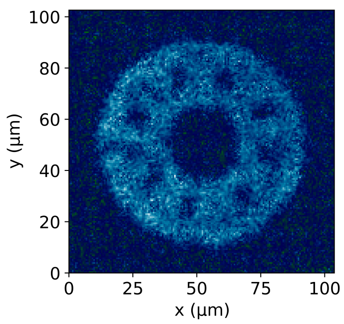

(d) $\Delta w = 8$, $t = 0\,\mathrm{ms}$

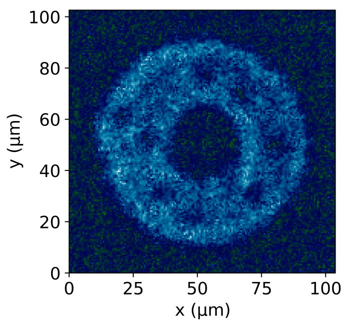

(e) $\Delta w = 8$, $t = 36\,\mathrm{ms}$

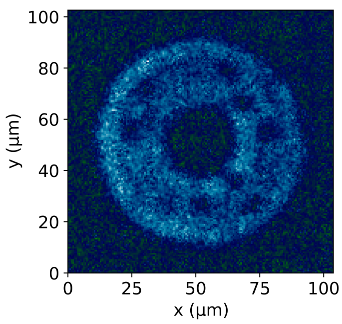

(f) $\Delta w = 8$, $t = 54\,\mathrm{ms}$

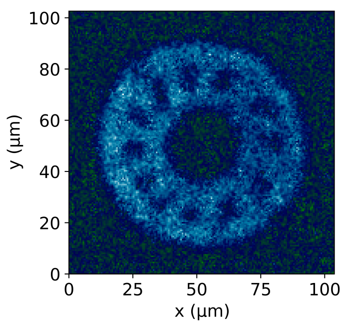

(g) $\Delta w = 12$, $t = 0\,\mathrm{ms}$

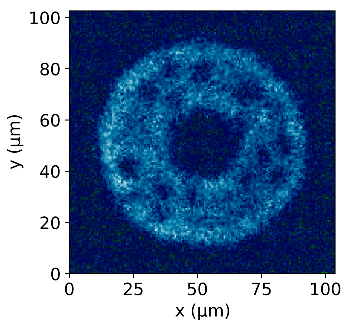

(h) $\Delta w = 12$, $t = 33\,\mathrm{ms}$

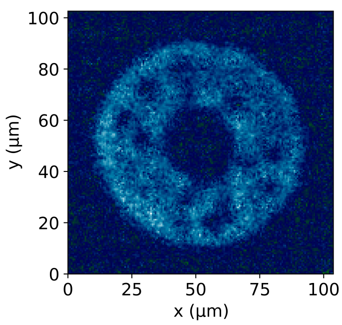

(i) $\Delta w = 12$, $t = 51\,\mathrm{ms}$

Figure 4.13: Dynamical evolution of the array of vortices for different values of relative circulation Δw before the removal of the circular barrier

Conclusions

In this thesis, I study the instabilities of persistent currents in fermionic superfluids in ring-shaped traps. In the first part of my work I study the behaviour of supercurrents in the presence of an obstacle across the BEC-BCS crossover. Via interferometric measurements we track evolution of the circulation state of the system. From our observations, the Unitary regime shows to be the more stable one. In particular no decay occurs in this case. On contrary the BEC and BCS regimes shows the evidence of a critical circulation w_c above which a circulation decay is observed. Furthermore, the decay induced by the presence of an obstacle allows for the investigation on the type of excitations that arise from the dissipative process. In particular, we observe that the decay of circulation is driven by the nucleation of vortices in the system. We characterized the vortices emission in time and we observe that the number of total emitted vortices is comparable with the number of circulation lost in the decay process. Numerical simulation helped us in understanding the microscopic mechanism underling the vortices nucleation. A direct extension of this study is to probe persistent currents in the ring increasing the number of obstacles acting on the superfluid. Both regular and disordered configurations of the obstacles are allowed thanks to the DMD. The first case is particularly interesting considering the results obtained in numerical simulations: when the obstacles are placed in a regular array along the azimuthal direction, a decay process is observed only below a critical obstacle number, that depends on the initial circulation state, above which the system is stable. On this line, future investigation will probe the effect of a disordered configuration of obstacles on the decay process.

Successively, I put the bases for the study the effects of dynamical instability in counter flowing superfluids, by realizing a double ring potential using the DMD. A characterization of the system trapped in the double ring geometry has been performed, in order to understand how geometry effects and limitations arising from the phase imprinting can influence the maximum relative circulation in our system. We then study the merging of two condensed ring-shaped system exciting in opposite circulation state, removing the barrier used to create the two superfluid rings. In this case the effects of the macroscopic wave functions description of the system leads to the evolution of the counter flowing rings with formation of regular structures. In particular, when the barrier is removed in a fast way, we observe the creation of a spiralic soliton in the system. On the other hand, when the barrier is removed in a slower way, a regular structure of vortices is emerges in the system. Moreover, the regular array of vortices is not a stable state of the system. The evolution of their position is describable in term of a dynamical instability that occurs in classical fluids, the Kelvin Helmholtz instability. The detailed characterization of the system is useful in view of the realization of this dynamical instability. In the last part of the work, I present a preliminary analysis of this dynamics. However, more detailed analysis will be performed. The results discussed are limited to the BEC superfluid. Future investigation on the BCS and UFG regimes on the Kelvin-Helmholtz instabilities will possibly lead to observation of different behaviour in vortices dynamics, providing a way to obtain different physical properties of different type of superfluids. The characterization of the double ring geometry lead to the possibility of exploring the Josephson effects in this superfluid excited in circulation states. Via tunneling process, an exchange of circulation between the two superfluid is expected [78].

The platform used in this work opens for the study and the simulation of superfluidity. In particular disorder effect or dynamical instabilities can be studied in a controllable way.

Appendix A

Atomic Structure of ^6Li

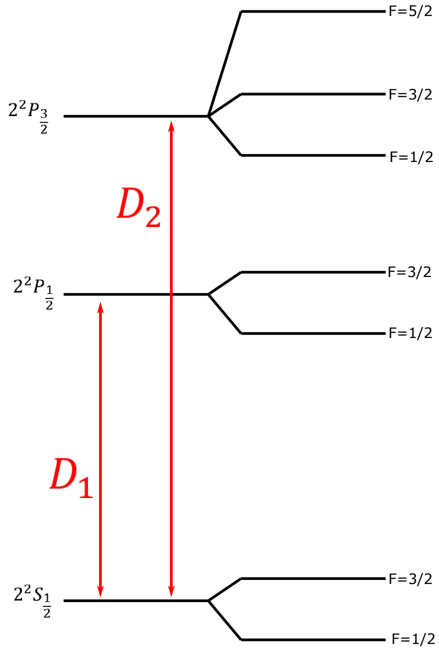

Figure A.1: Fine (left) and hyperfine (right) structure for the lowest energy levels of ^{6}Li atoms in absence of magnetic field. The spin-orbit coupling split the first excited state in two levels with angular momentum $J = 1/2$ and $J = 3/2$. The transition from the groun state to these are named D_1 and D_2 respectively. The hyperfine term creates a further splitting of the level with different total angular moemntum F.

The internal energy structure of atoms is extremely important for cooling technics and laser manipulation of atoms. Like others alkali atoms, Lithium has one valence electron and an internal closed shell. In this appendix are presented the atomic properties of the fermionic isotope, ^{6}Li. The ground state of the system is the $2s^1$ configuration for the valence electron, characterized by an orbital angolar momentum $L = 0$ and a spin $S = 1/2$. Optical radiation usually has not enough energy for excite internal electron so that in our case interesting electronic excited state are determined by the state of the unique valence electron. Therefore the first excited state will be given by the valence electron in the $2p^1$ state, with $L = 1$. The difference in energy in this two state arises when the coulombian interaction between the intern nucleus and the external electron is considered, taking in account the screening effect of the electron in the close shell. This is the gross structure of the atom.

However the possibility cool down atoms to degeneration and to manipulate them requires a more detailed description of the energy levels of an atom. One first correction consists in the *Spin-Orbit Coupling* $H_{fs} \sim \mathbf{L} \cdot \mathbf{S}$, that determinates the fine structure of the atom. This term represent the interaction between the electronic spin and the magnetic field created by the spin himself and is diagonal in the basis of the augenstates of the total angular momentum $\mathbf{J} = \mathbf{L} + \mathbf{S}$. Since $L = 0$ in the ground state, this term only split the excited state in two levels with $J = 1/2$ and $J = 3/2$ named i nthe spectroscopy notation ad $^2P_{1/2}$ and $^2P_{3/2}$. For the ^{6}Li case this separation is $\Delta E_{fs} = 10.05MHz$ [79]. The fine structure of fermionic lithium is showed in the left part of Fig. A.1. transitions from the Ground state $^2S_{1/2}$ to the two excited states $^2P_{1/2}$ and $^2P_{3/2}$ usally named as D_1 and D_2 respectively. In our case this two transition are both around $671nm$.

The subsequent correction arises from the interaction between the total electronic angolar momentum $\mathbf{J}$ and the angolar momentum of the nucleus $\mathbf{I}$ given by $H_{hfs} \sim \mathbf{J} \cdot \mathbf{I}$. This term is diagonal in the base of the total angular momentum gives rise to the *hyperfine structure*, in which energy states are split in level with different total angular momentum $\mathbf{F} = \mathbf{J} + \mathbf{I}$. The zero-field hyperfine structure of fermionic lithium is showed in Fig. A.1. In this case $I = 1$; therefore the ground state splits in two levels with $F = 1/2$ and $F = 3/2$.

A.1 Effect of a magnetic field

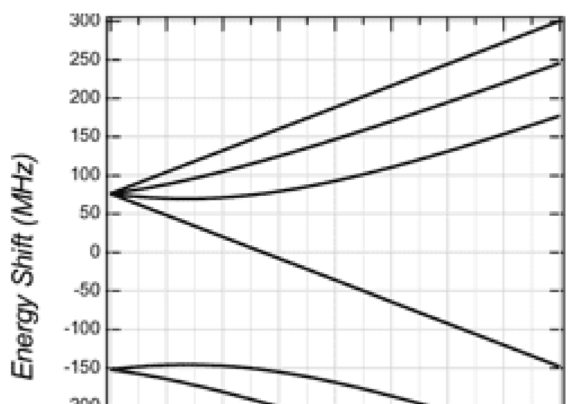

Figure A.2: Zeeman structure of fermionic lithium for the $^2S_{1/2}$ ground states. A linearly increasing splitting is observed for low magnetic field. When the Zeeman shift is much bigger than the hyperfine term, the fine structure split in level with different m_J. A further separation of states with different m_I is provided by by the hyperfine term. Image taken from [79].

The presence of a magnetic field $\mathbf{B}$ adds an additional term in the Hamiltonian $H_Z = -\mu \cdot \mathbf{B}$ know as *Zeeman effect*. μ is the magnetid dipole moment of the atom.

In case of low magnetic field, is possible to consider this term as a perturbation to the hyperfine structure. Is possible to show that the energy shift due to the Zeeman effect is given by $\Delta E = \langle H_Z \rangle = \mu_B B g_F m_F$; here m_F is the projection of the total angular momenta along the magnetic field. μ_B is the Bohr magneton and g_F is the Landé factor for the hyperfine structure. Therefore hyperfine states are splitted in levels with different m_F. In this particular regime, the energy splitting increase linearly with the magnetic field B.

In the opposite case for which the energy of the Zeeman effect is big respect to the hyperfine term, H_Z acts directly on the fine structure. As a result state splits in levels with different projection of the total electronic angular momenta along the magnetic field m_J. Then a further splitting is given by the hyperfine term. Good quantum number for describing the system in this case are $|J, m_J, I, m_I\rangle$

Fig.A.2 show the Zeeman structure of fermionic lithium for the $^2S_{1/2}$ ground states. A linearly increasing splitting is observed for magnetic field up to $20G$. For high values of B levels are gathered in two groups. The lower-energy one is formed by states with $m_J = -1/2$, the other one by $m_J = +1/2$ states.

Bibliography

[1] R. P. Feynman *et al.*, “Simulating physics with computers,” *Int. j. Theor. phys*, vol. 21, no. 6/7, 1982.

[2] L. Pitaevskii and S. Stringari, *Bose-Einstein condensation and superfluidity.* Oxford University Press, 2016, vol. 164.

[3] L. Landau, “Theory of the superfluidity of helium ii,” *Physical Review*, vol. 60, no. 4, p. 356, 1941.

[4] J. File and R. Mills, “Observation of persistent current in a superconducting solenoid,” *Physical Review Letters*, vol. 10, no. 3, p. 93, 1963.

[5] D. Loss and P. M. Goldbart, “Persistent currents from berry’s phase in mesoscopic systems,” *Physical Review B*, vol. 45, no. 23, p. 13544, 1992.

[6] R. Landauer and M. Büttiker, “Resistance of small metallic loops,” *Physical review letters*, vol. 54, no. 18, p. 2049, 1985.

[7] J. Clarke and A. Braginski, “The squid handbook: Applications of squids and squid systems. vol. 2,” 2006.

[8] Y. Aharonov and D. Bohm, “Significance of electromagnetic potentials in the quantum theory,” *Physical Review*, vol. 115, no. 3, p. 485, 1959.

[9] J. Sólyom, *Fundamentals of the Physics of Solids: Volume 1: Structure and Dynamics.* Springer Science & Business Media, 2007, vol. 1.

[10] N. Goldman, G. Juzeliūnas, P. Öhberg, and I. B. Spielman, “Light-induced gauge fields for ultracold atoms,” *Reports on Progress in Physics*, vol. 77, no. 12, p. 126401, 2014.

[11] S. Moulder, S. Beattie, R. P. Smith, N. Tammuz, and Z. Hadzibabic, “Quantized supercurrent decay in an annular bose-einstein condensate,” *Physical Review A*, vol. 86, no. 1, p. 013629, 2012.

[12] A. Ramanathan, K. Wright, S. R. Muniz, M. Zelan, W. Hill III, C. Lobb, K. Helmerson, W. Phillips, and G. Campbell, “Superflow in a toroidal bose-einstein condensate: an atom circuit with a tunable weak link,” *Physical review letters*, vol. 106, no. 13, p. 130401, 2011.

[13] W. Ketterle and M. W. Zwierlein, “Making, probing and understanding ultracold fermi gases,” *La Rivista del Nuovo Cimento*, vol. 31, no. 5, pp. 247–422, 2008.

[14] S. Inouye, M. Andrews, J. Stenger, H.-J. Miesner, D. M. Stamper-Kurn, and W. Ketterle, “Observation of feshbach resonances in a bose–einstein condensate,” *Nature*, vol. 392, no. 6672, pp. 151–154, 1998.

[15] A. Fetter, "Theory of a dilute low-temperature trapped bose condensate," in *Bose-Einstein condensation in atomic gases.* IOS Press, 1999, pp. 201–263.

[16] B. H. Bransden and C. J. Joachain, *Physics of atoms and molecules.* Pearson Education India, 2003.

[17] C. Chin, R. Grimm, P. Julienne, and E. Tiesinga, "Feshbach resonances in ultracold gases," *Reviews of Modern Physics*, vol. 82, no. 2, p. 1225, 2010.

[18] M. Bartenstein, A. Altmeyer, S. Riedl, R. Geursen, S. Jochim, C. Chin, J. H. Denschlag, R. Grimm, A. Simoni, E. Tiesinga *et al.*, "Precise determination of li 6 cold collision parameters by radio-frequency spectroscopy on weakly bound molecules," *Physical review letters*, vol. 94, no. 10, p. 103201, 2005.

[19] M. Zwierlein, "Novel superfluids, vol. 2," 2015.

[20] J. Bardeen, L. N. Cooper, and J. R. Schrieffer, "Theory of superconductivity," *Physical review*, vol. 108, no. 5, p. 1175, 1957.

[21] A. J. Leggett, "Diatomic molecules and cooper pairs," in *Modern trends in the theory of condensed matter.* Springer, 1980, pp. 13–27.

[22] D. Petrov, C. Salomon, and G. V. Shlyapnikov, "Weakly bound dimers of fermionic atoms," *Physical review letters*, vol. 93, no. 9, p. 090404, 2004.

[23] L. N. Cooper, "Bound electron pairs in a degenerate fermi gas," *Physical Review*, vol. 104, no. 4, p. 1189, 1956.

[24] J. Sólyom, *Fundamentals of the Physics of Solids: Volume 3-Normal, Broken-Symmetry, and Correlated Systems.* Springer Science & Business Media, 2010, vol. 3.

[25] C. Raman, M. Köhl, R. Onofrio, D. Durfee, C. Kuklewicz, Z. Hadzibabic, and W. Ketterle, "Evidence for a critical velocity in a bose-einstein condensed gas," *Physical Review Letters*, vol. 83, no. 13, p. 2502, 1999.

[26] N. Bogoliubov, "On the theory of superfluidity," *J. Phys*, vol. 11, no. 1, p. 23, 1947.

[27] W. Weimer, K. Morgener, V. P. Singh, J. Siegl, K. Hueck, N. Luick, L. Mathey, and H. Moritz, "Critical velocity in the bec-bcs crossover," *Physical review letters*, vol. 114, no. 9, p. 095301, 2015.

[28] D. Miller, J. Chin, C. Stan, Y. Liu, W. Setiawan, C. Sanner, and W. Ketterle, "Critical velocity for superfluid flow across the bec-bcs crossover," *Physical review letters*, vol. 99, no. 7, p. 070402, 2007.

[29] A. J. Leggett, "Superfluidity," *Reviews of Modern Physics*, vol. 71, no. 2, p. S318, 1999.

[30] R. Feynman, "Chapter ii application of quantum mechanics to liquid helium," ser. Progress in Low Temperature Physics, C. Gorter, Ed. Elsevier, 1955, vol. 1, pp. 17–53. [Online]. Available: https://www.sciencedirect.com/science/article/pii/S0079641708600773

[31] H. von Helmholtz, *über discontinuirliche Flüssigkeits-Bewegungen.* Akademie der Wissenschaften zu Berlin, 1868.

[32] L. Kelvin, "On the motion of free solids through a liquid," *Phil. Mag*, vol. 42, no. 281, pp. 362–377, 1871.

[33] L. D. Landau and E. M. Lifshitz, *Fluid Mechanics: Landau and Lifshitz: Course of Theoretical Physics, Volume 6.* Elsevier, 2013, vol. 6.

[34] F. Charru, *Hydrodynamic instabilities.* Cambridge University Press, 2011, vol. 37.

[35] M. Fedrizzi, "Observing persistent currents in annular fermionic superfluids," Master Thesis, Università degli Studi di Milano, 2020/2021.

[36] G. Valtolina, "„superfluid and spin dynamics of strongly interacting atomic fermi gases"," Ph.D. dissertation, proefschrift (Scuola Normale Superiore, Pisa, 2016), 2016.

[37] C. J. Foot, *Atomic physics.* OUP Oxford, 2004, vol. 7.

[38] H. J. Metcalf and P. van der Straten, *Laser Cooling and Trapping.* New York: Springer-Verlag, 1999.

[39] P. D. Lett, R. N. Watts, C. I. Westbrook, W. D. Phillips, P. L. Gould, and H. J. Metcalf, "Observation of atoms laser cooled below the doppler limit," *Physical review letters*, vol. 61, no. 2, p. 169, 1988.

[40] C. Cohen-Tannoudji and D. Guéry-Odelin, "Advances in atomic physics: an overview," 2011.

[41] A. Burchianti, G. Valtolina, J. Seman, E. Pace, M. De Pas, M. Inguscio, M. Zaccanti, and G. Roati, "Efficient all-optical production of large li 6 quantum gases using d 1 gray-molasses cooling," *Physical Review A*, vol. 90, no. 4, p. 043408, 2014.

[42] G. Del Pace, "„tunneling transport in strongly-interacting atomic fermi gases"," Ph.D. dissertation, proefschrift (Università degli studi di Firenze), 2021.

[43] R. Haussmann and W. Zwerger, "Thermodynamics of a trapped unitary fermi gas," *Physical Review A*, vol. 78, no. 6, p. 063602, 2008.

[44] H. Heiselberg, "Collective modes of trapped gases at the bec-bcs crossover," *Physical review letters*, vol. 93, no. 4, p. 040402, 2004.

[45] G. Del Pace, K. Xhani, A. M. Falconi, M. Fedrizzi, N. Grani, D. H. Rajkov, M. Inguscio, F. Scazza, W. Kwon, and G. Roati, "Imprinting persistent currents in tunable fermionic rings," *arXiv preprint arXiv:2204.06542*, 2022.

[46] C. Ryu, M. Andersen, P. Clade, V. Natarajan, K. Helmerson, and W. D. Phillips, "Observation of persistent flow of a bose-einstein condensate in a toroidal trap," *Physical Review Letters*, vol. 99, no. 26, p. 260401, 2007.

[47] S. Beattie, S. Moulder, R. J. Fletcher, and Z. Hadzibabic, "Persistent currents in spinor condensates," *Physical review letters*, vol. 110, no. 2, p. 025301, 2013.

[48] Y. Cai, D. G. Allman, P. Sabharwal, and K. C. Wright, "Persistent currents in rings of ultracold fermionic atoms," *Physical Review Letters*, vol. 128, no. 15, p. 150401, 2022.

[49] J. Brand and W. P. Reinhardt, "Generating ring currents, solitons and svortices by stirring a bose-einstein condensate in a toroidal trap," *Journal of Physics B: Atomic, Molecular and Optical Physics*, vol. 34, no. 4, p. L113, 2001.

[50] A. Kumar, R. Dubessy, T. Badr, C. De Rossi, M. d. G. de Herve, L. Longchambon, and H. Perrin, "Producing superfluid circulation states using phase imprinting," *Physical Review A*, vol. 97, no. 4, p. 043615, 2018.

[51] S. Eckel, F. Jendrzejewski, A. Kumar, C. J. Lobb, and G. K. Campbell, “Interferometric measurement of the current-phase relationship of a superfluid weak link,” *Physical Review X*, vol. 4, no. 3, p. 031052, 2014.

[52] R. Mathew, A. Kumar, S. Eckel, F. Jendrzejewski, G. K. Campbell, M. Edwards, and E. Tiesinga, “Self-heterodyne detection of the in situ phase of an atomic superconducting quantum interference device,” *Physical Review A*, vol. 92, no. 3, p. 033602, 2015.

[53] L. Corman, L. Chomaz, T. Bienaimé, R. Desbuquois, C. Weitenberg, S. Nascimbene, J. Dalibard, and J. Beugnon, “Quench-induced supercurrents in an annular bose gas,” *Physical review letters*, vol. 113, no. 13, p. 135302, 2014.

[54] M. Andrews, C. Townsend, H.-J. Miesner, D. Durfee, D. Kurn, and W. Ketterle, “Observation of interference between two bose condensates,” *Science*, vol. 275, no. 5300, pp. 637–641, 1997.

[55] C. J. Pethick and H. Smith, *Bose–Einstein Condensation in Dilute Gases*, 2nd ed. Cambridge University Press, 2008.

[56] C. Kohstall, S. Riedl, E. S. Guajardo, L. Sidorenkov, J. H. Denschlag, and R. Grimm, “Observation of interference between two molecular bose–einstein condensates,” *New Journal of Physics*, vol. 13, no. 6, p. 065027, 2011.

[57] S. Hofferberth, I. Lesanovsky, B. Fischer, T. Schumm, and J. Schmiedmayer, “Non-equilibrium coherence dynamics in one-dimensional bose gases,” *Nature*, vol. 449, no. 7160, pp. 324–327, 2007.

[58] T. Schweigler, V. Kasper, S. Erne, I. Mazets, B. Rauer, F. Cataldini, T. Langen, T. Gasenzer, J. Berges, and J. Schmiedmayer, “Experimental characterization of a quantum many-body system via higher-order correlations,” *Nature*, vol. 545, no. 7654, pp. 323–326, 2017.

[59] S. Ianeselli, C. Menotti, and A. Smerzi, “Beyond the landau criterion for superfluidity,” *Journal of Physics B: Atomic, Molecular and Optical Physics*, vol. 39, no. 10, p. S135, 2006.

[60] W. Kwon, G. Del Pace, R. Panza, M. Inguscio, W. Zwerger, M. Zaccanti, F. Scazza, and G. Roati, “Strongly correlated superfluid order parameters from dc josephson supercurrents,” *Science*, vol. 369, no. 6499, pp. 84–88, 2020.

[61] W. Kwon, G. Del Pace, K. Xhani, L. Galantucci, A. Muzi Falconi, M. Inguscio, F. Scazza, and G. Roati, “Sound emission and annihilations in a programmable quantum vortex collider,” *Nature*, vol. 600, no. 7887, pp. 64–69, 2021.

[62] A. Amar, Y. Sasaki, R. Lozes, J. Davis, and R. Packard, “Quantized phase slippage in superfluid he 4,” *Physical review letters*, vol. 68, no. 17, p. 2624, 1992.

[63] O. Avenel and E. Varoquaux, “Observation of singly quantized dissipation events obeying the josephson frequency relation in the critical flow of superfluid he 4 through an aperture,” *Physical review letters*, vol. 55, no. 24, p. 2704, 1985.

[64] T. W. Neely, E. C. Samson, A. S. Bradley, M. J. Davis, and B. P. Anderson, “Observation of vortex dipoles in an oblate bose-einstein condensate,” *Physical review letters*, vol. 104, no. 16, p. 160401, 2010.

[65] M. Kunimi and I. Danshita, “Decay mechanisms of superflow of bose-einstein condensates in ring traps,” *Physical Review A*, vol. 99, no. 4, p. 043613, 2019.

[66] J. R. Abo-Shaeer, C. Raman, J. M. Vogels, and W. Ketterle, “Observation of vortex lattices in bose-einstein condensates,” *Science*, vol. 292, no. 5516, pp. 476–479, 2001.

[67] J. Anglin, "Local vortex generation and the surface mode spectrum of large bose-einstein condensates," *Physical review letters*, vol. 87, no. 24, p. 240401, 2001.

[68] R. Dubessy, T. Liennard, P. Pedri, and H. Perrin, "Critical rotation of an annular superfluid bose-einstein condensate," *Physical Review A*, vol. 86, no. 1, p. 011602, 2012.

[69] A. W. Baggaley and N. G. Parker, "Kelvin-helmholtz instability in a single-component atomic superfluid," *Physical Review A*, vol. 97, no. 5, p. 053608, 2018.

[70] T. Kanai, W. Guo, and M. Tsubota, "Emergence of spiral dark solitons in the merging of rotating bose-einstein condensates," *arXiv preprint arXiv:1803.03747*, 2018.

[71] ——, "Merging of rotating bose–einstein condensates," *Journal of Low Temperature Physics*, vol. 195, no. 1, pp. 37–50, 2019.

[72] G. E. Volovik, "On the kelvin-helmholtz instability in superfluids," *Journal of Experimental and Theoretical Physics Letters*, vol. 75, no. 8, pp. 418–422, 2002.

[73] R. Blaauwgeers, V. Eltsov, G. Eska, A. Finne, R. P. Haley, M. Krusius, J. Ruohio, L. Skrbek, and G. Volovik, "Shear flow and kelvin-helmholtz instability in superfluids," *Physical review letters*, vol. 89, no. 15, p. 155301, 2002.

[74] H. Takeuchi, N. Suzuki, K. Kasamatsu, H. Saito, and M. Tsubota, "Quantum kelvin-helmholtz instability in phase-separated two-component bose-einstein condensates," *Physical Review B*, vol. 81, no. 9, p. 094517, 2010.

[75] N. Suzuki, H. Takeuchi, K. Kasamatsu, M. Tsubota, and H. Saito, "Crossover between kelvin-helmholtz and counter-superflow instabilities in two-component bose-einstein condensates," *Physical Review A*, vol. 82, no. 6, p. 063604, 2010.

[76] H. Kokubo, K. Kasamatsu, and H. Takeuchi, "Pattern formation of quantum kelvin-helmholtz instability in binary superfluids," *Physical Review A*, vol. 104, no. 2, p. 023312, 2021.

[77] L. Giacomelli and I. Carusotto, "Interplay of kelvin-helmholtz and superradiant instabilities of an array of quantized vortices in a two-dimensional bose–einstein condensate," *arXiv preprint arXiv:2110.10588*, 2021.

[78] T. Giamarchi, "Current drag in two leg quantum ladders," *Physica E: Low-dimensional Systems and Nanostructures*, vol. 77, pp. 164–168, 2016.

[79] M. E. Gehm, *Preparation of an optically-trapped degenerate Fermi gas of 6 Li: Finding the route to degeneracy.* Duke University, 2003.

Ringraziamenti

Un grazie a Giulia e Giacomo, per avermi guidato con il vostro immancabile ottimismo durante questo lavoro di tesi. Thank you Woo Jin, muchas gracias Diego, Merci Cyprien, per tutte le ore passate in laboratorio.
Un forte ringraziamento va a tutta la mia famiglia, in particolare ai miei genitori per avermi dato l'opportunità di raggiungere questo traguardo e per avermi insegnato l'impegno e la dedizione, e a mio fratello, buon esempio e degno avversario. Un grazie a tutti i miei amici, per aver allietato le serate durante questi anni.
Infine grazie a te Elena, per tutti i momenti passati insieme, per esserci sempre stata, per averci sempre creduto.